SHAPE MEMORY CERAMIC ACTUATION OF ADAPTIVE STRUCTURES

by

Kamyar Ghandi

Submitted to the Department of
Aeronautics and Astronautics in Partial
Fulfillment of the Requirements for the
Degree of

Master of Science
in Aeronautics and Astronautics
at the

Massachusetts Institute of Technology

January 1995

Signature of Author .....
Department of Aeronautics and Astronautics
January 13, 1995

Certified by .....
Professor Nesbitt W. Hagood
Thesis Supervisor

Accepted by .....
Professor Harold Y. Wachman
Chairman, Department Graduate Committee

SHAPE MEMORY CERAMIC ACTUATION OF ADAPTIVE STRUCTURES

by
Kamyar Ghandi

Submitted to the Department of Aeronautics and Astronautics
on January 13, 1995, in partial fulfillment of the requirements for
the Degree of Master of Science in Aeronautics and Astronautics

ABSTRACT

Field induced phase transitions in electroceramics with the advantages of large strain and shape memory are investigated as a mechanism for structural actuation. Several compositions were manufactured and studied. Phase transition and shape memory behavior of lanthanum and niobium doped lead zirconate titanate compositions were investigated. The dependence of the material response on various factors relevant to structural actuation has been examined. Factors such as induced stress, actuation frequency, and temperature play an important role in the response of the material. A phenomenological model for phase transition is proposed which is capable of modeling the static response of the material. While the dynamic response of the model agrees qulitatively with material behavior, the accuracy remains unsatisfactory.

The use of shape memory ceramic active materials in design of adaptive structures is discussed. Specifically, an adaptive mirror is considered and several design issues are addressed using finite element and Rayleigh-Ritz models. A prototype mirror using the material under investigation was constructed, tested, and used to validate model predictions.

ACKNOWLEDGMENTS

I would like to thank my advisor Professor Nesbitt W. Hagood whose guidance and supervision were essential for the completion of this work. I would also like to thank my colleagues Michael Fripp, Kin Chan, Aaron Bent, John Rodgers, and my undergraduate assistant Lana Luoma for their help.

I am also grateful to Dr. Richard Pober of the Ceramics Processing Research Lab, and Richard Perilli and Tim McClure of the Center for Materials Science and Engineering for their instructions on manufacturing and processing ceramics, and to prof. Kenji Uchino of Pensylvania State University for supplying samples of $PbNb(Zr,Ti,Sn)O_3$.

The research was funded by Jet Propulsion Laboratories.

TABLE OF CONTENTS

LIST OF FIGURES

NOMENCLATURE

Scalars:

A	Sample area.
A_s, A_f	Austenite start and finish temperatures.
a_A, a_M,	Parameter defined in the Rogers' model.
a, e	Electromechanical coupling constants.
C_A, C_M	Parameter defined in the Rogers' model.
c	Effective stiffness.
c^a	Effective stiffness of actuator.
c_{ij}	Stiffness matrix elements.
c^s	Effective stiffness of structure.
D	Electric displacement.
D, Ω, Θ	Shape memory alloy coupling constants.
E	Young's modulus.
E	Electric field.
E_c	Coercive electric field.
E_f, E_r	Forward and reverse transition field levels.
E_f^m, E_f^s, E_f^a	Mean, standard deviation, and asymmetry of E_f distribution.
E_r^m, E_r^s, E_r^a	Mean, standard deviation, and asymmetry of E_r distribution.
f(E_f,E_r)	Probability density function for distribution of families.
I	Electric current.
J	Cost function used in parameter optimization
k_s	Spring stiffness constant.

M_s, M_f	Martensite start and finish temperatures.
N	Internal variable representing polarization.
N_p, N_r	Net polarization of permanent and rotatable domains.
N_1, N_2	Fraction of total material in FE+ and FE- phases.
n_1, n_2	Fraction of each family in FE+ and FE- phases.
N_{FE}, N_{AFE}	Fraction of material in FE and AFE phases.
P	Polarization.
p, h	Width and height of representative volume element.
Q	Total charge.
q_i	Charges on each electrode.
r, p, q	Parameters in Chen and Montgomery model.
S	Strain.
S_{ij}	Components of the strain tensor.
s_{ij}	Compliance matrix elements.
T	Temperature.
T_{ij}	Components of the stress tensor.
t	Time.
t^a, t^s	Thickness of actuator and of structure.
U	Internal mechanical energy.
u_x, u_y, u_z	Displacement components.
W	Work due to applied surface stresses and applied charges.
W_e, W_m	electric and magnetic energy.
$\tilde{x}$, $\tilde{y}$, $\tilde{z}$	Nondimentionalized coordinates.
$\alpha(E)$, $\beta(E)$	Chen and Montgomery rate law functions.
α_f, α_r, α_r	Rate parameters.
$\bar{\varepsilon}$	Green strain.
ε_o	Dielectric constant of vacuum.
ε^s	Dielectric matrix at constant strain.
φ	Electric potential.
φ_i	Potential at each electrode.
ν	Poisson's ratio.
$\bar{\sigma}$	Piolka-Kirchhoff stress.
τ	Thickness ratio.
ξ	Martensitic fraction.
ψ	Stiffness ratio.

Vectors:

κ	Curvature vector.
Λ	Free strain vector.
$\mathbf{M}$	Resultant moments.
$\mathbf{M}_e$	Induced resultant moments due to actuator.
$\mathbf{N}$	Resultant loads.
$\mathbf{N}_e$	Induced resultant loads due to actuator.
$\mathbf{r}$	Vector of displacement degrees of freedom.
$\mathbf{S}$	Strain vector.
$\mathbf{S}^o$	Strain vector along z=0.
$\mathbf{T}$	Stress vector (in engineering notation).
$\mathbf{T}_s$	Surface stresses.
$\mathbf{u}$	Displacement vector.
$\mathbf{v}$	Vector of potential degrees of freedom.

Matrices:

$\mathbf{A}$	Extensional stiffness matrix in classical laminate plate theory.
$\mathbf{B}$	Coupling stiffness matrix in classical laminate plate theory.
$\mathbf{c}$	Material stiffness matrix.
$\mathbf{D}$	Bending stiffness matrix in classical laminate plate theory.
$\mathbf{d}$	Piezoelectric constants relating strain to applied field.
$\mathbf{e}$	Piezoelectric constants relating stress to applied field.
$\mathbf{F}_r$, $\mathbf{F}_v$	Applied load and charge matrices in the Ritz model.
$\mathbf{K}$, Θ, $\mathbf{C}$	Structure stiffness and coupling matrices in the Ritz model.
$\mathbf{N}_r$	Matrix of strain shape functions.
$\mathbf{N}_v$	Matrix of electric field shape functions.
$\mathbf{s}$	Material compliance matrix.
Ψ_r	Matrix of displacement shape functions.
Ψ_v	Matrix of potential shape functions.

Symbols:

L_r	Displacement→strain differential operator.
L_v	Voltage→electric field differential operator (gradient operator).
$(\cdot)^S$	Values measured at constant strain (e.g. clamped).

$(\cdot)^T$	Values measured at constant stress (e.g. free strain).
$(\cdot)^E$	Values measured at constant electrical field (e.g. short circuit).
$(\cdot)^*$	Reduced plane stress stiffness/compliance constants.
$(\cdot)^\mathsf{T}$	Matrix transpose.

Acronyms:

AFE	Antiferroelectric.
A_O	Orthorhombic phase: antiferroelectric.
A_T	Tetragonal phase: antiferroelectric.
FE	Ferroelectric.
F_R	Rhombohedral phase: ferroelectric.
F_T	Tetragonal phase: ferroelectric.
PLZST	Lead lanthanum zirconate stannate titanate (PbLaZrSnTi).
PLZT	Lead lanthanum zirconate titanate (PbLaZrSnTi).
PNZST	Lead niobium zirconate stannate titanate (PbNbZrSnTi).
PZT	Lead zirconate titanate (PbZrTi).
SMA	Shape memory alloys.
SMC	Shape memory ceramics.

1 INTRODUCTION

The past few years have seen a great deal of emphasis on structural actuation and sensing. In many cases, structural actuation is needed to further extend the performance of a system, while meeting more stringent weight and size requirements. To push the limits of current technology, further research in several areas is required. These include work in structural dynamics and modeling, control system design, and finally, design of improved actuators and sensors.

Electroceramics have been utilized in structural actuation for some time [10]. The benefits of using such actuators are the compact size, and precision with which they can be operated. Unfortunately, conventional electroceramics such as piezoelectrics and electrostrictors are only used in a limited range of their actuation capability due to the nonlinearity of their response. For example, piezoelectrics can only achieve strain levels up to a couple of hundred micro strain when operated in their linear range. Such small strain levels are quite adequate for some applications, such as micro positioning devices, and vibration control of certain structures. Other applications, such as aeroelastic control and static shape control, need higher actuator strains to be feasible. Several approaches can be taken to compensate for low strain levels. Ceramic wafers can be bonded together to form actuator stacks, increasing the overall stroke. Or the material may be operated beyond its linear range using improved nonlinear models of the material behavior [7]. Finally, one may pursue the development of new materials with higher strain capability.

Continuing research into materials possessing electro-mechanical coupling holds the promise of higher actuation authority as well as other useful characteristics, such as lower hysteresis, faster response, reduced temperature dependence and/or shape memory. Shape

memory alloys such as Nitinol, which undergo a phase transition accompanied with large strains when subjected to a temperature change, are examples of the new materials that have been developed in recent decades. The area of particular interest in the present work is electric field induced phase transitions in electroceramics. In certain ceramics, the application of a sufficiently large electric field can cause a change in the crystal structure of the material. Such phase transitions may be accompanied by a strain in the material. Field induced phase transitions have been investigated by several authors [13,23,8]. Two families of materials displaying beneficial behavior are the lead lanthanum zirconate stannate titanate (PbLaZrSnTi or PLZST) family of ceramics studied by L. E. Cross [13], and the lead niobium zirconate stannate titanate (PbNbZrSnTi or PNZST) family of ceramics studied by K. Uchino [23]. Depending on the exact proportion of the constituent ions, as well as external conditions such as temperature, stress, and electric field, the crystallite domains may exist in a variety of states such as rhombohedral, orthorhomic, or tetragonal. Large strains have been observed to occur during the orthorhomic antiferroelectric (AFE) to tetragonal ferroelectric (FE) phase transition in certain varieties of these electroceramics, making them a candidate for high strain actuators. Furthermore, some ceramics are metastable in both the ferroelectric and antiferroelectric phases. Thus they are capable of maintaining a residual strain even after the electric field has been switched off, displaying shape memory in a manner analogous to shape memory alloys.

The feasibility of using the strain associated with field induced phase transition in actuating adaptive structures is the primary focus of the present work†. Various factors such as the response of the material at different temperatures, frequencies, and structural stress, which are of concern in an structural control application, have been considered.

Three factors motivate the study of field induced phase transitions as an actuation mechanism. First, strain levels as high as 0.6% have been reported to occur during the phase transition, making the material ideal for meeting the high strain requirements for many applications. Second, the use of shape memory in control of adaptive structures has clear advantages. For example, a large number of actuators could be operated with only a few number of amplifiers, since the electric field does not need to be sustained to maintain a certain strain level. The final motivation is the bandwidth of the actuators. In shape memory alloys, phase transitions are induced by changes in temperature. By contrast, in shape memory ceramics, phase transitions are induced by the application of an electric

---

† Initial findings were published by the author in 1994 [14].

field. Since an electric field can be changed at much higher rates than temperature, shape memory ceramics may be actuated at higher bandwidths. Thus, although they have lower strain levels than shape memory alloys, they may be more suitable for certain applications.

Utilizing these materials in actual applications requires an understanding of the dependence their properties on operating conditions and the capability of predicting the nonlinear behavior of the material. A phenomenological model for the phase transition based on a family of internal variables has been formulated for antiferroelectric-ferroelectric switching. Various model parameters were obtained by optimizing the correspondence with data from material characterization experiments. The model is capable of reproducing experimental strain curves under quasistatic conditions or a narrow frequency range. Further work is required to improve modeling of the frequency response of the material.

The specific application utilized as a case study is adaptive optics. With the use of space based telescopes, such as the Hubble Space Telescope, which avoid atmospheric disturbance, the optics themselves become the limiting factor in performance. An adaptive deformable mirror can be used to correct for imperfections in other components of the telescope to achieve diffraction-limited images at much lower wavelengths, well into the ultra violet region. Another advantage of space observatories is the possibility for high dynamic range or coronographic imaging. That is, the imaging of a faint object close to a bright star [29]. Space telescopes utilizing adaptive optics, would improve results of coronographic imaging techniques by reducing the scattered light. An even more sophisticated approach is the use of adaptive mirrors to implement 'dark hole' algorithms. Rather than attempting to reduce the scattered light uniformly over the field of view, such algorithms reduce the scattered light by an additional factor of ~100 to ~1000 only in the specific region near the center of the field of view. The mirror would actively redistribute the scattered light away from the area where the faint object is being observed [29]. Using a large number of actuators in such an application is made much simpler by the shape memory of the PLZST ceramics. This has been investigated by constructing small prototype adaptive mirrors.

The following chapter of this report contains a more detailed description of antiferroelectric-ferroelectric phase transitions. The observed material behavior is explained and compared to polarization reversal in ferroelectrics, and the underlying mechanisms are explained in terms of the ceramic structure. This is followed by a historical overview of the previous work in the field.

Several compositions of shape memory ceramics were manufactured for the study. In Chapter 3, the manufacturing process and the steps taken to improve the quality of the ceramics are described.

Chapter 4 contains results from the material characterization experiments. Data on the transverse and longitudinal strains of the material under applied electric fields are presented. The dependence of the material behavior on temperature and frequency are also included. Partially clamped tests were used to determine the response of the material under structural stress, and to calculate the stiffness of the material.

Chapter 5 addresses material modeling. Several models from the literature for materials such as shape memory alloys which also undergo phase transitions are summarized. This is followed by the development of a phenomenological model for antiferroelectric-ferroelectric materials.

The material has been used in the construction of small adaptive mirrors (with only four actuators), which are described in Chapter 6. Both theoretical predictions and experimental data on the structural response of the mirrors are presented. Finally, various factors to be considered in the design and construction of a full scale adaptive mirror are discussed based on finite element and Rayleigh-Ritz models.

2 BACKGROUND

The focus of the present work is the field induced transitions between ferroelectric and antiferroelectric states. As such, some description of the material, and the history of their development is in order.

2.1 Material Behavior

In general, crystals can be divided into 32 classes according to their rotational symmetry [6]. Twenty of these classes display the phenomenon of piezoelectricity, i.e. they exhibit an electric charge upon application of external stress. Half of the classes in this category are pyroelectric. Pyroelectric crystals have a spontaneous polarization, since along at least one axis the cells are nonsymmetric. This electric polarization is generally masked due to existence of surface charges. But usually, a change in polarization, caused for example by altering the temperature, can be measured in nonconducting pyroelectric material [31]. Thus, piezoelectricity and pyroelectricity are simply functions of the crystal structure, and can be predicted as soon as the crystal class is determined.

The direction of polarization of some pyroelectrics can be reversed through application of a large enough electric field. This subgroup of pyroelectrics is referred to as ferroelectrics. Unlike piezoelectricity or pyroelectricity, knowing the crystal class is not sufficient to establish ferroelectricity, and dielectric measurements are required [31]. Figure 2.1 shows the characteristic hysteresis loop of a ferroelectric material. The plot shows the observed electric displacement as a cyclic field is applied to the material. The

electric displacement is proportional to the charge on the surface of the material and can be measured by integrating the current supplied to the sample. The polarization (P) is related to the electric displacement (D) through the relation:

$$D = \varepsilon_0 E + P \tag{2.1}$$

where E is the electric field and ε_0 is the dielectric constant of vacuum. Different domains in an unpoled ferroelectric ceramic are polarized in different directions. As an electric field is applied, the polarization of the domains switch until finally all domains are aligned in the same direction. As the field is reduced to zero, some of the domains maintain their state and thus a finite value of "remnant" polarization (P_r) is observed. Note from equation 2.1 that at E=0 the polarization and the electric displacement are equivalent. Applying an electric field in the opposite direction with an amplitude larger than the coercive field of the material (E_c) can remove the remnant polarization [31]. The hysteresis can be directly observed on an oscilloscope by means of a simple circuit first described by Sawyer and Tower [28].

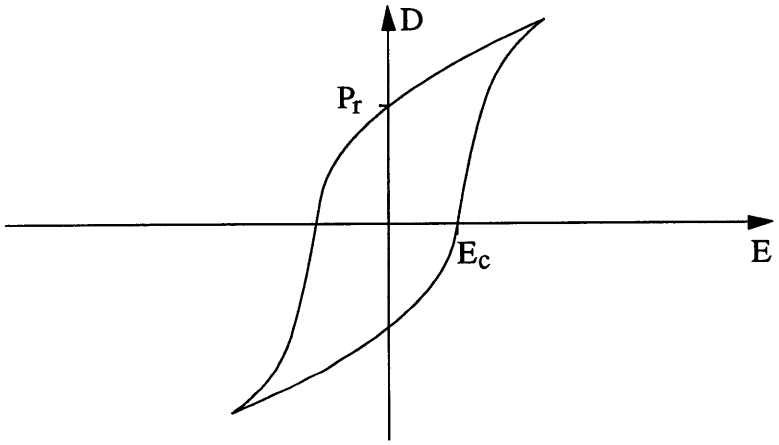

Figure 2.1 - Standard hysteresis loop of a conventional ferroelectric.

Figure 2.2 shows the general crystal structure of a perovskite [5], which is the crystal structure of such common ferroelectrics as barium titanate and lead zirconate titanate (PZT). The general formula for a perovskite can be written as ABO_3, where A and B are metal ions having a total charge of +6. The relative size of the ions is the key to the properties of the material. A and B must represent ions which have quite different sizes for the perovskite structure to form. In the case of barium titanate, A and B are the divalent cation Ba^{2+} and the tetravalent cation Ti^{4+}. The material of interest in the present work is similar to PZT ceramics, where divalent (Pb^{2+}) and tetravalent (Zr^{4+},Ti^{4+}) cations have

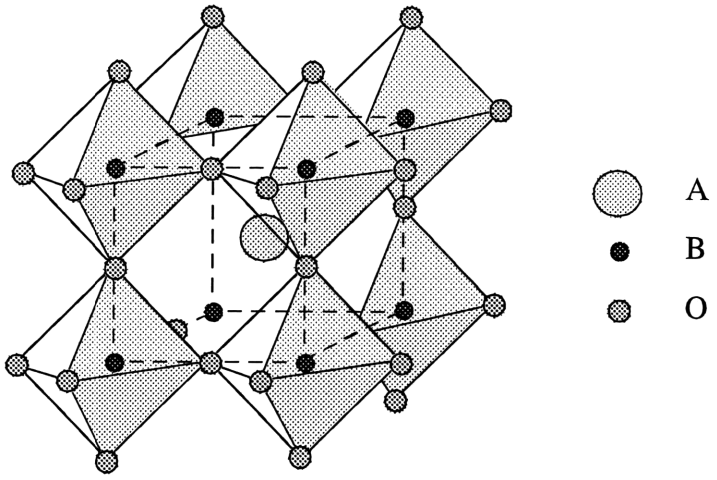

Figure 2.2 - The perovskite structure is built of corner-shared octahedral cages. [5, pp. 54]

been substituted for A and B. The properties of the material can be modified by adjusting the Zr^{4+} and Ti^{4+} cations, or by adding other metal oxides to form compounds such as $(Pb,La)(Zr,Sn,Ti)O_3$.

Depending on the exact composition and the temperature, the shape of the perovskite cell can change. At high temperatures, thermal vibrations of the B-site cation, keeps the oxygen anions of the tetrahedral cages apart. The structure maintains an undistorted cubic shape, and the material is in a paraelectric phase. Application of an electric field to a paraelectric material produces polarization, which vanishes upon the removal of the field. As the temperature is lowered below the Curie point of the material, the cubic structure becomes unstable and the cell is distorted. Figure 2.3 shows the different phases that arise in PZTs as the ratio of the Zr and Ti in the composition is changed. In the tetragonal phase, the cube is stretched parallel to an edge, while in rhombohedral crystals, the cube is stretched along a body diagonal. Both of these phases are ferroelectric, with the polarization in tetragonal crystals occurring along a body axis in the direction of elongation, and polarization for rhombohedral crystals occurring along a body cube diagonals. Rhombohedral crystals may undergo further transitions at lower temperatures, becoming orthorhombic. In orthorhombic crystals, adjacent cells are oppositely polarized, resulting in zero net polarization of the domain.

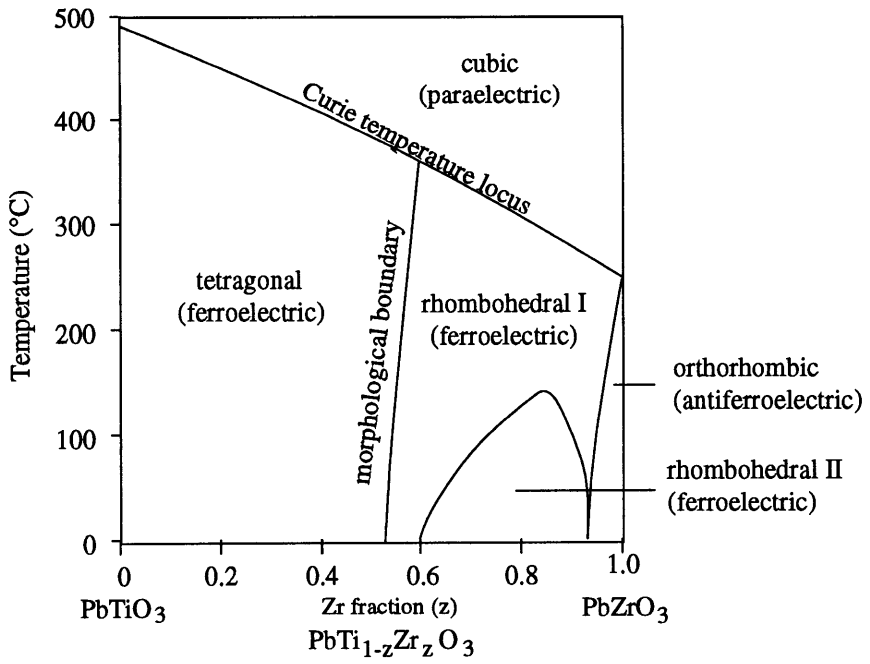

Figure 2.3 - Equilibrium phase diagram for PZT. [5, pp. 175]

Introducing other oxides to the composition can modify the properties of the material. Figures 2.4 and 2.5 show the ceramic phases of $Pb_{0.97}La_{0.02}(ZrTiSn)O_3$ and $Pb_{0.97}Nb_{0.02}(ZrTiSn)O_3$ as the ratio of Zr, Ti, and Sn as the composition is varied. These phase diagrams were first produced by Berlincourt in 1966 [3]. $F_R(LT)$ and $F_R(HT)$ are the low temperature and high temperature ferroelectric rhombohedral regions. A_O and A_T are the antiferroelectric orthorhomic and tetragonal regions respectively. The A_T region (which was not present in the compositions without Sn) and the $F_R(LT)$ region are energetically close. Thus it is possible to induce a phase transition from the antiferroelectric to the ferroelectric phase by applying an electric field for compositions that lie close to the boundary. Other transitions such as A_O to $F_R(LT)$ would involve too much energy to be achieved by a realizable field. It is therefore the transition between the rhombohedral ferroelectric phase and the tetragonal antiferroelectric phase, which is the focus of the present work.

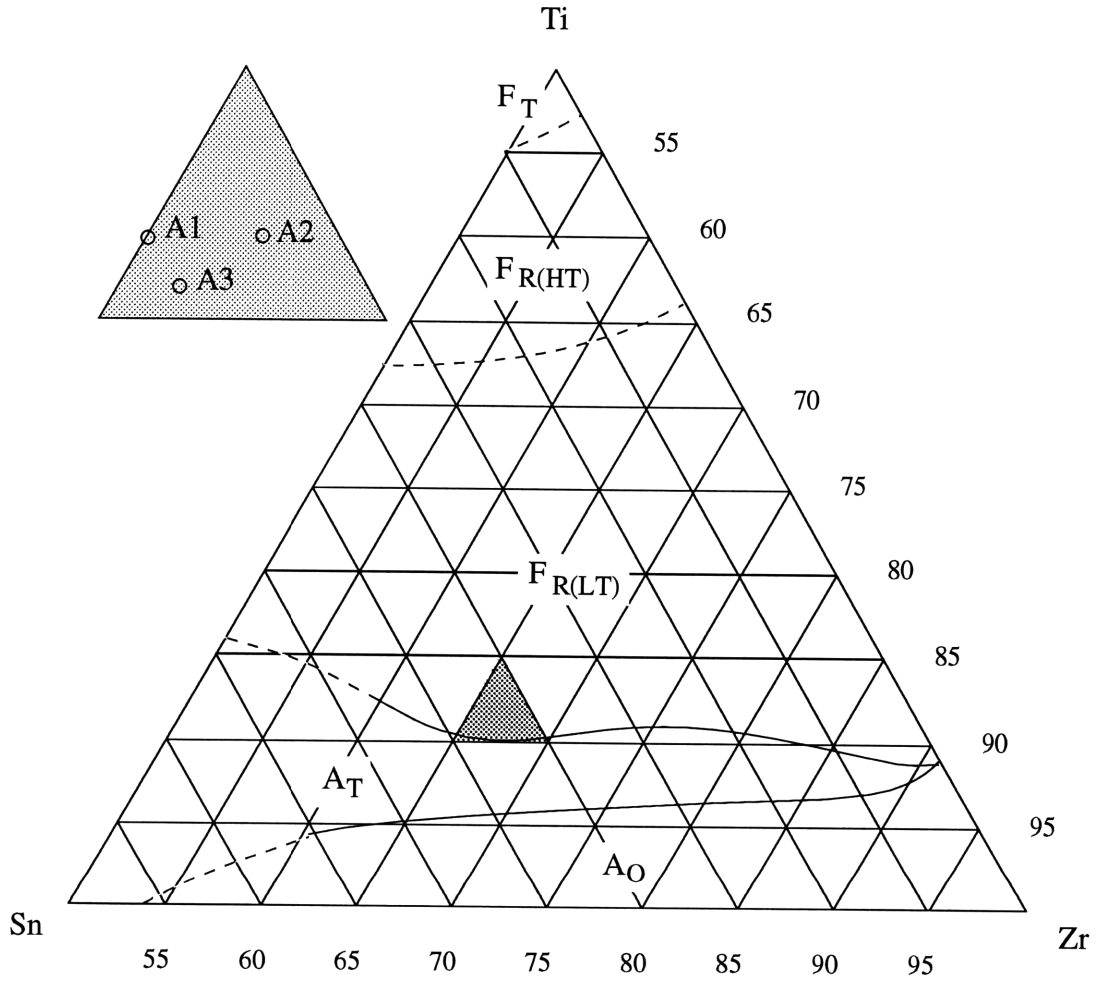

Figure 2.4 - Phase diagram for $Pb_{0.97}La_{0.02}(ZrTiSn)O_3$ at 25°C. The inset shows the compositions manufactured for this study. [3]

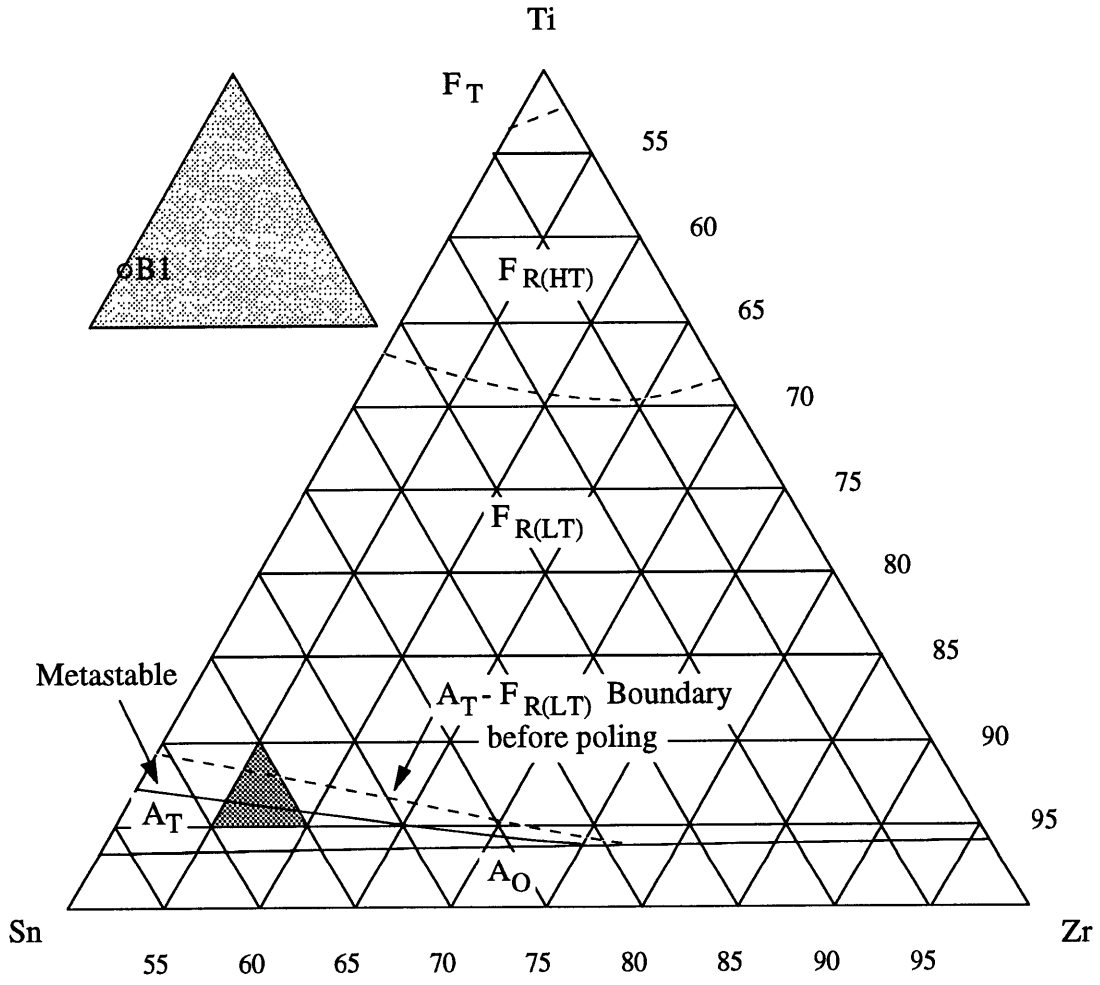

Figure 2.5 - Phase diagram for $Pb_{0.97}Nb_{0.02}(ZrTiSn)O_3$ at 25°C. The inset shows the composition supplied by Penn. state university. [3]

In ferroelectrics, an electric field can cause mechanical strain due to the polarization of the material (Figure 2.6). However, since antiferroelectrics contain two sub-lattices which are spontaneously polarized in opposite directions, and thus do not display any macroscopic polarization, very little strain is achieved when applying low electric fields. If the composition of an antiferroelectric material is close to the ferroelectric phase boundary, a phase transition from AFE to FE can be induced by the application of a large electric field. This phase transition is accompanied by a lattice distortion leading to a net volume expansion in the material [23]. The isotropic expansion manifests itself as a sharp jump in the strain level of the material. This can be seen in Figure 2.6, which shows the strain in the material as it is subjected to a periodic electric field of fixed frequency and amplitude. Longitudinal strain levels ranging from 0.08% to 0.6% have been reported for various compositions [13,23]. The compositions studied in the present work have shown strain levels of ~0.3%. Following this transition into the ferroelectric phase, the material displays anisotropic strains due to the reorientation of the ferroelectric domains.

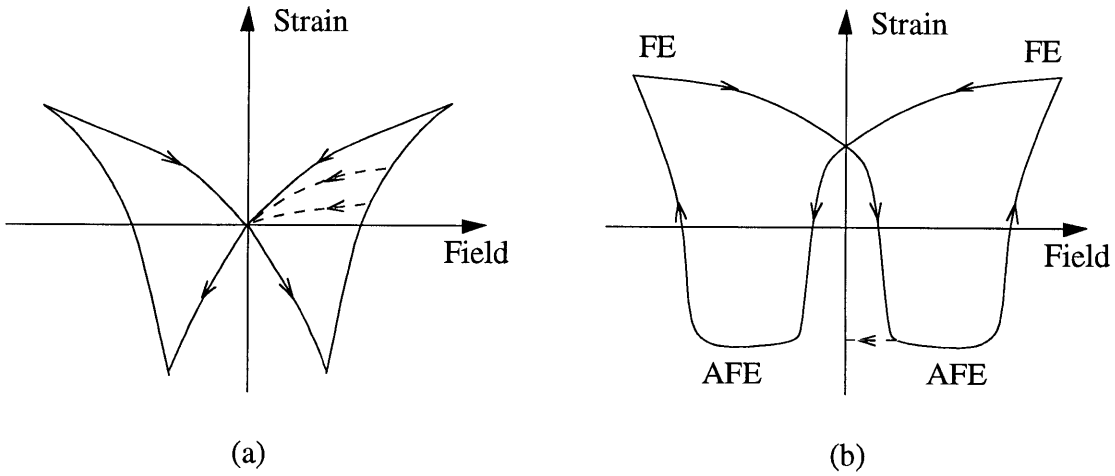

Figure 2.6 - Comparison of the longitudinal strains for ferroelectric and antiferroelectric materials. (a) is ferroelectric. (b) undergoes field induced phase transition from antiferroelectric and vice versa.

As the electric field is reduced, the material may either return to its original state, or remain in the ferroelectric state (exhibiting shape memory), depending on the exact composition. The ceramics lacking shape memory are only stable in the antiferroelectric state at zero field, while those with shape memory are metastable in either of the ferroelectric and the antiferroelectric states at zero field. In the latter case, a field in the opposite direction must be applied to remove the residual strain.

2.2 History of Developments in AFE/FE Phase Transitions

The existence of antiferroelectric crystals was first proposed by C. Kittel in 1951 based on analogy to antiferromagnetic crystals [20]. This was accomplished before any material was identified as antiferroelectric. The antiferroelectric state was defined as one in which the ions in the crystal are spontaneously polarized such that neighboring cells are polarized in antiparallel directions, resulting in net zero polarization. It was predicted that the antiferroelectric state would not be piezoelectric, unlike the ferroelectric state which is piezoelectric. The dielectric constant of the antiferroelectric below the Curie point was not expected to be particularly large, and an anomaly in the heat capacity at the Curie point was expected to exist similar to ferroelectrics.

Later in 1951, Shirane *et al.* studied the dielectric properties of Lead Zirconate at various temperatures [30]. As the temperature of the material was increased, a sudden increase in polarization was observed near the Curie point, which suggested the absence of spontaneous polarization below the Curie point. They proposed the existence of an antiferroelectric phase below the Curie point to explain this phenomenon. Furthermore, anomalous polarization-electric field hysteresis loops (Figure 2.7) were observed below the Curie point, which can be explained in terms of an antiferroelectric to ferroelectric phase transition. At these temperatures, the material is antiferroelectric, but the application of a large enough electric field produced ferroelectric behavior.

Berlincourt *et. al.* performed detailed studies of the phase boundary between

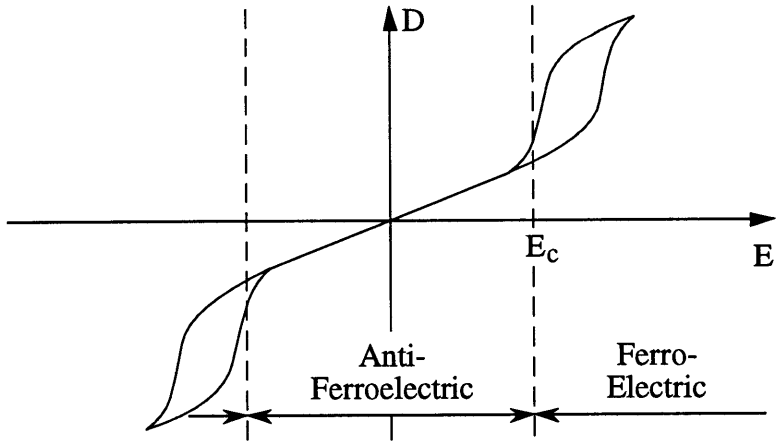

Figure 2.7 - Anomalous hysteresis loops of $PbZrO_3$ at 30 kV/cm explained in terms of antiferroelectric-ferroelectric transition. [30]

ferroelectric and antiferroelectric states of lead zirconate modified with titanium, niobium, and tin [1]. $PbZrO_3$ is an antiferroelectric with orthorhombic structure at room temperature. Substitution of Ti for Zr, Ba for Pb, or Nb for Zr brings about a ferroelectric (rhombohedral) phase. Substitution of Sn for (Zr,Ti) in $Pb(Zr,Ti)O_3$ lowers the distortion of the ferroelectric rhombohedral phase, and reduces the volume difference between ferroelectric and antiferroelectric phases. Substitution of Nb for Zr favors ferroelectricity, and substitution of La for Pb favors antiferroelectricity. Their study produced phase diagrams of the types pressure-temperature, pressure-electric field, electric field-temperature, temperature-composition, electric field-composition, and pressure-composition. Simple cubic, multiple cell cubic, orthorhombic antiferroelectric, tetragonal antiferroelectric, rhombohedral ferroelectric, and rhombohedral ferroelectric phase with superstructure were identified on these diagrams. Thus a comprehensive map of the stable material phases was presented for certain compositions in the PbNb(ZrSnTi)O family.

The difference in the crystal structure of the AFE and FE phases results in a higher specific volume in the ferroelectric phase. It was shown by Jaffe that certain $Pb(Zr,Sn,Ti)O_3$ compositions have antiferroelectric and ferroelectric states of nearly equal energy over a wider range of temperatures than $Pb(Zr,Ti)O_3$ [18]. Thus Berlincourt *et. al.* were able to find that substantial electric energy could be released at high voltage, by inducing a FE to AFE phase transition through the application of a hydrostatic pressure to modified polycrystalline lead zirconate [2]. The material could also be used for conversion of thermal energy to electrical energy. While the overall efficiency of this conversion was about 0.4%, the high output voltage was considered to be a significant benefit.

Further research into antiferroelectric-ferroelectric phase transitions was motivated by the large strains associated with the transition. One of the applications being considered at the time was the use of the material to create acoustic radiation in a fluid media. Piezoelectrics used in such applications required designing resonant composite structures in order to achieve sufficient amplitude. This however is not possible at low frequencies which are desired for long range transmissions. The large strains associated with field-forced phase transitions were considered to be an alternative to the use of resonant structures. An ideal transducer for this purpose would have no hysteresis (Figure 2.8). The real material however displays a double hysteresis loop. To search for the most suitable material and operating conditions, Berlincourt studied numerous compositions of the form $Pb_{0.99}Nb_{0.02}(Zr,Sn,Ti)_{0.98}O_3$ and $Pb_{0.97}La_{0.02}(Zr,Sn,Ti)O_3$ [3]. He obtained Triaxial phase diagrams indicating the various material phases depending on composition,

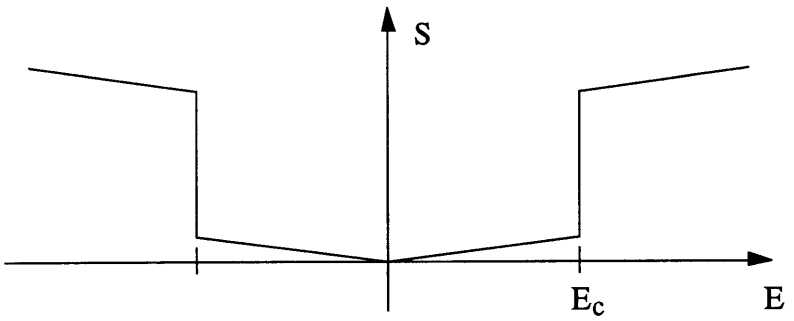

Figure 2.8 - Idealized antiferroelectric-ferroelectric field forced transitions. [3]

as well as temperature-composition and electric field-hydrostatic pressure phase diagrams for specific compositions. He also determined that the AFE-FE transition is a first-order transition and presented equations governing the transition based on Gibbs free energy.

Cross *et. al.* searched for compositions close to the morphotropic phase boundary between rhombohedral and tetragonal phases of lead lanthanum zirconate titanate (PLZT) ceramics and modified lead lanthanum zirconate stannate titanate compositions [13,26,27]. As the La content was increased the induced strain was found to become more electrostrictive in nature [26]. Strain levels as high as 0.9% were found during the phase transition. The switching speed of the transition was also studied by applying a square pulse to the samples and was found to be on the order of 1-2 μs. Aging effects were also studied. The ceramics were found to degrade under AC field excitation. Average life cycles were in the range 10^6-10^7. It was found that this could be greatly improved by careful polishing of the sample surfaces [27].

Uchino stressed the digital nature of the strain produced by the AFE-FE transition [32]. The electric field dependence of the strain in the AFE and FE states is rather small, compared to the strain caused by transition. Making the material suitable for construction of digital displacement transducers. He also noted that in certain compositions the field induced ferroelectric phase did not return to the AFE state even after decreasing the field to zero, giving rise to a shape memory behavior similar to those in shape memory alloys. This can be seen in the electric field-Ti concentration phase diagram for the material studied (Figure 2.9). Two of the curves indicate the forward transition (AFE→FE) phase boundary, while the other two indicate the reverse transition (FE→AFE) phase boundary. In regions III and IV, the reverse transition can not be induced by electric field. Instead the material undergoes polarization reversal between the FE+ and FE- states, with the coercive

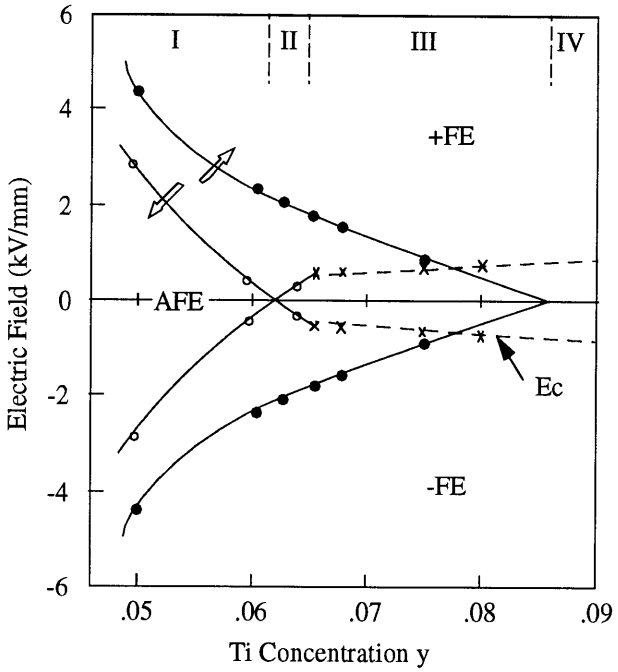

Figure 2.9 - Phase diagram of $Pb_{0.99}Nb_{0.02}[(Zr_{0.6}Sn_{0.4})_{1-y}Ti_y]_{0.98}O_3$ at room temperature with respect to the composition y and the applied electric field E. [32]

field shown as a dashed line. The compositions in region II are metastable at zero field and may exist in either phase. Thus, after a forced transition to the FE phase, they will not return to the AFE phase unless a reverse field is applied. Thus they can be said to posses shape memory. In addition, these materials have the advantage of quick response, controllability by electric field, and low energy consumption compared to shape memory alloys. Recently the group demonstrated the use of these properties by constructing a latching relay using a shape memory ceramic unimorph as well as a mechanical clamp using a multilayer stack of the same material [23].

Since Kittel's proposal of the existence of antiferroelectricity, numerous authors have studied materials exhibiting AFE-FE phase transitions. The goal of the present work, is to assess the feasibility of using such material for structural actuation. Therefore, attention is focused on the material properties which are important in such an application, namely the dependence of strain on various operating conditions. As with much of the previous work, the large strain associated with the transition is one of the main motivations. Another motivation is the shape memory property of the material which has only recently been considered significant.

3 MATERIAL MANUFACTURING

The ceramic samples studied in this work are not commercially available. It was therefore necessary to manufacture them at MIT in the Ceramic Processing Research Laboratory. There are numerous steps in the manufacturing process, which is fairly time consuming. While many of the details of the process would be considered common knowledge to researchers in the field of material science, they are presented here for the benefit of those from other engineering disciplines who might be interested in duplicating the process.

The compositions of the materials that were tested during the course of this project are listed in Table 3.1. The A1-A3 samples were Lanthanum doped compositions which were manufactured during the project. The B1 samples were from a Niobium doped composition which was supplied by professor Kenji Uchino's group at Pennsylvania State University. Figures 2.4 and 2.5 show the positions of these compositions on the appropriate phase diagrams. The selection of the Lanthanum compositions studied was based on Cross's investigation of the phase transition in high strain actuation [13]. We selected compositions which we expected would show shape memory as well as high

Table 3.1 - Compositions of the electroceramics presented in the report.

A1	$Pb_{0.97}La_{0.02}(Zr_{0.65}Ti_{0.115}Sn_{0.235})\ O_3$
A2	$Pb_{0.97}La_{0.02}(Zr_{0.67}Ti_{0.115}Sn_{0.215})\ O_3$
A3	$Pb_{0.97}La_{0.02}(Zr_{0.66}Ti_{0.105}Sn_{0.235})\ O_3$
B1†	$Pb_{0.99}Nb_{0.02}(Zr_{0.551}Ti_{0.0617}Sn_{0.3673})\ O_3$

† B1 samples were supplied by Kenji Uchino's group at Pennsylvania State University.

strain, based on Cross's published polarization curves for the material.

The raw material used in manufacturing the ceramics were reagent grade oxides obtained from Johnson Matthey Alfa and Aldrich chemical companies. The raw oxides and their formula weights are listed in Table 3.2. The amount of each raw oxide used is determined based on the composition of the desired ceramic. It should be noted that the quantities in the stoichiometry of the material refer to the proportions of the metal ions, and not the whole oxides. Thus the molar mass per mole of the metal ion in the oxide, rather than the formula weight of the oxide, was used to determine the mass of powder used.

Table 3.2 - Formula weights of the material components.

Oxide	Formula weight (g/mol)	Molar mass† (g/mol)
PbO (assay)	223.1894	223.1894
La_2O_3	325.8182	162.9091
ZrO_2	123.2188	123.2188
TiO_2 (anatase)	79.8988	79.8988
SnO_2	150.6888	150.6888

Once appropriate amounts of the oxides had been measured out, they were mixed together. To improve the mixing, the powder was put in a plastic bottle along with ballmilling rocks and some ethanol. The bottle was then put in a shaker overnight. The ethanol was then evaporated by pouring the resulting suspension into a shallow dish. While the ethanol helps in breaking up the particles and improves the mixing, during the evaporation some separation occurs, due to the density difference among the oxides. So the powder was ballmilled dry for another 24 hours. In order to minimize deviation from the desired composition due to loss of chemicals, the same container was used for the mixing and ballmilling. Thus, the powder residue remaining in the bottle at each stage could be reincorporated into the mixture.

After the ballmilling, the powder was sieved through a 45 μm mesh. Due to presence of moisture in the air, the powder can form clumps which make the sieving process difficult. Shaking alone was found to be insufficient. A brush was therefore used to guide the powder through the mesh. Any remaining powder was hand ground using a

† per mole of metal ion.

mortar and pestle, until the entire mixture was passed through the mesh. Since different component oxides start with different particle sizes, they may pass through the mesh at different rates. It is therefore important to ensure that the entire mixture is passed through the mesh to avoid deviation from the desired composition, and to roughly remix the powder after it has been sieved.

The powder was then placed in a crucible and calcined in an oven at 800°C for 10 hours. The aim of the calcination is to make the oxides react and form the desired composition. After the first calcination, the powder was ballmilled, sieved and calcined a second time, to ensure complete reaction of the powder and uniformity of the composition. After the second calcination the powder was once again ballmilled and sieved, and then pressed into a 1 inch diameter cylinder.

For best results, it is necessary to minimize residual internal stresses that may occur during the pressing. Any residual stress can result in cracks during the final sintering of the sample. The powder was pressed using a 1 inch diameter die and cylinder. As the

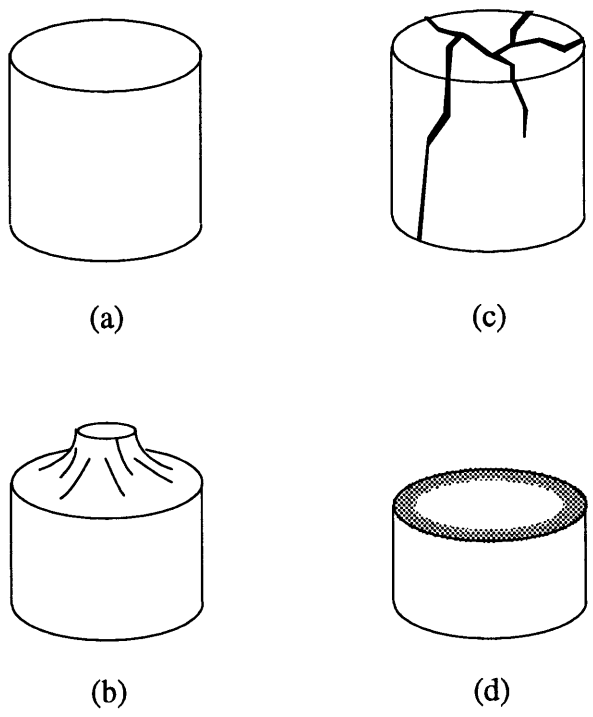

Figure 3.1 - Effect of variation in pressing method on sintered sample. a) undamaged sample. b) sample with end capping due to large loads during die press. c) cracked sample which was not isopressed before sintering. d) cross section of porous sample caused by lead loss.

powder is compressed in the cylinder, it experiences shear stresses near the cylinder walls. These lead to residual internal stresses in the sample which can result in "end capping" which are cracks in the top and bottom of the sample as shown in Figure 3.1b. Lubricating the sides of the cylinder with a 1% solution of stearic acid in acetone greatly reduced this problem. After the die press the sample is sealed in a plastic bag and is then isopressed in oil at 40000 psi for 10 minutes, to further compact the powder. Since isopressing uses hydrostatic pressure it relieves some of the internal stresses built up during the die pressing. It was found that the best results were obtained when fairly low pressures were applied with the die. A load of 5000 lb on the 1 inch diameter sample was enough for the sample to maintain its shape while being prepared for the isopress. Eliminating the isopressing step resulted in large cracks during sintering as in Figure 3.2c.

The sample is then sintered in the oven at 1350°C for 10 hours. Initially, it was found that the samples cracked during the sintering as in Figure 3.1b,c. This problem was solved by reducing the residual stresses in the material during pressing as discussed earlier. Reducing the rate of heating and cooling during sintering, also lowers any thermal stresses in the sample and reduces cracks. Thus, the heating and cooling were performed at a rate of 5°C/min which was the slowest possible speed given the available equipment.

Initial samples also exhibited some weight loss, along with some porosity near the edges, as in Figure 3.1d. Since lead is the most volatile of the constituents of the ceramic, it is reasonable to assume that this was caused by evaporation of lead during the sintering process. Several approaches were taken to reduce the lead loss. The first was to reduce the duration of the sintering process (the length of time at 1350°C) to 5 hours. The second was to attempt to contain the lead by using closed crucibles. A lead atmosphere in a closed crucible would prevent the evaporation of lead from the sample. Some of the arrangements attempted are sketched in Figure 3.2. Placing the sample in a closed crucible was not enough to reduce the lead loss. To increase the partial pressure of lead in the crucible, various amounts of PbO powder were also placed in the crucible. It was found that due to corrosive nature of lead, high-alumina crucibles with low porosity which are highly resistant to chemical attack needed to be used. Also, the PbO powder had to be physically separated from the sample, to prevent diffusion of lead into the sample which caused non-uniform samples. This was accomplished by placing the sample upon a platform above the PbO powder. The platform was made from the same material as the crucibles and had holes to permit exchange of lead vapor. Finally, the sample itself was buried in PbLaZrSnTi powder to achieve as homogenous a sample as possible.

Sintered samples were then sliced using an ID saw at Staveley Sensors Inc.†. Most samples were sliced to either 15 mil or 12 mil thickness. Each wafer was then coated on both sides with aluminum to serve as electrodes. Thermal evaporation was used to deposit the aluminum to a thickness of 3000 Å.

Once the wafers have been electroded, they are ready to be subjected to various characterization experiments, or used for actuation purposes as discussed in the following chapters.

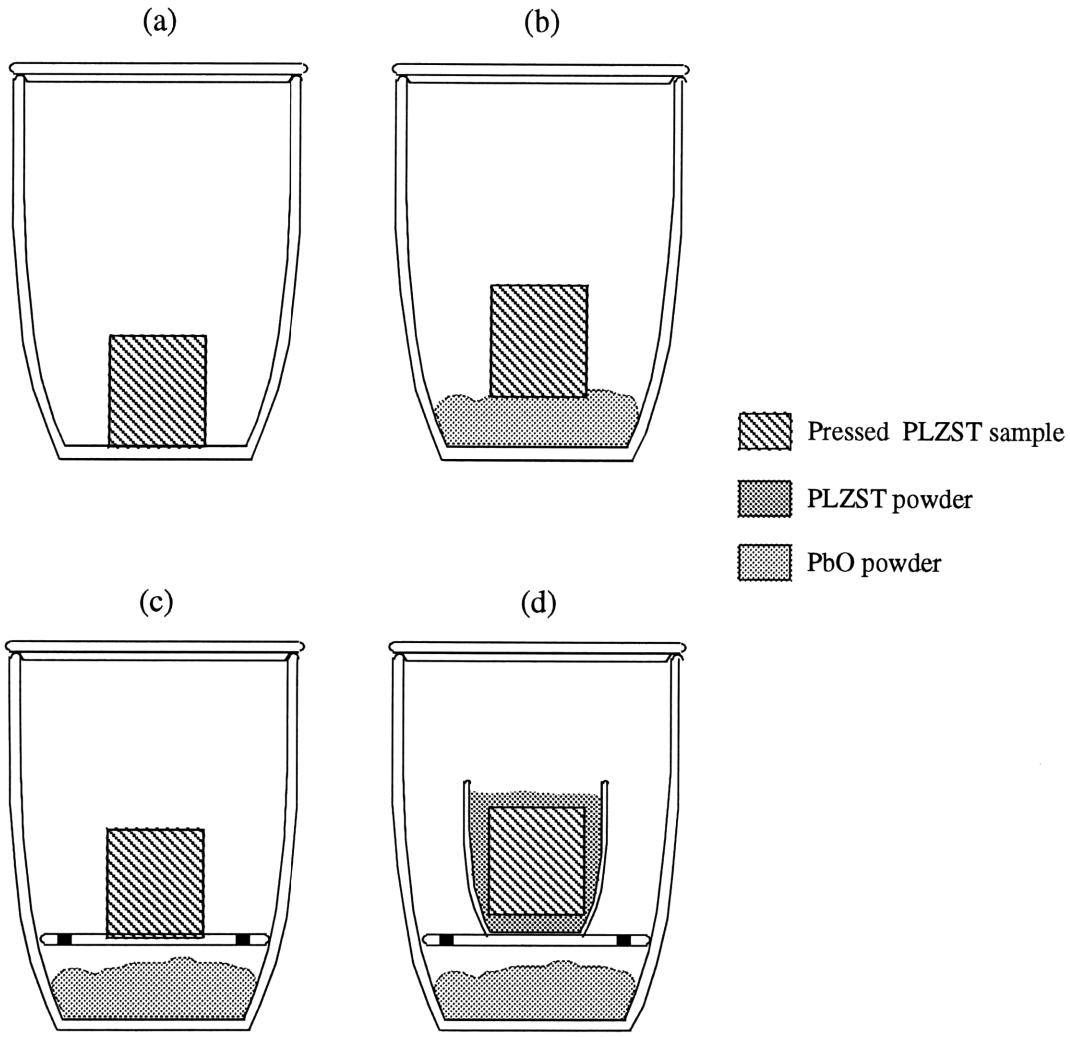

Figure 3.2 - Closed crucible arrangements used in order to reduce Lead loss during sintering. (a) sample in closed crucible. (b) addition of PbO to increase lead partial pressure. (c) use of a platform to separate sample from PbO. (d) burying the sample in PLZST powder.

† East Hartford, CT, U.S.A., Tel: (203) 289-5428.

4 EXPERIMENTAL RESULTS

The materials were characterized through a series of tests. The tests generally entailed the application of an electric field to the sample and the measurement of the resultant strain under different conditions. Data was obtained under a range of temperatures, and actuation frequencies. Behavior under structural stress was assessed by testing partially clamped samples. Also, the shape memory properties of the material were studied through the application of electric field waveforms containing pulses. The data from these tests is presented in the following sections.

4.1 Experimental Setup

To measure the transverse strains, a strain gage was bonded to the surface of each sample. A dummy strain gage was used in each case as part of the Wheatstone bridge in order to compensate for the effects of temperature drift. Measurements Group model 2120 or 2120A strain gage conditioners were used to balance the gages and amplify the signal.

In some experiments, the longitudinal strain was also measured. Since it was not feasible to use a strain gage for this purpose, a Zygo Axiom 2/20 interferometric system was utilized to obtain longitudinal displacement of the sample surface. Based on the sample thickness, longitudinal displacement measurements were converted to strain values. The experimental apparatus for obtaining simultaneous transverse and longitudinal measurements is shown in Figure 4.1.

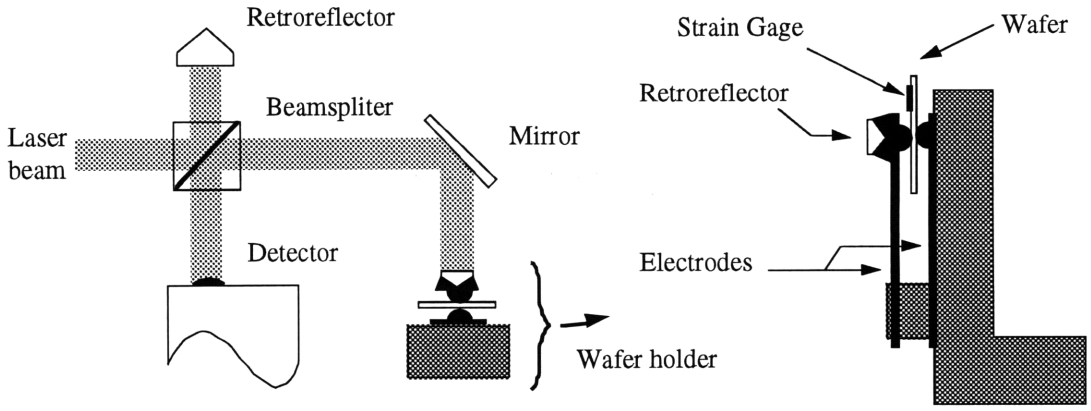

Figure 4.1 - Experimental setup used for simultaneous measurement of transverse and longitudinal strain. An interferometer provides longitudinal measurements, while a strain gage provides transverse measurements.

Electric fields were applied to the sample through the same leads which hold the sample in place. Since the samples could not be sliced to thicknesses lower than 10 mil using the available equipment, a high voltage power supply was needed to generate sufficient voltage for phase transition to occur. A Trek 633A high voltage power supply in conjunction with a Trek 622 amplifier was used for this purpose. The power supply is capable of supplying up to 10,000 volts at 20 mA. The input to the amplifier was generated using a Philips PM5138 function generator, or a computer, depending on the experiment. The amplifier also permits monitoring of the current supplied to the sample. The current can be recorded and then integrated numerically to obtain a measurement of the electric displacement and hence polarization of the sample.

$$D = \frac{Q}{A} = \frac{1}{A}\int I\,dt \tag{4.1}$$

All Data was recorded using the National Instruments MIO-16 data acquisition board installed in a Macintosh Quadra 950. The acquisition software was written in Labview.

Some of the tests were performed with the sample submerged in silicon oil. A Neslab EX-250 high temperature bath was used for this purpose. The oil has a higher dielectric breakdown than air. Thus, submerging the sample in oil reduces arcing across the electrodes. This allows application of electric fields with higher amplitude and/or frequencies. The oil also improves the thermal stability of the sample's environment during the test. The Neslab bath is also equipped with a controller for adjusting the temperature of the oil bath.

4.2 Free Strain Tests

The first series of tests was the measurement of transverse and longitudinal strains in the ceramic wafers, under an applied electric field. Characteristic field-strain curves for the A1, A2, A3 and B1 compositions are shown in Figures 4.2-4.5. These curves correspond to an electric field with a triangular waveform at 0.05 Hz. The first two compositions (A1 and A2), display purely ferroelectric response (at 23°C). As expected for a ferroelectric material, the transverse strain curves were similar in shape to the longitudinal strain curve, but with opposite sign. A3 and B1 demonstrated antiferroelectric-ferroelectric switching. For electric fields limited to 2.2 kV/mm the longitudinal strains of approximately 2200 $\mu\varepsilon$ and 2700 $\mu\varepsilon$ were attained by A3 and B1 respectively at room temperature. Note that the strain associated with both of these samples has the same sign in the longitudinal and transverse directions, indicating the phase transition is the dominant mechanism for creating strain. It should be noted from the slope of the longitudinal curves in Figures 4.2-4.5 that the strains have not saturated. Higher strains could be achieved by applying larger electric fields. However, To avoid arcing across the sample at higher electric fields, the samples had to be submerged in silicon oil. Thus longitudinal strains could not be measured using the interferometric system.

An interesting observation made during experiments was that a virgin antiferroelectric sample required much higher electric field for the first phase transition than subsequent phase transitions. A sinusoidal electric field was applied to a sample, with the amplitude gradually increased to 2.9 kV/mm, held for several cycles, and then gradually decreased to zero (Figure 4.6). The resulting strains were measured. Figure 4.7 shows the amplitude of the strain computed during each half cycle and plotted against the amplitude of the electric field. It can be seen from the longitudinal strain plot, that the A3 sample did not undergo a phase transition until the electric field exceeded 2.7 kV/mm. Once the first transition has occurred however, transitions continue to be observed even as the electric field amplitude is lowered to 1.7 kV/mm. The cause of this phenomenon is unclear. It is most likely caused by the initially random polarization of the various domains. Microcracking in the ceramic may also be responsible. It can also be seen that the transverse and longitudinal strains do not show the first transition occurring at the same instant. This effect is most likely due to the non-collocated measurement of longitudinal and transverse strains. That is, different portions of the wafer may have undergone the transition at slightly different times.

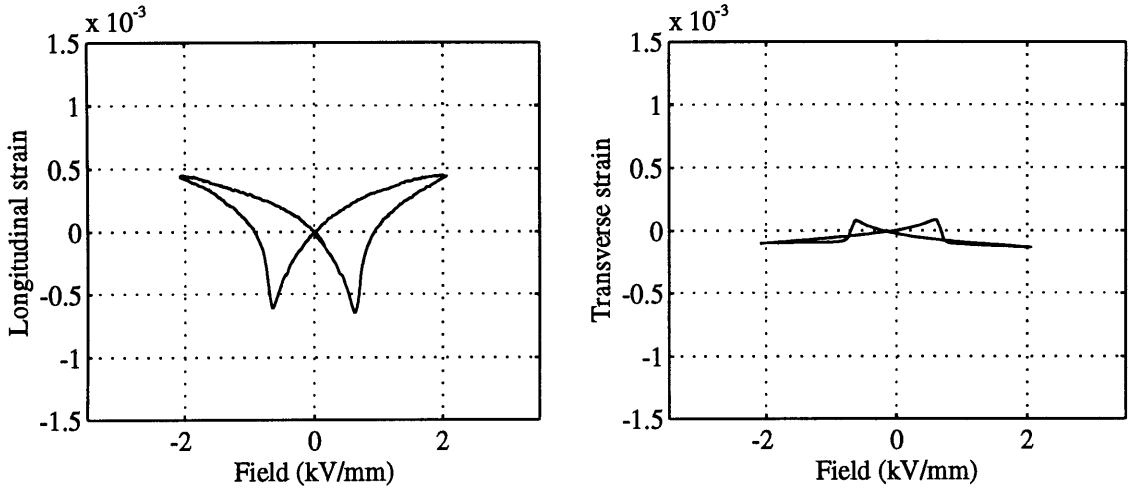

Figure 4.2 - Transverse and longitudinal field-strain curves for A1 ceramics.

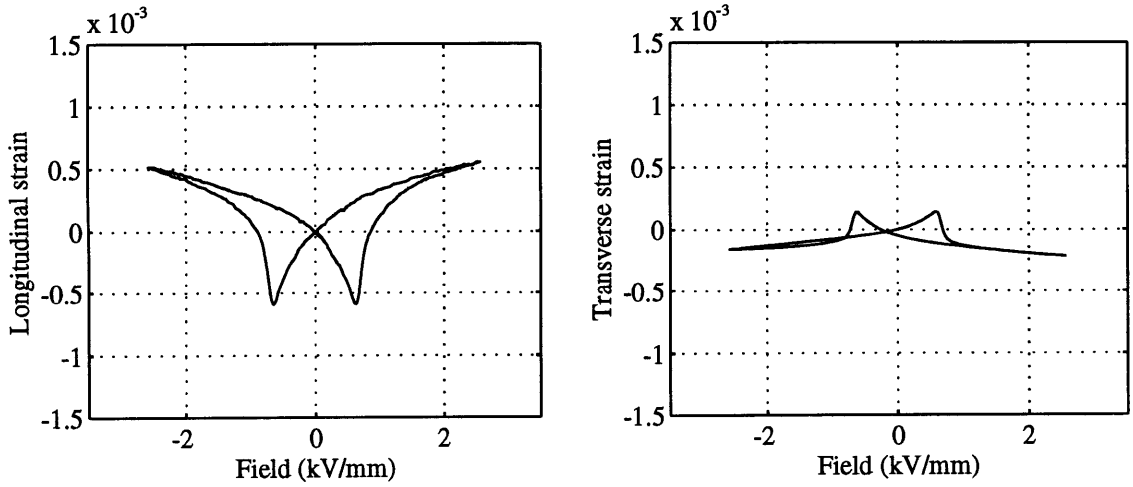

Figure 4.3 - Transverse and longitudinal field-strain curves for A2 ceramics.

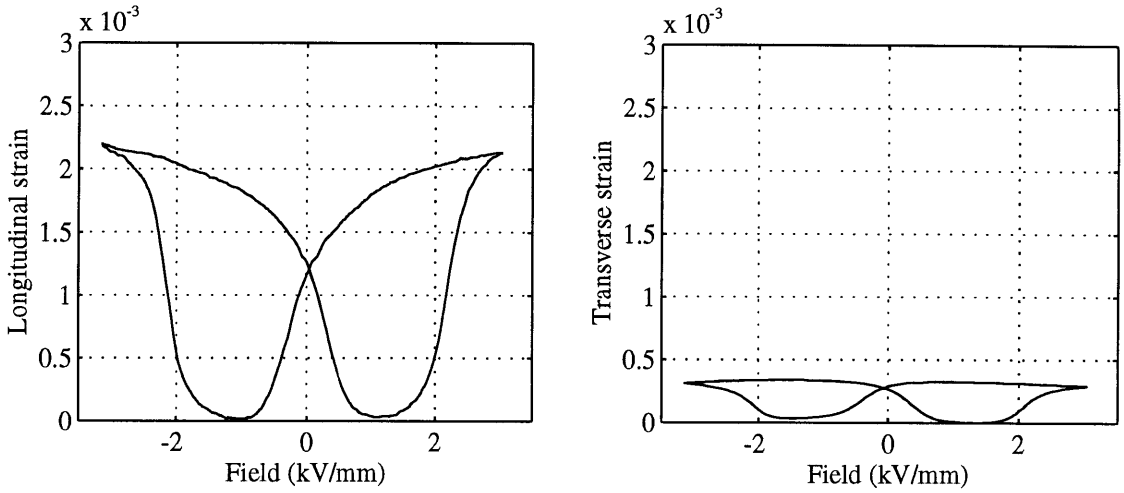

Figure 4.4 - Transverse and longitudinal field-strain curves for A3 ceramics.

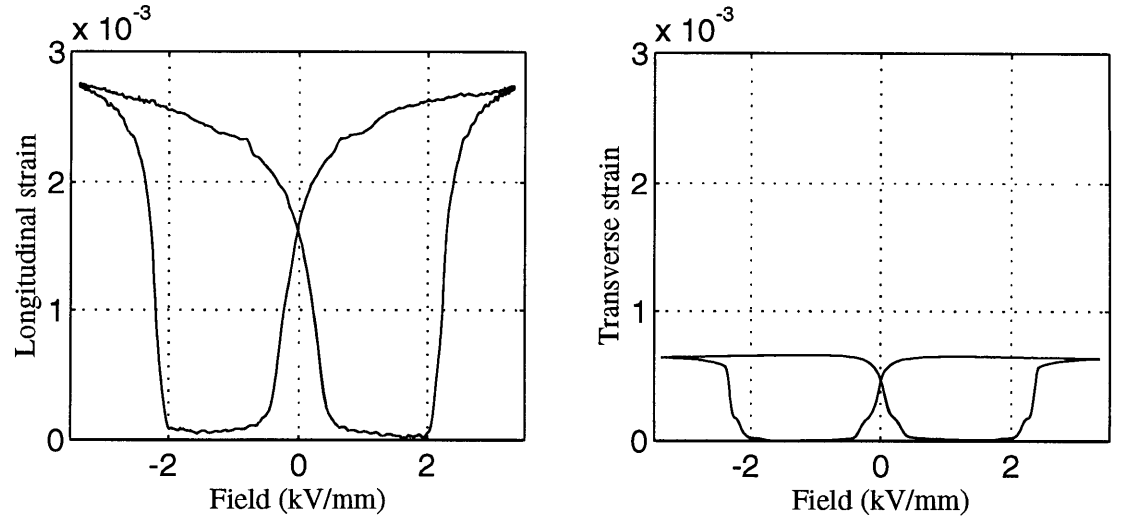

Figure 4.5 - Transverse and longitudinal field-strain curves for B1 ceramics.

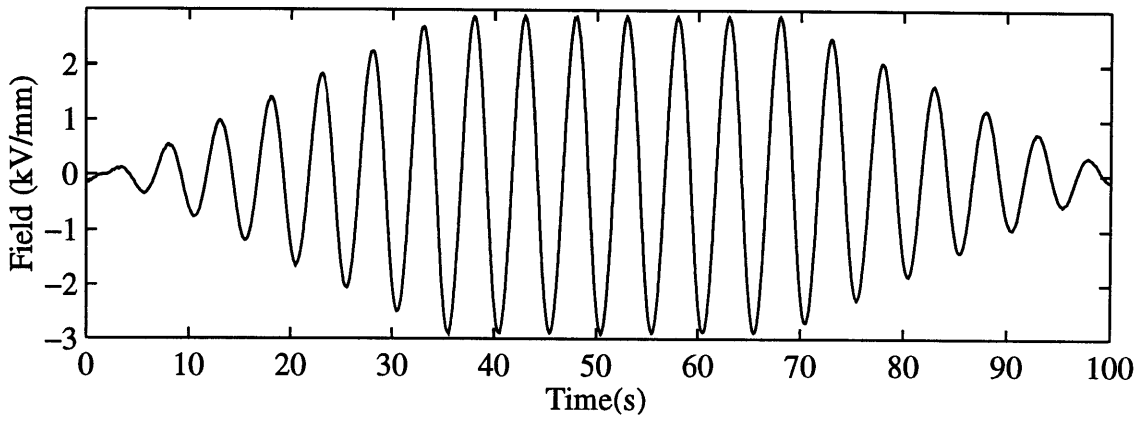

Figure 4.6 - The electric field waveform used to test a virgin sample.

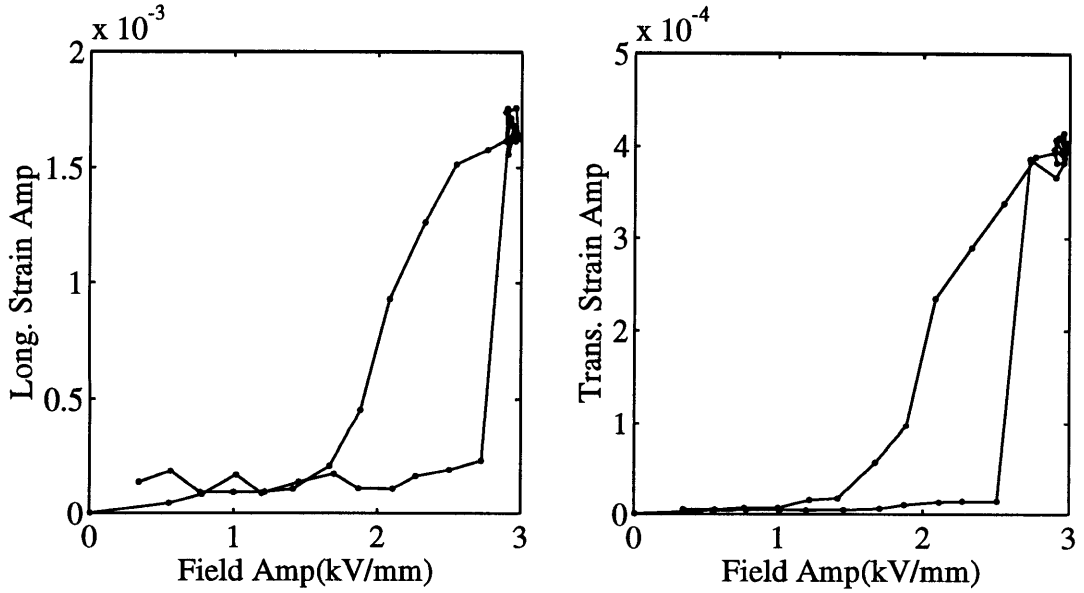

Figure 4.7 - Response of a virgin wafer of A3 material. The amplitude of strains are shown as the electric field amplitude is gradually increased and then decreased. As the electric field amplitude is increased again, the response follows the top curve in each plot.

It can be seen from the residual strain at zero field, in Figures 4.4 and 4.5, that both compositions A3 and B1 possess some shape memory. It should be noted that the transverse strain at zero field was as high as 75% of the peak strain. The longitudinal strain at zero field however, was much lower than the peak value. This results from the combination of the anisotropic ferroelectric strain and the isotropic strain associated with the phase transition. This may be understood by considering the strains as the field is reduced from its maximum amplitude to zero. In the longitudinal direction, the strain due to the phase transition and the strain due to the ferroelectric coupling between field and strain contribute to each other. As the field is reduced, the drop in the ferroelectric portion of the strain causes a large decrease in the overall strain. In the transverse direction, the ferroelectric portion of the strain has the opposite sign. Thus as the field is reduced, the strain actually increases (this is more evident in Figure 4.16). In either direction there is some drop in the strain which can be attributed to a fraction of the domains switching back to the antiferroelectric phase.

In a shape memory application, one is interested in having the actuator in either the AFE or FE phase at zero field. If the ceramic is used for longitudinal actuation one has to contend with the large overshoot in strain when the phase transition to FE phase is induced. In the transverse direction however, there is much lower overshoot. Hence transverse actuation is more suitable than longitudinal actuation if use of the shape memory effect is intended.

4.3 Temperature Tests

A series of tests was performed to characterize the behavior of the materials at different temperatures. The phase of the material is a function of its state. Along with the applied electric field, it is expected that quantities such as temperature and pressure will be among the state variables, forming a multi-dimensional state space for the sample. The composition phase diagrams in Chapter 2 (Figures 2.4 and 2.5) are merely cross-sections of this multi-dimensional space. Thus, one can think of the phase boundary shifting, as different cross-sections are viewed due to a change in temperature. Since the phase transition depends on the position of the specific material composition relative to the phase boundary, the behavior of the material depends on the operating temperature. This dependence has been investigated by conducting strain measurements at various temperatures in the range 0°C-50°C.

Figure 4.8 shows the transverse strain and the electric displacement of the B1 sample at four different temperatures. The sample was subjected to an electric field with a triangular waveform at 0.2 Hz, while being submerged in a temperature controlled oil bath. Longitudinal strain measurements with the laser were not possible because of the oil. Several effects can be observed from the transverse strain plots. As the temperature was decreased, the onset of the reverse transition (i.e. from FE to AFE) was delayed. Shape memory can only occur when the reverse transition has not occurred even when the field is returned to zero. Thus lowering the temperature improves the shape memory. Unfortunately however, this was accompanied by a drop in the overall strain associated with the phase transition. At low enough temperatures, the phase transition was inhibited altogether, and the material appeared to behave as a ferroelectric. This can also be seen from the plots of the electric displacement (or polarization). At high temperatures, two distinct hysteresis loops are observed, separated by an antiferroelectric region. As the temperature is decreased, the two loops merge together. At low enough temperatures, a single hysteresis loop is observed, and the material acts as a ferroelectric, switching between two poled states. Figure 4.9 shows the results of similar tests performed on A3 samples. Both similarities and differences were observed. As before, the polarization showed a single loop at low temperatures and a double hysteresis loop at high temperatures. Also, the strain associated with phase transition decreased as the temperature was lowered. However, a significant strain was still observed even at the lower end of the temperature range studied. The higher sensitivity of the Niobium doped composition to temperature is possibly related to the fact that the material is antiferroelectric for a smaller range of compositions (See Figures 2.4 and 2.5).

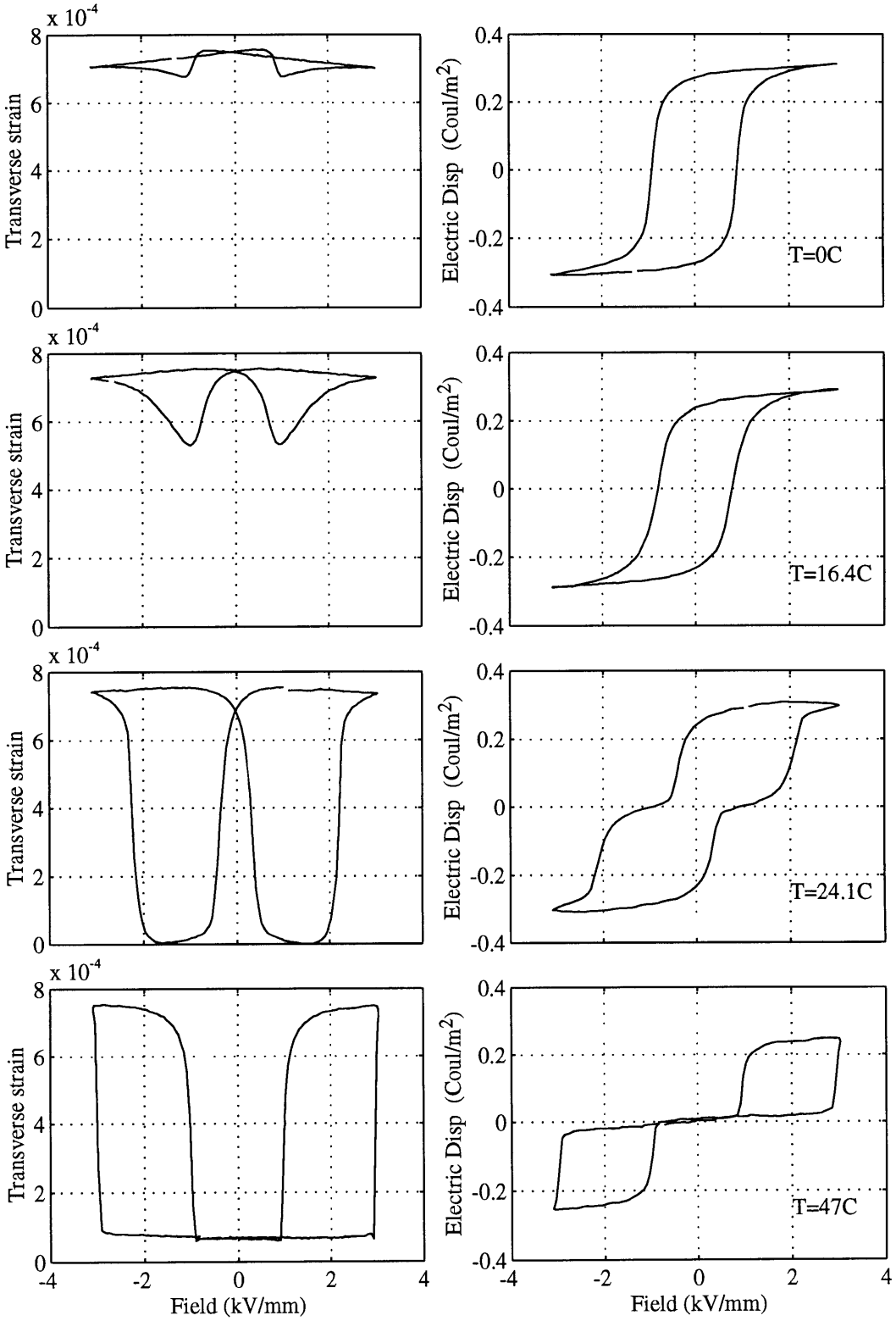

Figure 4.8 - Transverse strain, and electric displacement of the B1 sample at four different temperatures, under the application of an electric field with a triangular waveform at 0.2 Hz.

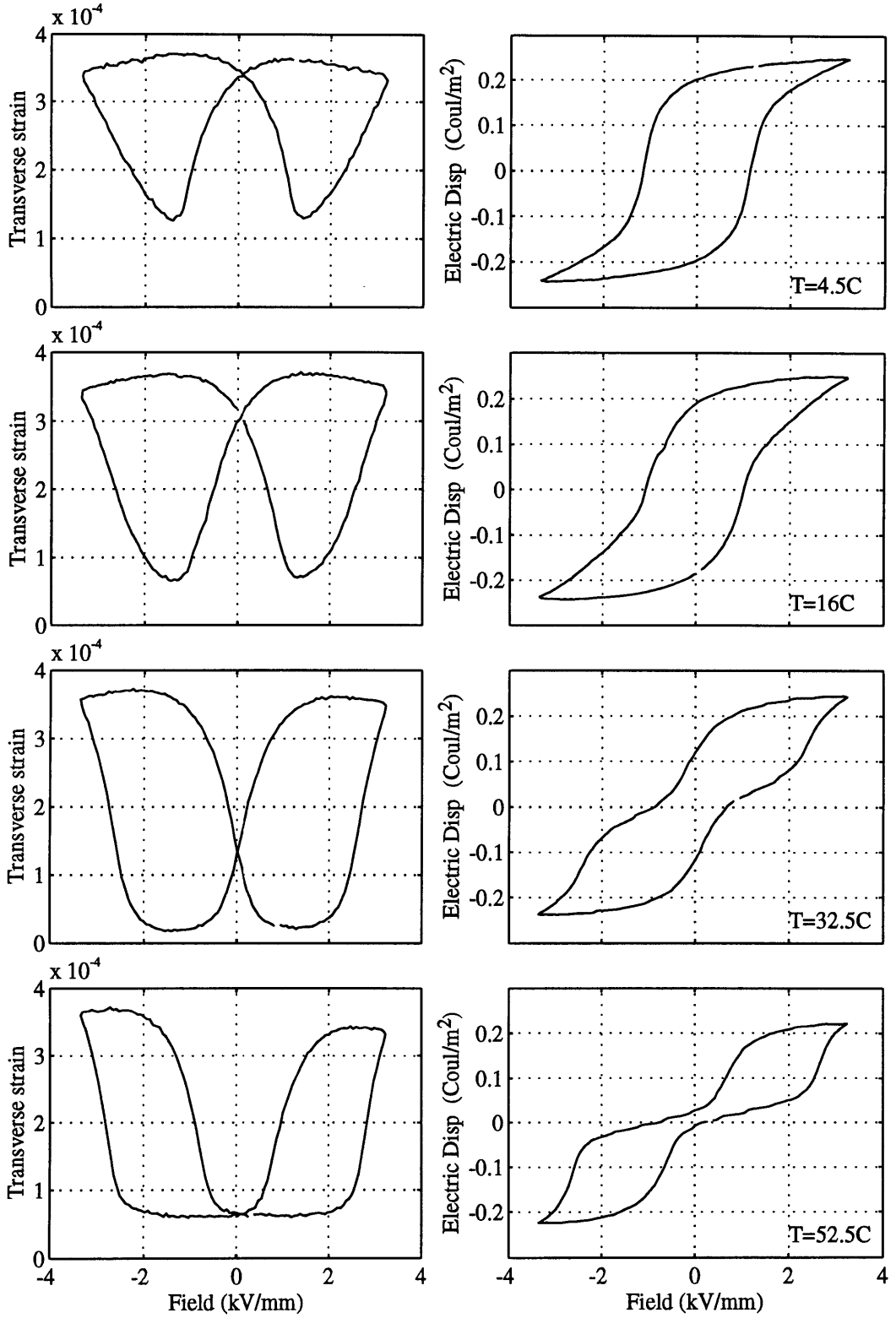

Figure 4.9 - Transverse strain, and electric displacement of the A3 sample at four different temperatures, under the application of an electric field with a triangular waveform at 0.2 Hz.

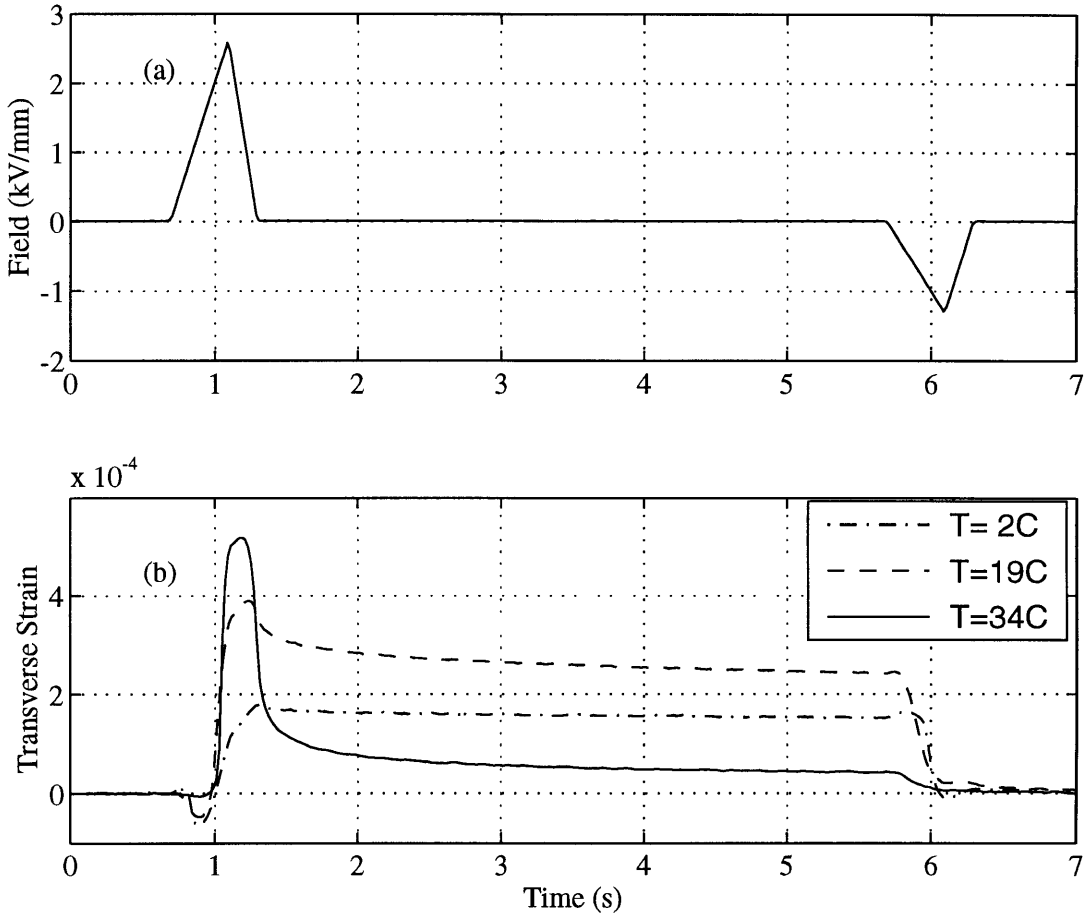

Figure 4.10 - The transverse strains in A3 sample arising from the application of the specified electric field at different temperatures.

The shape memory of the sample is seen more clearly in time domain tests. Figure 4.10b shows the strains in the A3 sample when applying an electric field with the time history shown in Figure 4.10a. The magnitude of the positive voltage pulse was selected to force transition from AFE to FE. The negative pulse was made just large enough to cause the reverse transition. Of interest are the strain levels while the electric field is switched off. Several curves are shown corresponding to different temperatures. It is immediately obvious that over the temperature range considered, the peak transverse strain increases with temperature. However, at higher temperatures the strain decays more rapidly. A small negative strain is also observed during the initial portion of the positive electric field pulse. This indicates that a small fraction of the material was still in the FE phase after the application of the negative pulse. This could be corrected by more careful choice of the amplitude used for the negative electric field pulse. Figure 4.11 shows the temperature dependence in more detail. The top and bottom curves display the maximum

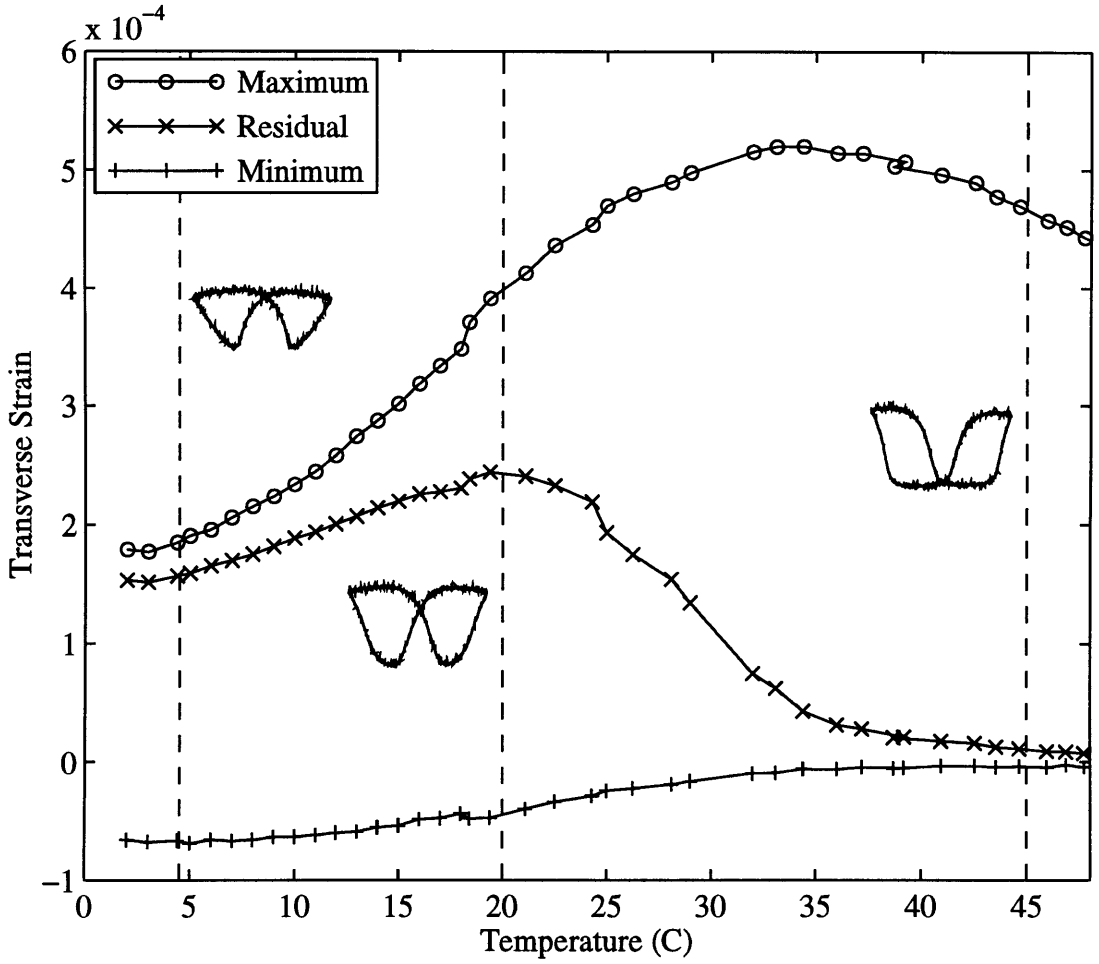

Figure 4.11 - Transverse strains of A3 sample during application of the electric field in Figure 4.10a. The three curves correspond to peak strain, minimum strain, and the residual strain after 4.5 seconds. The insets show corresponding field-strain curves at selected temperatures.

and minimum strains which occur during the application of the positive electric field pulse. The middle curve in the figure is the residual strain after the field has been off for 4.5 seconds and is a measure of the amount of shape memory present. This residual strain peaks around 20°C. The rapid decay at higher temperatures can be attributed to an increase in the thermal vibrations of the lattice, which reduce the stability of the FE phase at zero field. Clearly, as far as the memory in the ceramic is concerned, there is an optimal operating temperature where the magnitude of the residual strain is maximized. This optimal temperature can possibly be tailored for specific applications by making slight variations in the composition of the material. Figure 4.12 shows similar data for the B1

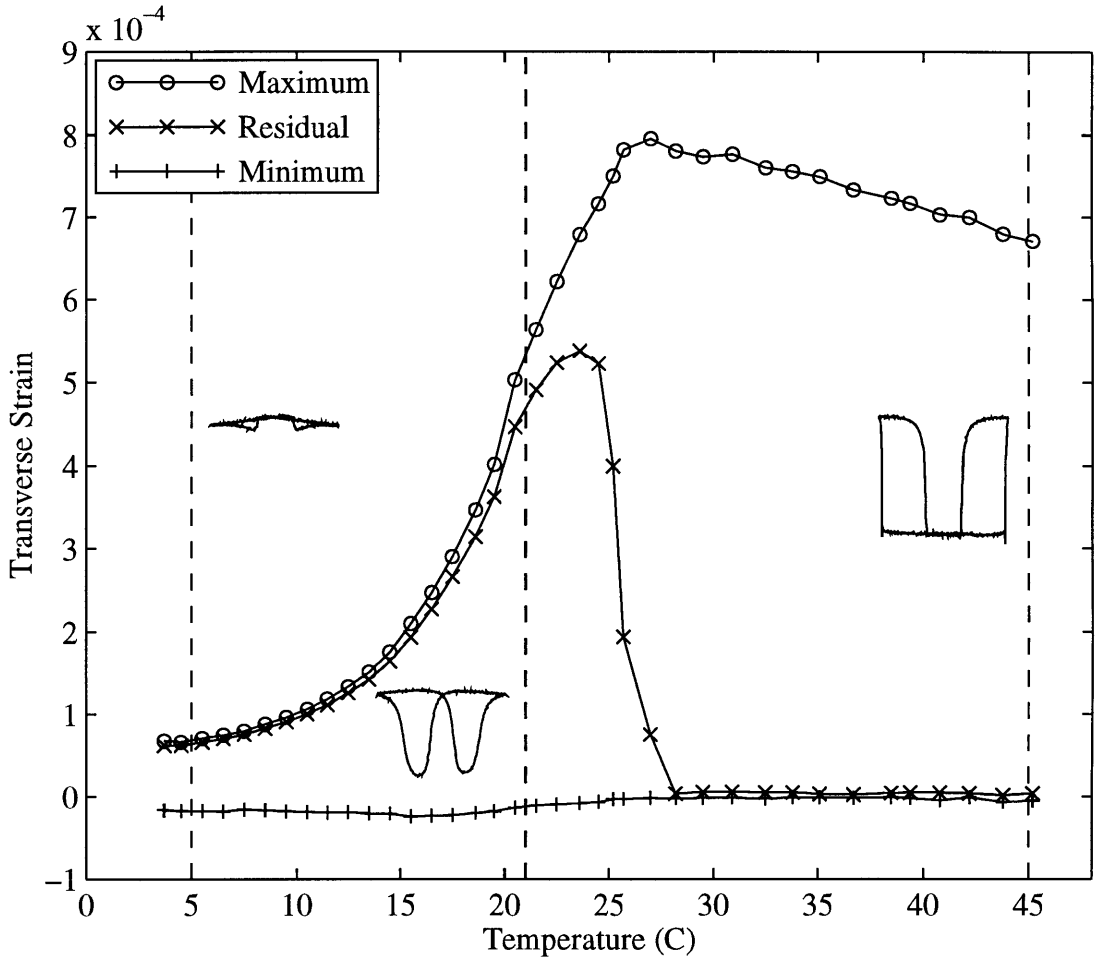

Figure 4.12 - Transverse strains of B1 sample during application of an electric field similar to Figure 4.10a. The three curves correspond to peak strain, minimum strain, and the residual strain after 4.5 seconds. The insets show corresponding field-strain curves at selected temperatures.

sample. This material exhibits more sensitivity to temperature as seen from the narrow peak in the residual strain curve. Its optimal operating temperature for shape memory is around 25°C.

The above results can be related to butterfly curves obtained at different temperatures. Field-strain curves at selected temperatures are superimposed on Figures 4.11 and 4.12. At high temperatures both materials undergo the reverse transition (i.e. from FE to AFE) before the electric field has returned to zero, and thus do not exhibit any shape memory. As the temperature was decreased, the onset of the reverse transition was delayed, increasing the observed residual strain. But as the temperature is decreased further the strain associated with the phase transition drops.

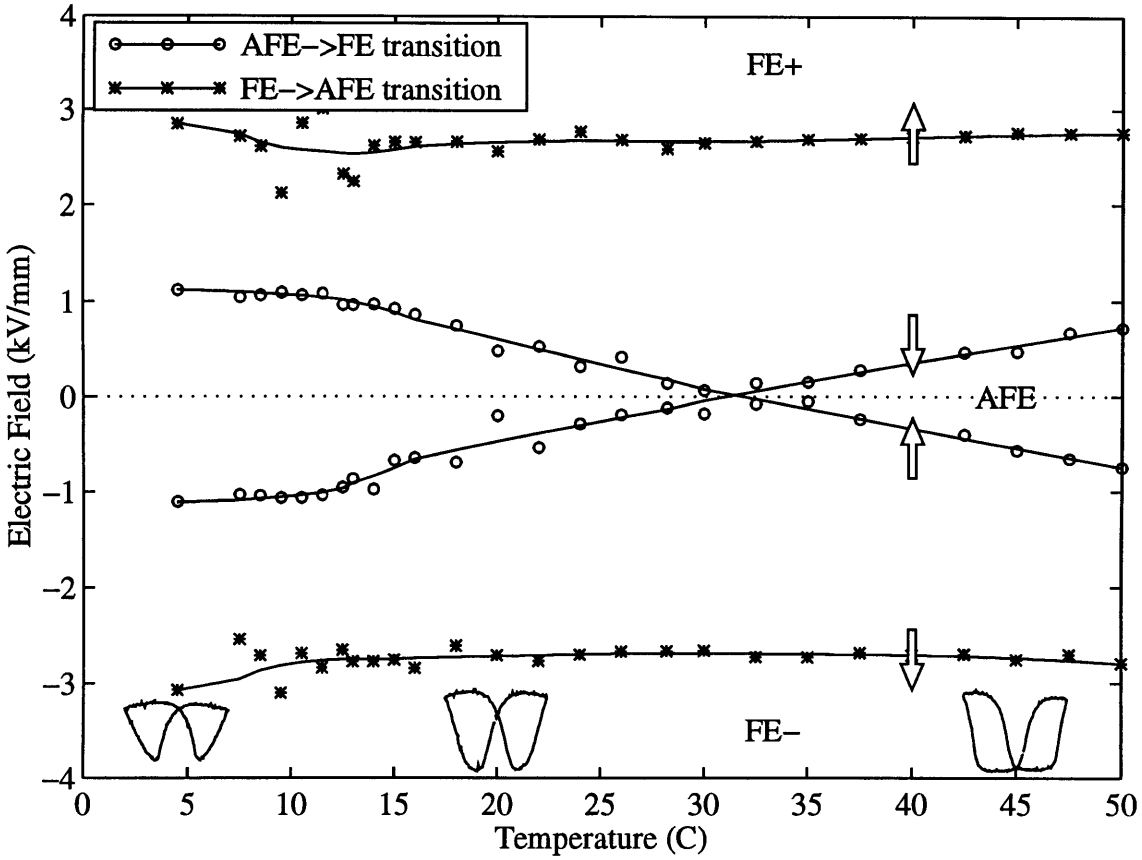

Figure 4.13 - Electric field-temperature phase diagram for the A3 sample. The insets show field-strain curves at 4.5°C, 20°C, and 45°C for reference.

An alternative way to look at the material behavior is using electric field-temperature phase diagrams for a given composition. These phase diagrams were constructed from the AC tests performed at various temperatures. The field-strain curves obtained at each temperature were used to determine the values of electric field at which phase transitions occurred. Since the transitions are not very sharp, the transition field level was defined to be the point at which the most rapid change in strain occurred. Two forward (AFE→FE) and two reverse (FE→AFE) transitions were identified at each temperature. This data can be displayed on a field-temperature phase diagram. Figure 4.13 is the phase diagram for the A3 material. In order to account for the hysteresis in the phase transition, the arrows indicate the direction in which each phase boundary is crossed. So for example, at 40°C, with the electric field increasing from -3 kV/mm, a reverse transition occurs at about -0.5 kV/mm, followed by a forward transition at 2.7 kV/mm. The other two phase boundaries are only seen while the electric field is decreasing. It can be immediately seen from such a phase diagram that the material has shape memory only for temperatures below 30°C. Below that temperature, the reverse transition does not occur unless a reverse field is

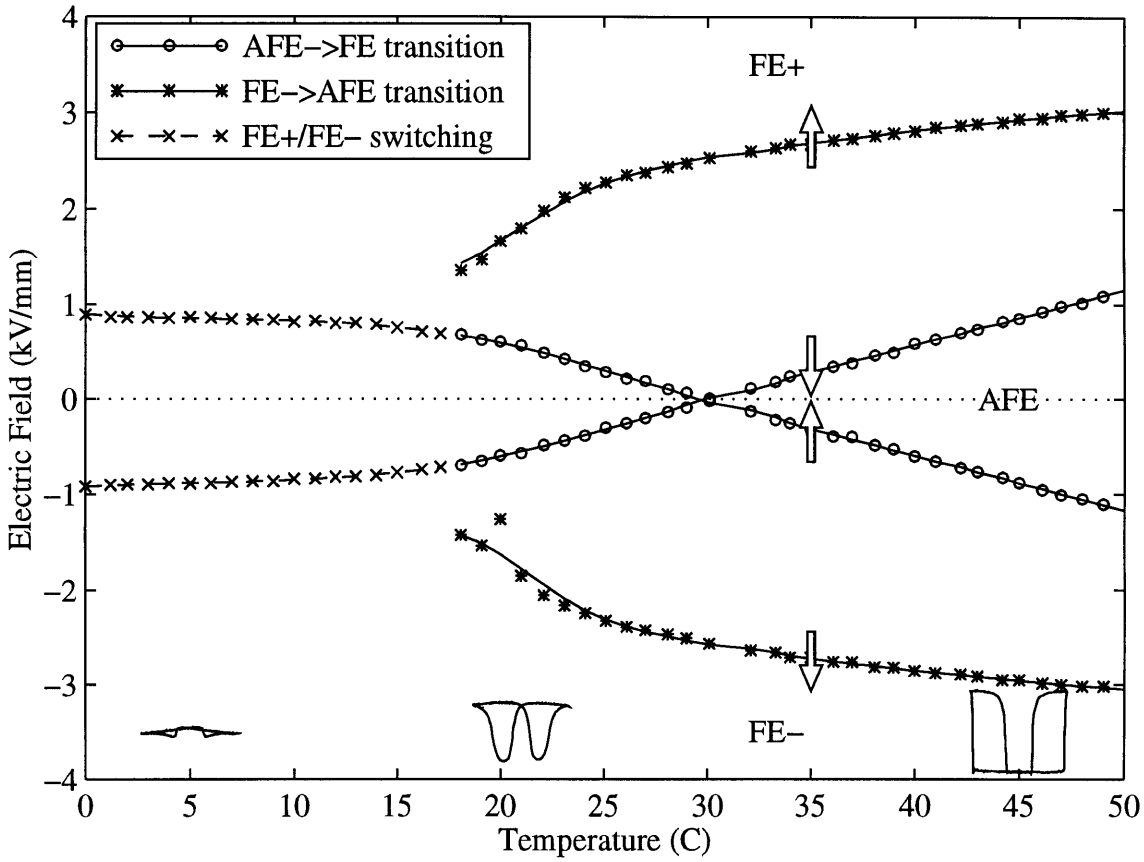

Figure 4.14 - Electric field-temperature phase diagram for the B1 sample. The insets show field-strain curves at 5°C, 21°C, and 45°C for reference.

applied. Figure 4.14 shows similar phase diagram for the B1 composition. Again, we see that the material has shape memory below 30°C. In this case however, at low enough temperatures no antiferroelectric phase is observed. The material behaves as a ferroelectric displaying polarization reversal due to application of large electric field. The AFE phase has effectively been frozen out. This occurs at approximately 17°C.

It is clear that the response of the material is sensitive to temperature. The field-temperature phase diagrams 4.13 and 4.14 can be used along with the strain-temperature plots 4.11 and 4.12 to determine the optimal operating temperature for each material. The choice of the optimal temperature will depend on whether the critical requirement for the application of interest is peak strain or shape memory.

4.4 Stress Tests

Another series of tests were aimed at determining the effect of induced stress on the samples. The effect of stress on the response of the material is of great concern when the material is used in structural applications. Two factors are of interest. First, the stiffness of the ceramic must be measured. The ratio of the actuator stiffness to the structure stiffness plays a major role in determining the actuator authority. In addition, it is necessary to ensure that structural stresses do not impede the phase transition in the actuator. Structural loading can also have an effect on the shape memory of the sample by inducing a reverse transition.

These effects could be investigated using a testing apparatus capable of applying specific loads to the samples. The small sample size and the brittle nature of the ceramics make the use of existing tensile testing machines impractical. It is, however, possible to obtain some of the desired information by testing the samples while bonded to a structure. Metal shims of various extensional stiffnesses were bonded to both sides of 15 mil thick wafers of the A3 sample (Figure 4.15). Figure 4.16 shows the observed transverse strains obtained under these partially clamped conditions, while applying an electric field with a triangular waveform. Curve (a) corresponds to a free wafer. Curves (b-d) are the transverse strains produced by wafers sandwiched between metal shims with properties listed in Table 4.1. An immediate observation is that under the stiffness ratios examined, phase transition was not impeded. The different curves all have the same shape, and are simply reduced in amplitude as the structure stiffness is increase. It should be pointed out that there were cases where the shape memory was inhibited due to structural backstress. For example, an 11 mil thick B1 wafer was partially clamped by bonding a 40 mil thick aluminum to each side. Figure 4.17 shows the transverse strain of this sample compared to one tested under free conditions. Note that due to the resulting stress in the partially clamped sample, the phase transition was not accompanied by the large strain observed under free conditions and no shape memory is observed.

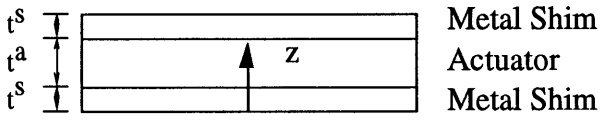

Figure 4.15 - Cross section of sandwich test samples.

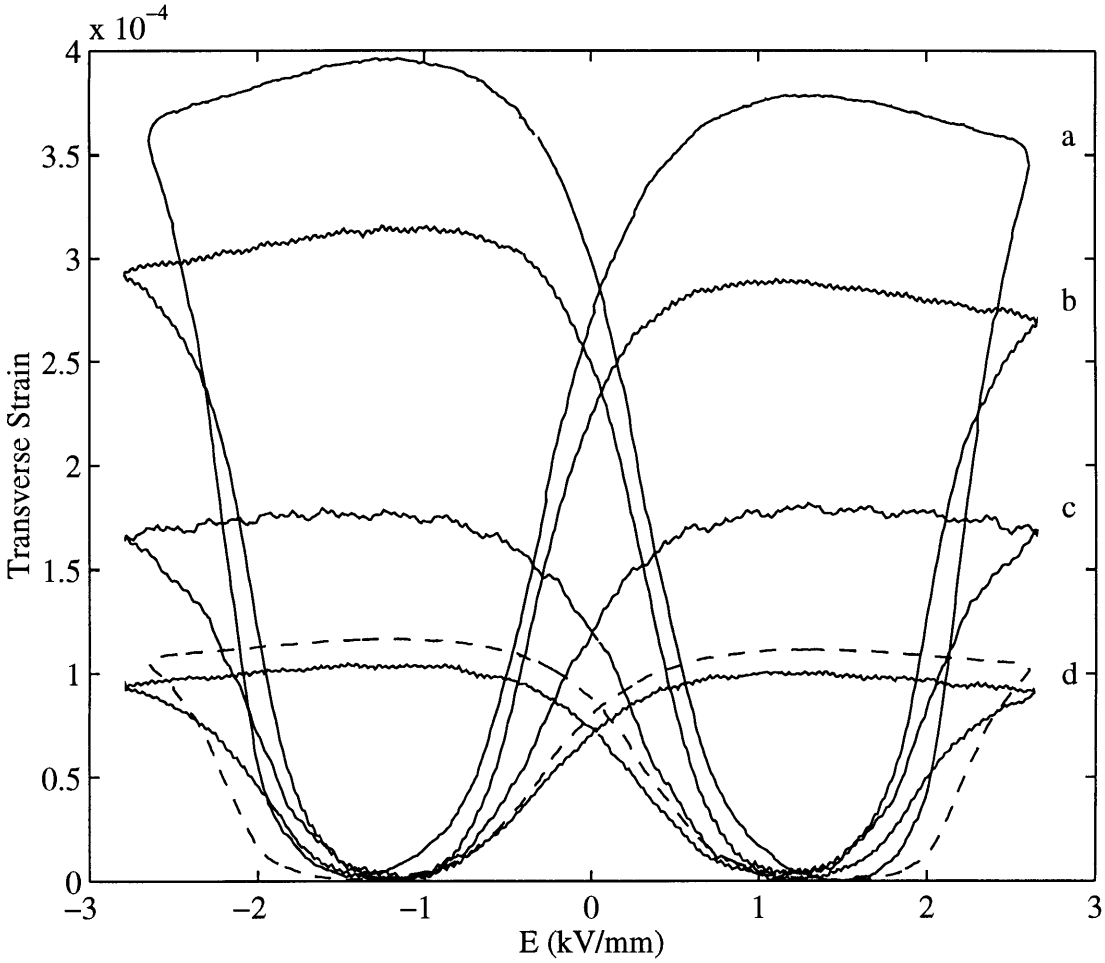

Figure 4.16 - Field-strain curves for partially clamped wafers: (a) free wafer. (b-d) wafer sandwiched between metal shims of increasing stiffness (See Table 4.1). The dashed curve shows predicted response using equation (A.21) corresponding to curve (d).

Table 4.1- Properties of the material used in performing partially clamped wafer tests.

	Material	E (GPa)	ν	t^s (mil)	$\psi^\dagger$
b	Brass	105	0.35	2.5	0.23
c	Steel	190	0.30	4	0.62
d	Aluminum	70	0.35	20	1.24

† ψ is the structure to actuator stiffness ratio as defined by (A.20). It is calculated using an effective actuator stiffness of c^a=116 GPa which was calculated as described later in the section.

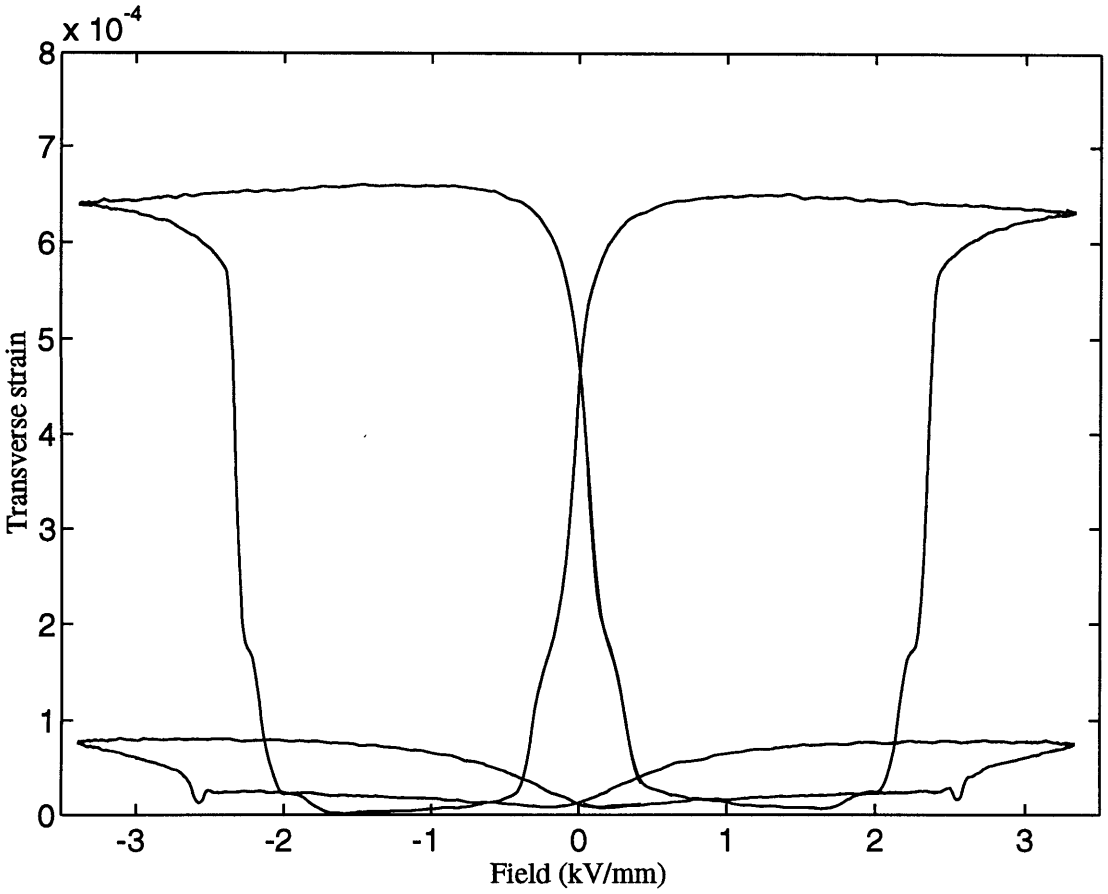

Figure 4.17 - Field-strain curves for wafers of sample B1 under free, and partially clamped conditions.

The data from these partially clamped tests can be used to approximate the stiffness of the ceramic while it is in the ferroelectric phase. The method for modeling the system using Classical Laminated Plate Theory with induced stresses is described in Appendix A.2. The approach assumes symmetry of the problem in the x and y directions, leading to effective extensional stiffnesses for the structure (c^s) and the actuator (c^a) being given by

$$c^s = c_{11}^s + c_{12}^s = E/(1-\nu)$$
$$c^a = c_{11}^a + c_{12}^a$$

where c_{ij}^a and c_{ij}^s are the stiffness constants for the actuator and the structure under plane stress assumptions. E and ν are the Young's modulus and Poisson's ratio for the structure. Solving the system for the transverse strain in the sandwich sample, equation (A.21) is obtained:

$$S^o = \frac{\Lambda}{1+2\psi} \tag{A.21}$$

where S^o is the observed transverse strain of the structure and Λ is the transverse strain which the ceramic actuator would have experienced under free conditions. ψ is the structure to actuator stiffness ratio in terms of the effective extensional stiffness and the thickness of each layer as defined by (A.20).

With Equation (A.21) a least squares fit can be performed to obtain an estimate of c^a as follows. Multiple sandwich samples with different effective structure stiffnesses are used. For each sample, the ratio of Λ to S^o at a given electric field level is measured and plotted against $2t^s c^s/t^a$ as in Figure 4.18. The slope of the best fit line then corresponds to $1/c^a$. Using the value of strains corresponding to an electric field of 1 kV/mm from Figure 4.16, a value of 116 GPa was calculated for the stiffness ($c_{11}+c_{12}$) of A3 samples. To decouple the c_{11} and c_{12} values, one would need to assume a value for the Poisson's ratio of the material, ν. However, since the model only makes use of the sum of c_{11} and c_{12}, this is not necessary. The dashed curve in Figure 4.16 shows the free strain data scaled according to (A.21) for the stiffness ratio corresponding to curve (d) of Figure 4.16. Reasonable agreement between the two curves is observed.

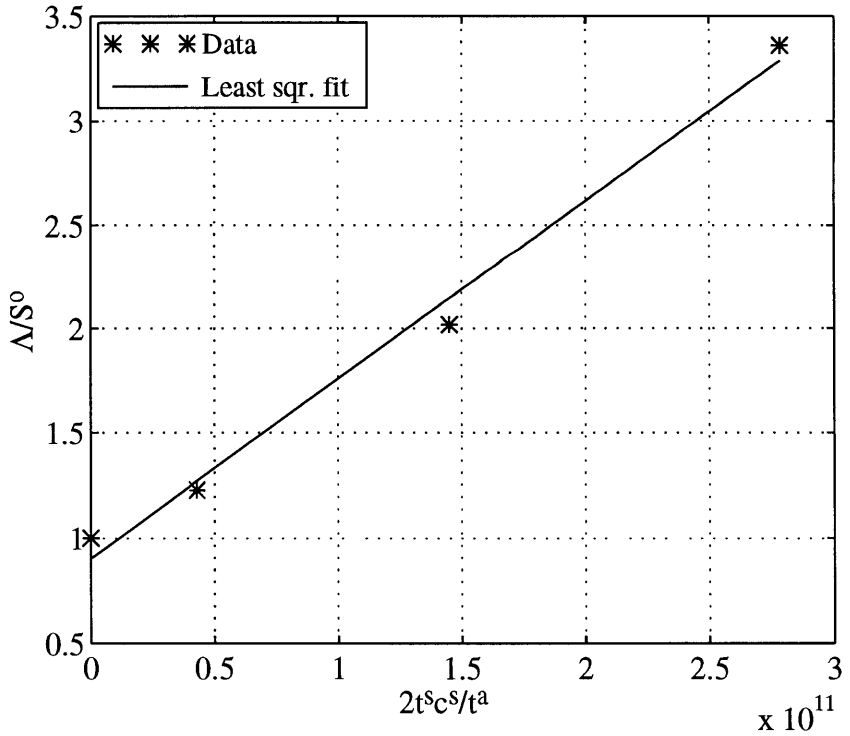

Figure 4.18 - Least squares fit used to determine effective ceramic stiffness.

4.5 Frequency Tests

The final series of tests performed on the samples involved obtaining strain data using electric fields with different frequencies. A triangular waveform was used. Since the material response is nonlinear, there would be no particular advantage in using sinusoidal excitation. Triangular waveforms, however, make it possible to see the dependence of strain on the rate of change of electric field more clearly.

The current required by the sample increases with frequency. This is to be expected, since the charge required during each cycle has to be supplied in a shorter period of time at higher frequencies. To increase the maximum frequency attainable given the current limitations of the power supply (20 mA), the area of the samples were reduced as much as possible. The maximum frequency attained during the tests was 20 Hz. Arcing across the electrodes was also found to be a problem during tests at high frequencies. To prevent arcing, samples were submerged in silicon oil. Also, some of the electrode was removed from the edges of the samples. Thus, on a 14 mm by 7.5 mm sample, only a 13 mm by 6.5 mm area was electroded.

It should be noted that the hysteresis of supplied current with voltage implies a power dissipation in the sample. This causes a rise in the sample temperature at higher frequencies. Since it is of interest to separate the effects of temperature and frequency, the oil temperature was adjusted during the experiment to maintain the wafer at approximately 26°C. Figure 4.19 shows some of the field-strain curves obtained from these tests. The strain amplitudes attained at each frequency are plotted in Figure 4.20. The peak strain appears to decrease almost linearly with the log of frequency. The slope discontinuity at 10 Hz is caused by current saturation in the amplifier. It should be noted that even at the lowest frequency, the strain amplitude is lower than the strain shown in Figure 4.11 at the same temperature. This is due to the clamping caused by the unactuated region around the edge of each sample, where the electrodes were removed.

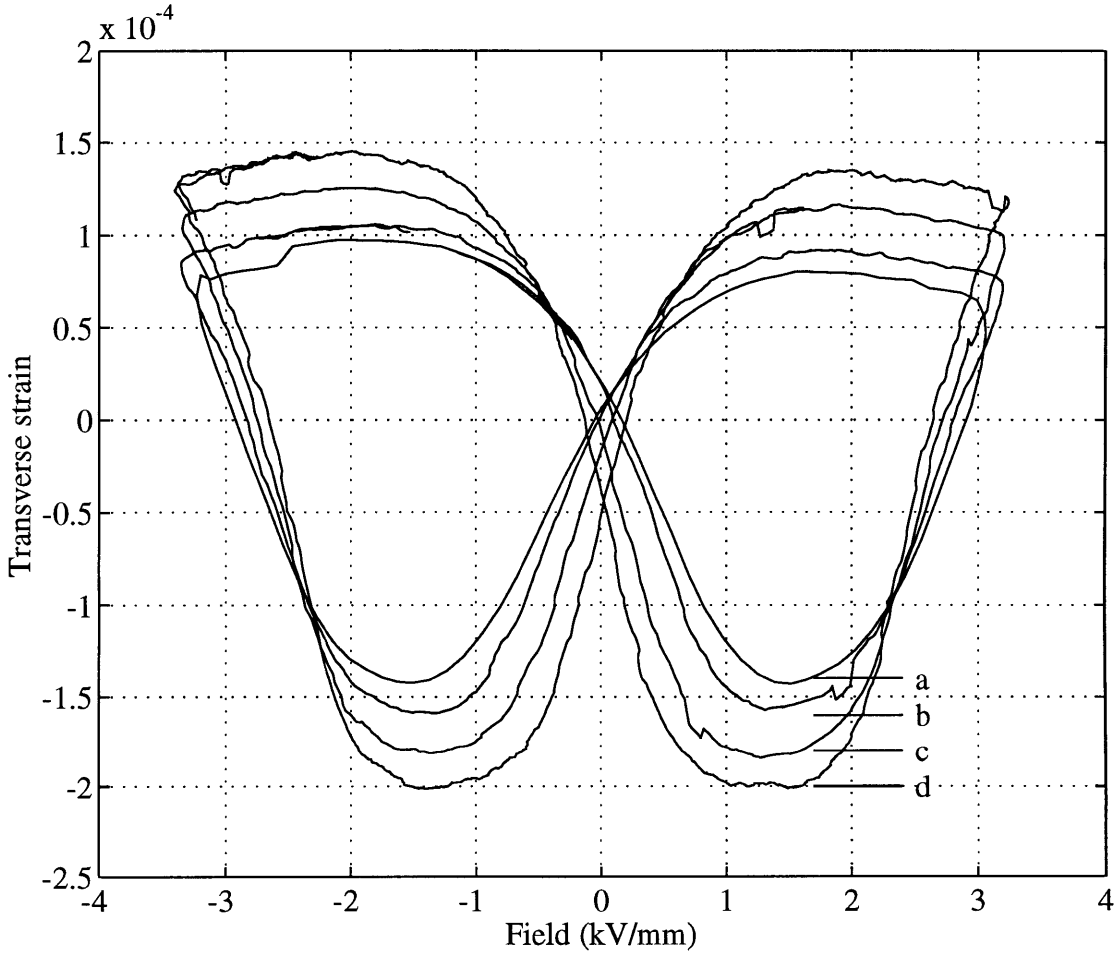

Figure 4.19 - Field-strain curves produced by a triangular electric field of amplitude 3.2 kV/mm at the frequencies: a) 20 Hz, b) 2 Hz, c) 0.2 Hz d) 0.02 Hz.

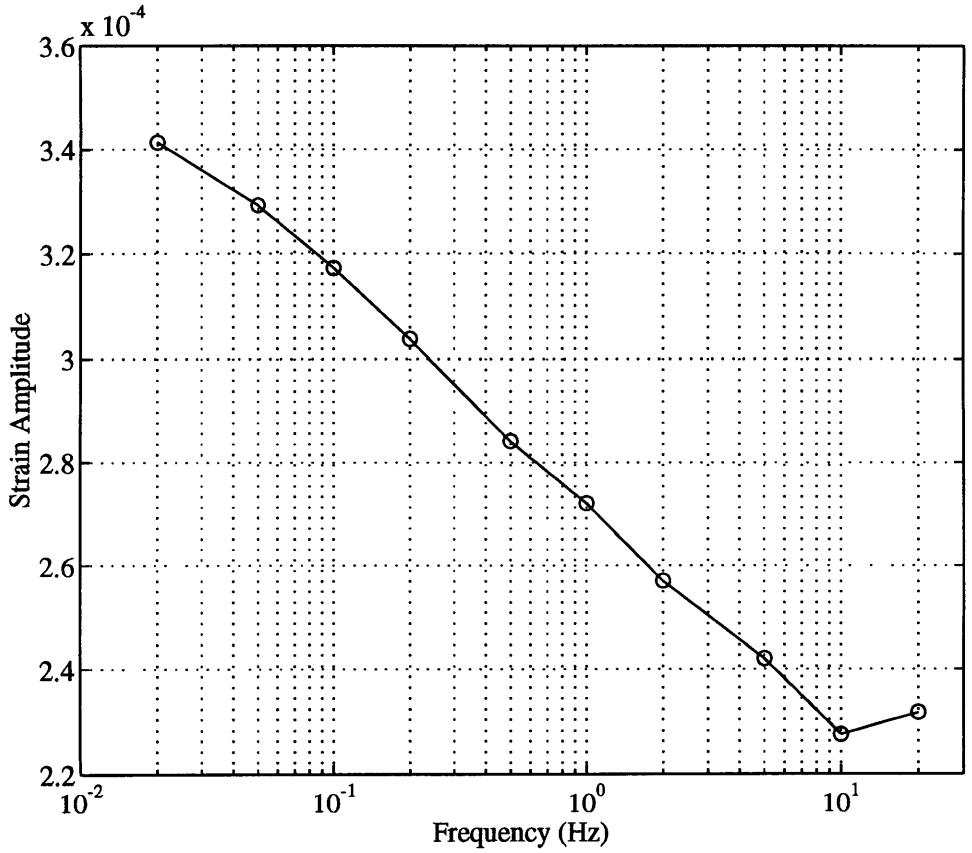

Figure 4.20 - Peak transverse strain in the ceramic wafer produced by a triangular electric field of amplitude 3.2 kV/mm at different frequencies.

4.6 Summary of Experimental Results

Of the several compositions tested during this study, only the B1 and A3 compositions exhibited AFE-FE phase transitions at room temperature. With electric field magnitudes of 3.2 kV/mm the longitudinal strains of approximately 2200 με and 2700 με were produced by wafers of A3 and B1 compositions respectively. The corresponding transverse strains were approximately 400 με and 650 με respectively.

The material response was found to be quite sensitive to changes in temperature. In both samples the transition field levels varied with temperature. Thus reducing the temperature resulted in improved shape memory (reduction of the residual strain decay rate). Unfortunately however, the overall strain also decreased with temperature. At higher temperatures more strain was observed, while the residual strain decayed more rapidly. The B1 samples appeared to be much more sensitive to changes in temperature. Using some of the strain-temperature curves obtained from experiments, it is possible to determine the optimal operating temperature for each composition, to either maximize peak strain or residual strain. For the A3 samples maximum peak strain was observed at 34°C and maximum residual strain was observed at 20°C. For the B1 samples maximum peak strain was observed at 27°C and maximum residual strain was observed at 24°C. It is likely that this optimal temperature can be tailored for specific applications by slight variations in composition.

The effect of induced stress on the observed strain was investigated by testing samples which had been bonded to metal shims of various thicknesses. For sufficiently small structure to actuator stiffness ratios, the phase transition was not inhibited by stress. The data obtained from the tests was used to obtain an effective in-plane extensional stiffness for the material. This stiffness can be used along with Classical Laminated Plate Theory to predict the observed strains when the ceramic is bonded to a structure.

The material response was also measured at different frequencies. As expected, the observed strain decreases as the frequency of excitation is increased. It was also found that due to the power dissipation in the actuator, heating of the sample should be an important consideration in any application.

5 MATERIAL MODELING

One of the goals of the present work has been to obtain a model for the behavior of shape memory ceramics. One may take either a microscopic or a macroscopic approach to the problem of modeling the behavior of any active material. In a microscopic approach, the interactions are modeled at the atomic level. The behavior of the material is then derived based on those interactions. Such models are useful in gaining understanding of the physical origins of the material behavior, and the phenomena associated with phase transition. However, one can generally only model simple crystal structures with such an approach. Furthermore, it is difficult to obtain good agreement between model and experiments The phenomenological modeling focuses on predicting the response of the material without any explicit modeling of the underlying mechanisms. However, insight into the nature of such mechanisms is utilized to guide the development of the model. Since phenomenological models can be matched with experimental data more closely, they are usually more useful for engineering applications. For this reason, a phenomenological approach was taken in modeling shape memory ceramics in the present work.

The next section summarizes three examples of phenomenological models found in the literature for materials undergoing phase transition. The model developed for shape memory ceramics, is then presented in §5.2.

5.1 Modeling Approaches in Literature

Over the years, numerous models have been proposed for describing the behavior of materials which undergo internal transitions. For example, models for shape memory alloys have been proposed by Rogers [21], Hoffmann [16], and Cory [9,22]. These

theories include completely phenomenological models as well as more theoretical models based on non-equilibrium thermodynamics. Various models have also been proposed for describing the phase transition in electroceramics [12,24]. These models take a thermodynamics approach and describe the phase transition by obtaining a phase diagram for the material. While these models are capable of predicting the phase transition, they do not deal with the rate of the transition or the relation of the transition to stress and strain in the material. A model for the behavior of ferroelectrics, accounting for the dependence of the transition on the applied field and incorporating the constitutive relationship for the material, has been developed by Chen and Montgomery [8]. Another model for ferroelectrics also incorporating constitutive relations has been proposed by Chan [7]. This model accounts for the ceramic structure by modeling multiple crystalline domains. In the following subsections the Rogers model, the Chen and Montgomery model, and the Chan model are summarized.

5.1.1 Rogers' Model for Shape Memory Alloys

As mentioned in previous chapters, there are several similarities between shape memory alloys and shape memory ceramics. In both materials the dominant source of actuation strain is a phase transition. In shape memory ceramics the strain is brought about by an electric field induced transition from the FE to AFE phase. In a shape memory alloy such as Nitinol, the strain is caused by a thermally induced phase transition from austenite to martensite. Furthermore, in both material, the metastability of either phase leads to the presence of shape memory behavior. As such, the models used for describing shape memory alloys are of some relevance to shape memory ceramics. This section summarizes one of the phenomenological models for shape memory alloys, which has been proposed by Rogers [21].

This is a one dimensional model which applies to SMA fibers or wires. The model utilizes an internal variable ξ which represents the martensitic fraction. The constitutive relation for the material is written in terms of this internal variable as:

$$\overline{\sigma} - \overline{\sigma}_o = D(\overline{\varepsilon} - \overline{\varepsilon}_o) - \Theta(T - T_o) + \Omega(\xi - \xi_o) \tag{5.1}$$

where $\overline{\sigma}$, $\overline{\varepsilon}$, and T are the Piolka-Kirchhoff stress, the Green strain, and the temperature. The parameters D, Θ, and Ω are material constants, and the subscript $(\cdot)_o$ corresponds to the initial conditions.

The change of the internal variable under free stress conditions is described in terms of four temperature parameters: martensite start temperature (M_s), martensite finish temperature (M_f), austenite start temperature (As), and austenite finish temperature (A_f). The behavior of the internal variable is shown in Figure 5.1. When the temperature is increasing, it is assumed that there is no change in the martensitic fraction, except during the M→A phase transition which occurs when $A_s<T<A_f$. If ξ_M is the martensitic fraction before the start of transition, the ξ-temperature relation is assumed to be of the form:

$$\xi = \frac{\xi_M}{2}\left\{\cos\left[a_A\left(T - A_s\right)\right]+1\right\} \qquad a_A = \pi / \left(A_f - A_s\right) \tag{5.2}$$

Similarly, the M←A transition is assumed to occur only when the temperature is decreasing and $M_f<T<M_s$. Assuming the martensitic fraction before the start of transition is ξ_A, then the transitions is described by:

$$\xi = \frac{1-\xi_A}{2}\cos\left[a_M\left(T - M_f\right)\right]+\frac{1+\xi_A}{2} \qquad a_M = \pi / \left(M_s - M_f\right) \tag{5.3}$$

The transitions temperatures A_s, A_f, M_f, M_s are assumed to be linearly related to the applied stress σ (Figure 5.2). With C_A and C_M denoting the slope of the lines, the relations during transition can be modified to:

$$\xi = \frac{\xi_M}{2}\left\{\cos\left[a_A\left(T - A_s - \sigma / C_A\right)\right]+1\right\} \tag{5.4}$$

$$\xi = \frac{1-\xi_A}{2}\cos\left[a_M\left(T - M_f - \sigma / C_M\right)\right]+\frac{1+\xi_A}{2} \tag{5.5}$$

As before, the relations (5.4) and (5.5) correspond to M→A and M←A transitions respectively, and only apply when the argument of the cosine is between 0 and π.

With these equations the response of the material can be computed in a piecewise manner. While the material is not undergoing a phase transition, ξ is constant and the constitutive relation (5.1) is sufficient for computing the response based on the loading conditions. The transition points can be computed based on the arguments of the cosine in equations (5.4) and (5.5). The conditions at the point of transition are then used as new initial conditions in the constitutive relation, while the appropriate relation is used to compute ξ depending on the direction of the transformation.

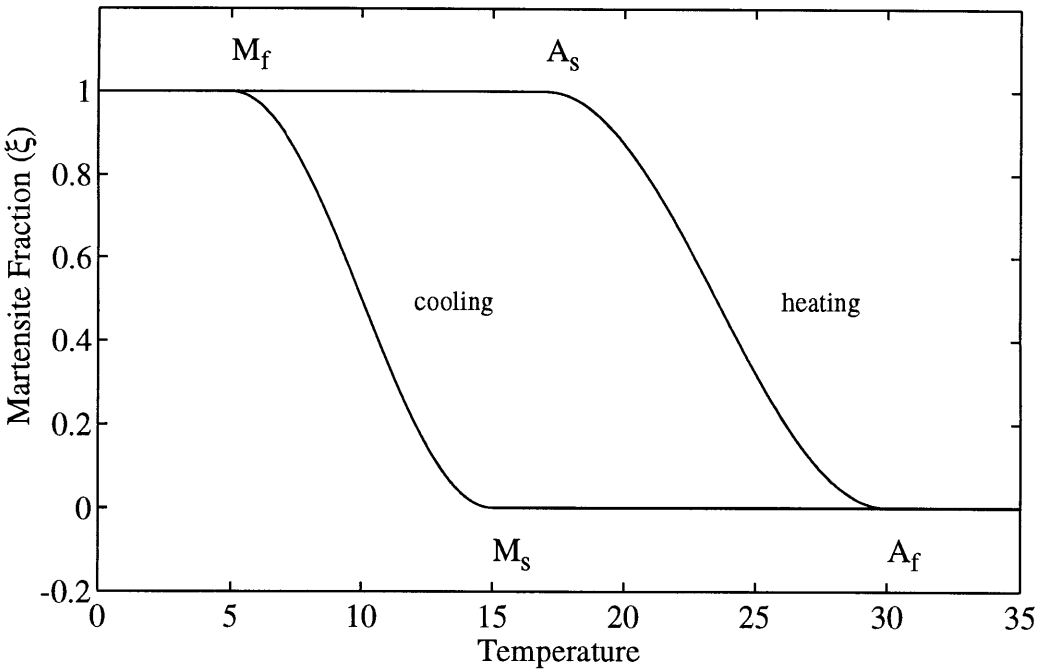

Figure 5.1 - The change in the martensite fraction as a function of temperature in terms of the parameters M_s, M_f, A_s, and A_f.

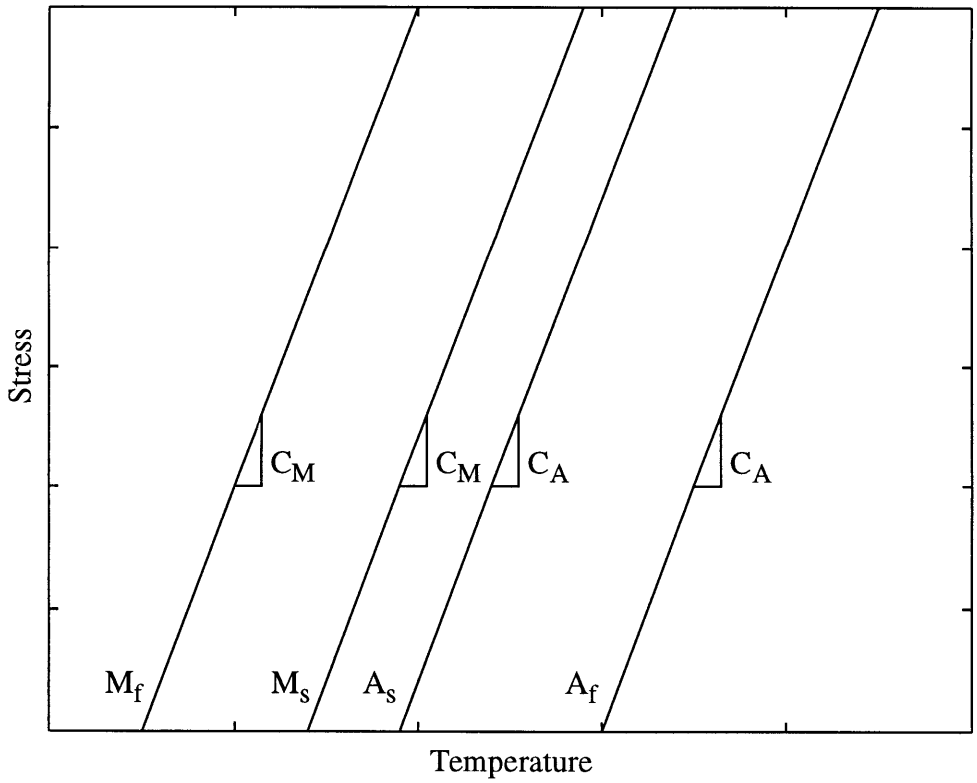

Figure 5.2 - Dependence of M_s, M_f, A_s, and A_f on applied stress.

5.1.2 Chen and Montgomery's Model for FE Poling

Another model of interest is one proposed by Chen and Montgomery [8] to describe the process of polarization reversal in a ferroelectric. The model employs an internal variable representing the degree of polarization in the ferroelectric. This internal variable (N) is incorporated into the constitutive relation involving the traditional state variables of stress (T), strain (S), and electric field (E):

$$T = cS - eNE + a|N| \tag{5.6}$$

where c, e, and a are material constants. N varies between -1 and 1. It is assumed to consist of two components:

$$N = N_p + N_r \tag{5.7}$$

where N_p denotes the dipoles which are permanently switchable, and N_r refers to dipoles which return to their original states after removal of the field. The evolution of each component, given an applied electric field is governed by a rate law. The rate law takes the form:

$$\begin{aligned}
&\frac{d}{dt}N_p = 0 && \text{if } \begin{cases} |N_p| \geq |p\beta(E)/\alpha(E)| \\ \& \\ sgn(N_p) = sgn(p\beta(E)/\alpha(E)) \end{cases} \\
&\frac{d}{dt}N_p + \alpha(E)N_p = p\beta(E) && \text{otherwise} \\
&\frac{d}{dt}N_r + \alpha_r N_r = 0 && \text{if } \begin{cases} |N_r| > |r\beta(E)/\alpha(E)| \\ \& \\ sgn(N_r) = sgn(r\beta(E)/\alpha(E)) \end{cases} \\
&\frac{d}{dt}N_r / q + \alpha(E)N_r = r\beta(E) && \text{otherwise}
\end{aligned} \tag{5.8}$$

The curve $\beta(E)/\alpha(E)$ is effectively the steady state value of N, and $\alpha(E)$ is the rate parameter. The conditions imposed on the rate law are required in order to capture the hysteretic behavior of the material. Figure 5.3 shows typical shapes for the $\beta(E)/\alpha(E)$ and $\alpha(E)$ curves. p is the fraction of dipoles which are permanently switchable while r is the fraction of dipoles which return to their original state. These parameters are therefore constrained by:

$$p + r = 1 \tag{5.9}$$

α_r, and q are constants which govern the rate of change of the non-permanent dipoles. The reader is referred to [8] for further discussion of the different parameters. $\alpha(E)$ and $\beta(E)$, as well as the various constants in the rate law, are parameters which can be adjusted to produce experimentally observed behavior.

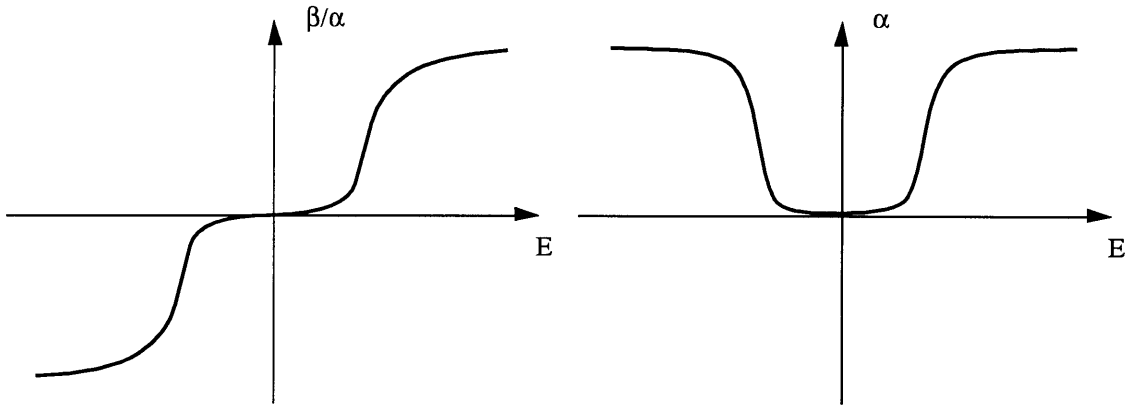

Figure 5.3 - Typical α and β/α curves used in the Chen & Montgomery model.

5.1.3 Chan model of Ferroelectrics

Another model for ferroelectric ceramics has been produced by Chan [7]. While the details of the model are too involved to be presented here, the approach is summarized. The model is based on a multiple-family system. A model for behavior of the single crystals is proposed. The crystal may be spontaneously polarized in one of the six directions parallel to the cell axes, as is the case for a perovskite in the tetragonal phase (see §2.1). Constitutive relations are proposed, describing the dependence of the strain on the polarization of the crystal and the applied field. Furthermore, upon the application of large enough external fields, the direction of spontaneous polarization may switch by either 180° or 90°. No strain is associated with a 180° transition, while 90° transitions produce a strain since the crystal lattice is elongated in the direction parallel to the polarization. Expressions for potential energy and work terms associated with transitions are derived by Chan, and the principle of minimum potential energy is used to predict switching of polarization in the crystal.

Having established the behavior of a single crystal, groups of crystals in random orientations are modeled. Each family is parametrized by three Euler angles. The behavior of each family can be predicted by transforming the external loads and electric field into the local crystal coordinates. The macroscopic response of the ceramic is then computed by

combining the response of individual crystals using one of two methods. The first is to perform direct averaging of the resulting strains and electric displacements in each family. The second is to perform a series expansion of the macroscopic properties in terms of the external loads and several parameters describing the internal alignment of the crystal polarizations. The model can be used to predict the strain, or stress produced by the crystal as well as the electric displacement. It does not however incorporate any dynamics and thus can only be used to predict quasi-static response of the material.

5.2 AFE/FE Model

Each of the models described in §5.1 have strengths and weaknesses. In this section a model for materials undergoing AFE-FE phase transition will be described. The goal is to obtain a model capable of predicting the strain produced by the material as a result of arbitrary applied electric fields under various structural stress levels.

The approach taken to model the material is described over the next few sections, starting with the desired characteristics of the model. Two internal variables are utilized, representing the fraction of the material in the FE+ and FE- states. A form for the constitutive relation similar to the one used by Chen and Montgomery is proposed. The constitutive relation makes it possible to compute external variables such as strain and stress in terms of the internal variables. The change in the internal variables is governed by a set of rate laws which depend on the applied electric field. Two types of rate laws are presented and the predictions are compared.

5.2.1 Desired Model Characteristics

Since the shape memory of the material is one of the primary characteristics of interest, it is important for the model to exhibit similar hysteretic behavior. Each of the models described in §5.1 use different approaches to produce hysteretic response. A model for shape memory ceramics based on each of these approaches could be optimized to reproduce experimental field-strain curves obtained at a specific frequency with a simple input waveform such as a triangular electric field. This however was not considered to be sufficient. Several other characteristics were also desired in the model.

The model is intended for eventual use in control system applications. It would therefore have to be a causal model, capable of producing strain outputs without prior

knowledge of the type of electric field waveform being applied. In a similar vein it should be capable of predicting correct response for fields which have an arbitrary or complicated waveform (as opposed to a simple sine wave or triangular wave). As a consequence, the model will have to be adept at dealing with partial transitions. With the type of piecewise rules used in the Rogers' model, some problems are encountered when dealing with partial transitions that are not fully reversed. Consider for example the situation depicted in Figure 5.4a. A partial martensite phase is induced by lowering the temperature. The temperature is then increased beyond the martensite start temperature and reduced again. Repeating this process, and successive application of equation (5.3) with new ξ_M values during each iteration would produce the increase in ξ shown in Figure 5.4a. A different behavior is observed in experiments with shape memory ceramics. If an electric field is applied to the PLZST material in a similar fashion, the peak strain reached in successive cycles would be no more than the peak strain achieved by applying a monotonically decreasing electric field (Figure 5.4b). Thus any internal variable used in the model would have to behave as shown in Figure 5.4b.

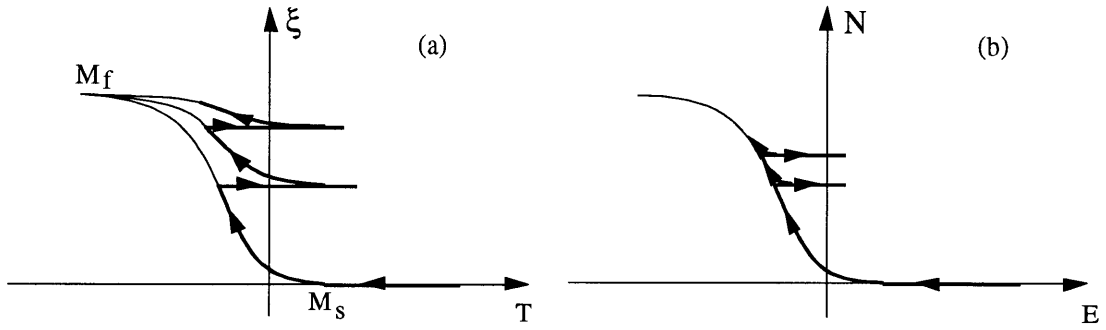

Figure 5.4 - (a) The type of behavior predicted by the Rogers' model, as temperature goes up and down. (b) The type of behavior observed experimentally in a PLZST as electric field is varied in a similar fashion.

It was also desired for the model to predict the response due to electric fields of different frequencies. This requires the existence of dynamics in the model. Chen and Montgomery's model of ferroelectrics was the only one of the three models described possessing any sort of dynamics. Figure 5.5 shows typical response of the internal variable for a cyclic electric field at different frequencies. Subplot (a) shows an intermediate frequency response. The model contains rate laws which would predict a drop in the strain level with increased frequency as seen in curve (b). This is similar to experimental response at higher frequencies. Unfortunately however, a problem exists with the response of that model at very low frequencies as seen in subplot (c). No matter

what kind of $\alpha(E)$ curve is chosen, at low enough frequencies the model response will degenerate, making the model incapable of predicting static response of the material accurately. This problem is an inherent characteristic of the model, produced by the conditions imposed on the rate law to produce hysteresis.

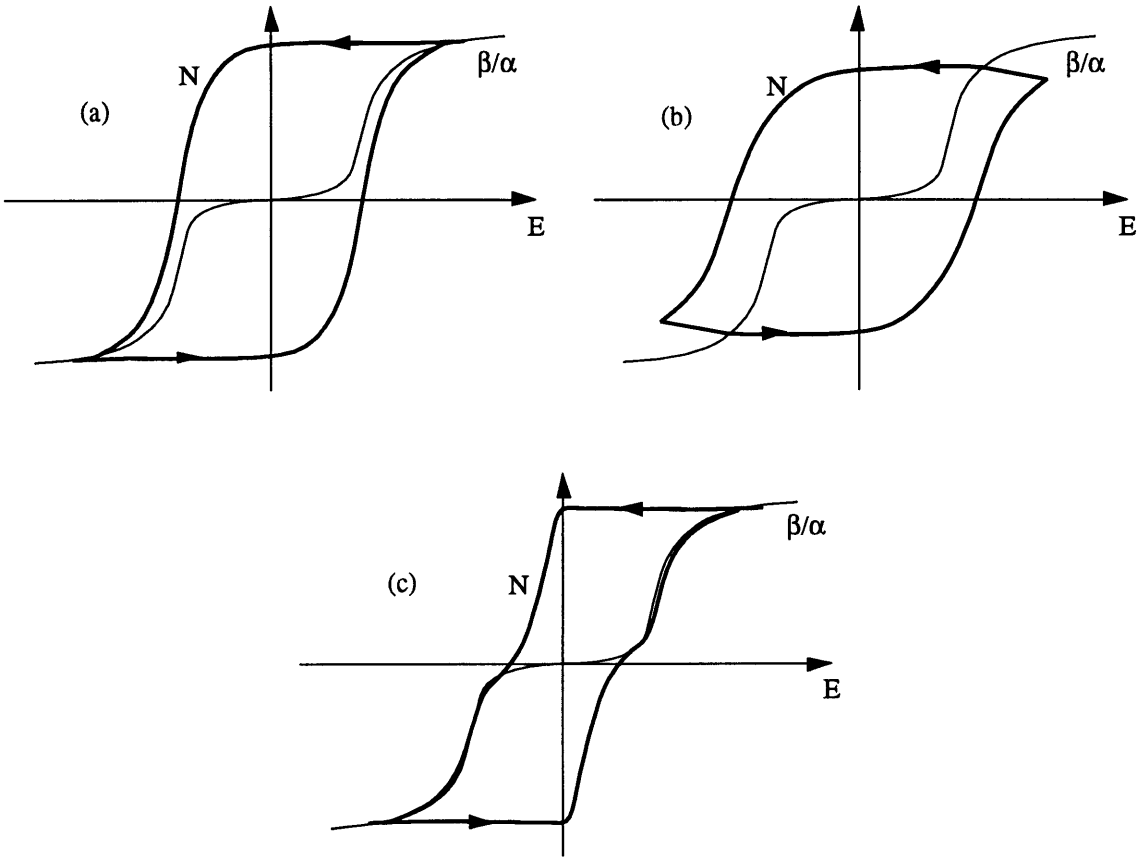

Figure 5.5 - The type of behavior predicted by the Chen and Montgomery type rate law. β/α curve is shown for reference. (a) Intermediate frequency. (b) Higher frequency. (c) Lower frequency.

The model being proposed for AFE-FE transition was formulated with an attempt to avoid similar problems. It is capable of predicting static strain response to arbitrary electric fields, and addresses the problem of partial transitions. It does not have the problem associated with the Chen & Montgomery model at low frequencies. It is however still not very successful in duplicating the frequency response observed in experiments.

5.2.2 Internal Variables and Constitutive Relation

In order to model the phase transition in antiferroelectrics, we start with an approach similar to Chen and Montgomery. The internal variable utilized by Chen and Montgomery

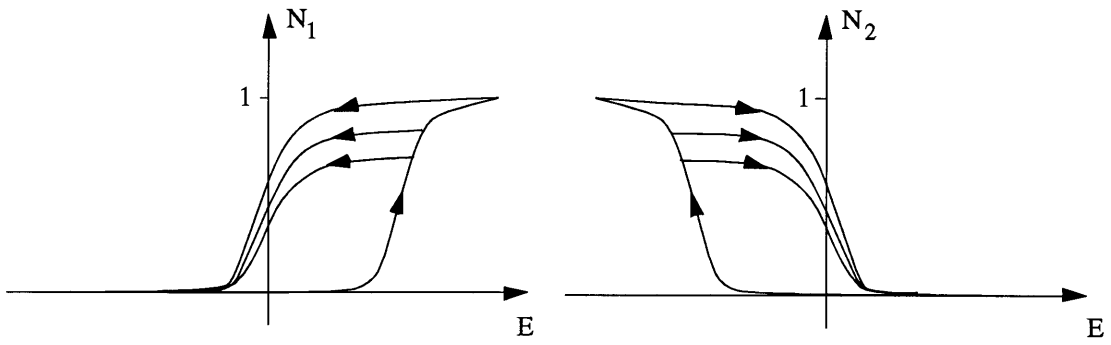

Figure 5.6 - The behavior of the internal variables given an applied electric field of different amplitudes.

represents the degree of polarization in the material, a quantity which may be positive or negative depending on the direction in which the majority of domains are polarized. A given domain in shape memory ceramics, may exist in three states. It may be in the antiferroelectric state with zero polarization, or in ferroelectric state with either positive or negative polarization. Of course, in reality a ferroelectric domain may be polarized along anyone of several axes. For the purposes of the model however, only the polarization axis most closely aligned with the direction of applied field is of importance. Two internal variables are used in the model. N_1 and N_2 represent the fraction of the material in the ferroelectric state with the polarization in the positive and negative directions respectively. Each of the variables will vary between 0 and 1 in a manner similar to figure 5.6. As it can be seen from the figure, applying sufficiently large electric field in the positive direction would cause a transition to the ferroelectric state, and thus an increase in N_1. As the electric field is reduced, N_1 decreases, reaching a remnant value at zero field. N_1 is reduced to zero only upon the application of a negative electric field. N_2 behaves in a similar manner for opposite values of electric field. Thus, the fraction of the material in the ferroelectric phase (N_{FE}), and the fraction of the material in the antiferroelectric phase (N_{AFE}) can be written in terms of the two internal variables as:

$$\begin{aligned} N_{FE} &= N_1 + N_2 \\ N_{AFE} &= 1 - N_1 - N_2 \end{aligned} \tag{5.10}$$

Obviously, the sum N_1+N_2 should remain less than or equal to one, in order for N_{AFE} to have a meaningful value. The net polarization in the material would be proportional to:

$$N = N_1 - N_2 \tag{5.11}$$

It should be noted that this is an extreme simplification of reality. In an actual sample, various crystal domains will be either ferroelectric or antiferroelectric at any given time. The net polarization of the sample depends not only on N_1 and N_2, but also on the orientation of each of the FE domains. Proceeding with the simplified view of the material, the constitutive relation used by Chen and Montgomery can then be used with a slight modification:

$$T = cS - eNE + aN_{FE} \tag{5.12}$$

T is the transverse stress on the sample, S is the transverse strain, and E is the electric field applied across the sample. Since N_{FE} is defined to represent the fraction of FE in the material, the quantity aN_{FE} describes the stress due to phase transition from AFE to FE in a constrained sample. This term replaces the $a|N|$ term in (5.6), which represents the stress due to polarization reversal in the Chen and Montgomery model. The quantity eNE describes the stress produced by the piezoelectric effect in the ferroelectric portion of the material. Ideally, equation (5.12) would be replaced with a tensor equation describing the relation between the stress and strain vectors in voigt notation, the electric field vector, and the internal variables. The constant parameters would then be replaced with matrices. However, since the experimental data obtained for the material is limited, it would not be possible to estimate all elements of those matrices. The present model is thus limited to transverse stress/strain. If there is no stress on the sample, the strain can be calculated from (5.12) as

$$S = (eNE - aN_{FE}) / c \tag{5.13}$$

To complete the model, we still need to determine the equations governing the change in the internal variables. Several approaches were taken, all the while concentrating on achieving a model which would behave in a manner similar to the material given a wide variety of applied electric waveforms. The following subsections present two of these approaches and compare the results obtained with them. The first is similar to the rate laws in the Chen and Montgomery model and is presented primarily for comparison purposes. The second is based on a multiple family approach inspired by, but quite different from Chan's model of piezoceramics.

5.2.3 Chen and Montgomery Based Rate Law

Early versions of the model followed a scheme similar to that used by Chen and Montgomery for modeling ferroelectrics. Each of the internal variables, N_1 and N_2, follow a rate law as in that model but with modified $\alpha(E)$ and $\beta(E)$ functions. The functions used to determine the evolution of N_1 are offset with respect to zero field as shown in Figure 5.7. The mirror image of the functions, i.e. $\alpha(-E)$ and $\beta(-E)$, are used to govern the evolution of N_2. As before, the internal variables are broken up into permanently switchable and non-permanently switchable components:

$$N_i' = N_{i,p}' + N_{i,r}' \tag{5.14}$$

where $(\cdot)'$ is used to identify internal variables generated by the Chen and Montgomery rate law which vary between -1 and 1. It is necessary to scale these variables such that they vary between 0 and 1 before using them in the constitutive relations for shape memory ceramics proposed in §5.2.2. This is accomplished using:

$$N_i = \tfrac{1}{2}\left(1 + N_i'\right) \tag{5.15}$$

The evolution of the of the internal variables are governed by the following rate law:

$$\begin{aligned}
&\tfrac{d}{dt}N_{i,p}' = 0 && \text{if} \begin{cases} |N_{i,p}'| \geq |p\beta_i(E)/\alpha_i(E)| \\ \& \\ sgn(N_{i,p}') = sgn(p\beta_i(E)/\alpha_i(E)) \end{cases} \\
&\tfrac{d}{dt}N_{i,p}' + \alpha_i(E)N_{i,p}' = p\beta_i(E) && \text{otherwise} \\
&\tfrac{d}{dt}N_{i,r}' + \alpha_r N_{i,r}' = 0 && \text{if} \begin{cases} |N_{i,r}'| > |r\beta_i(E)/\alpha_i(E)| \\ \& \\ sgn(N_{i,r}') = sgn(r\beta_i(E)/\alpha_i(E)) \end{cases} \\
&\tfrac{d}{dt}N_{i,r}'/q + \alpha_i(E)N_{i,r}' = r\beta_i(E) && \text{otherwise}
\end{aligned} \tag{5.16}$$

Figure 5.8 shows an example of the result produced by the model compared to the transverse strain of the A3 sample. A triangular electric field waveform with an amplitude of 2.7 kV/mm and frequency of 0.01 Hz is used. The value of c was determined from the stress tests as discussed earlier, and other parameters were adjusted manually to reproduce experimental strain. The $\alpha_i(E)$ and $\beta_i(E)$ used are shown in Figure 5.7. Results were improved by choosing $\alpha_i(E)$ such that the forward transitions were faster than the reverse transitions. The other parameters used are listed in Table 5.1.

Table 5.1 - Parameters used in for the model with Chen/Montgomery based rate law.

α_r=0.02 s^{-1}	q=0.15	p=0.9	r=1-p
c=116×10^9 Pa	e=-2.70 Pa m/V	a=72×10^6 Pa	

Given a single experimental field-strain curve, it is possible to achieve a fairly good match with the model in this way. However the model is quite sensitive to the rate parameters. Thus, modeling the frequency dependence of the strain response was found to be very difficult. Specifically, the model parameters can be adjusted to yield a strain curve which matches experimental results for a given electric field amplitude and frequency. However, changing the frequency of the electric field in the model sometimes resulted in unexpected results. This can be seen in Figure 5.9 which shows the response of the same model at 0.001 Hz.

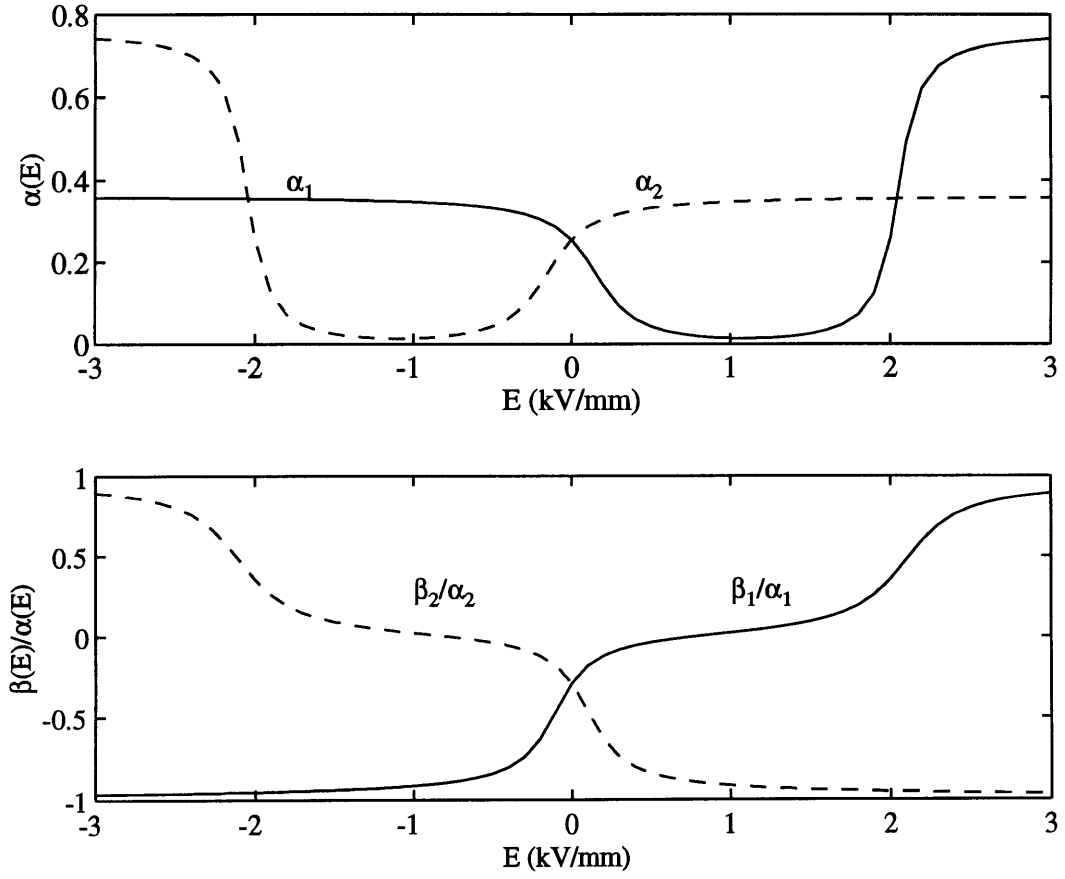

Figure 5.7 - $\alpha_i(E)$ and $\beta_i(E)/\alpha_i(E)$ curves used in modeling phase transition.

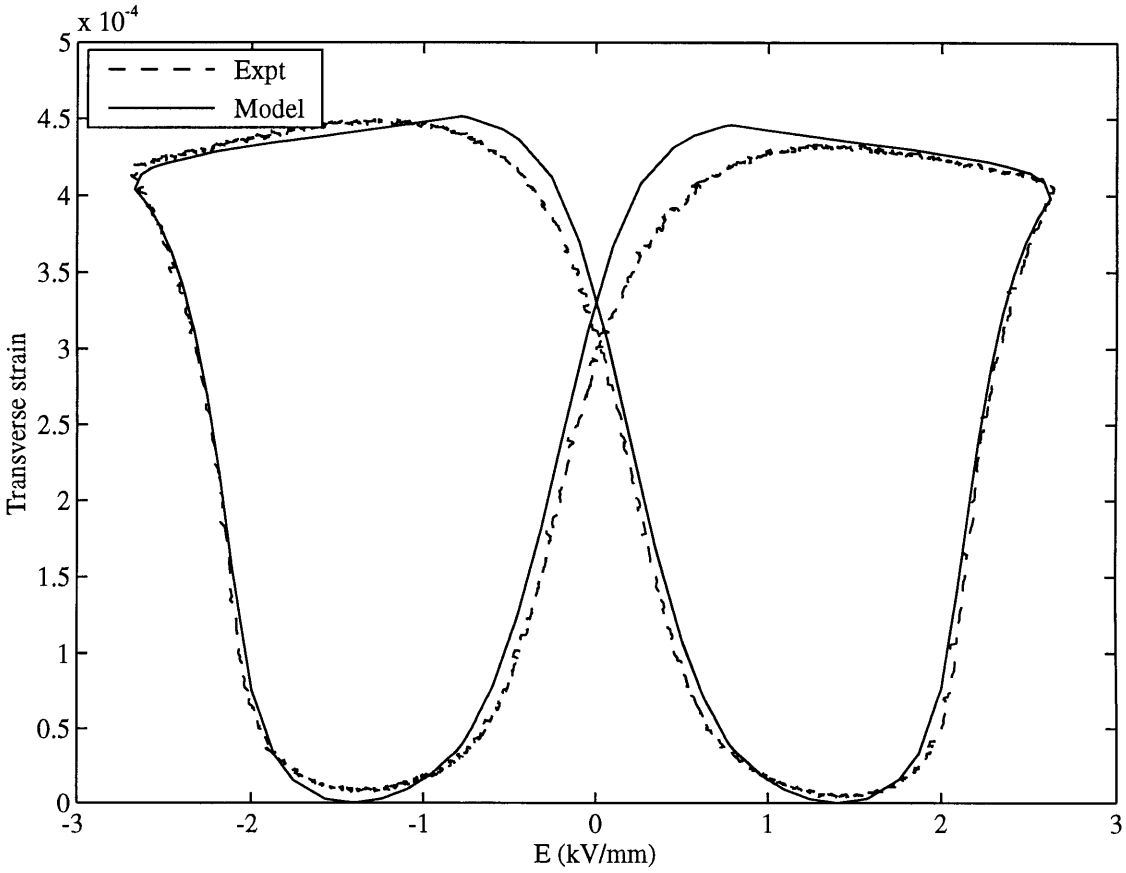

Figure 5.8 - Example of the transverse strain generated by the model compared to experimentally measured strain in an A3 sample (Using equations 5.10-5.16 and the parameters listed in Table 5.1).

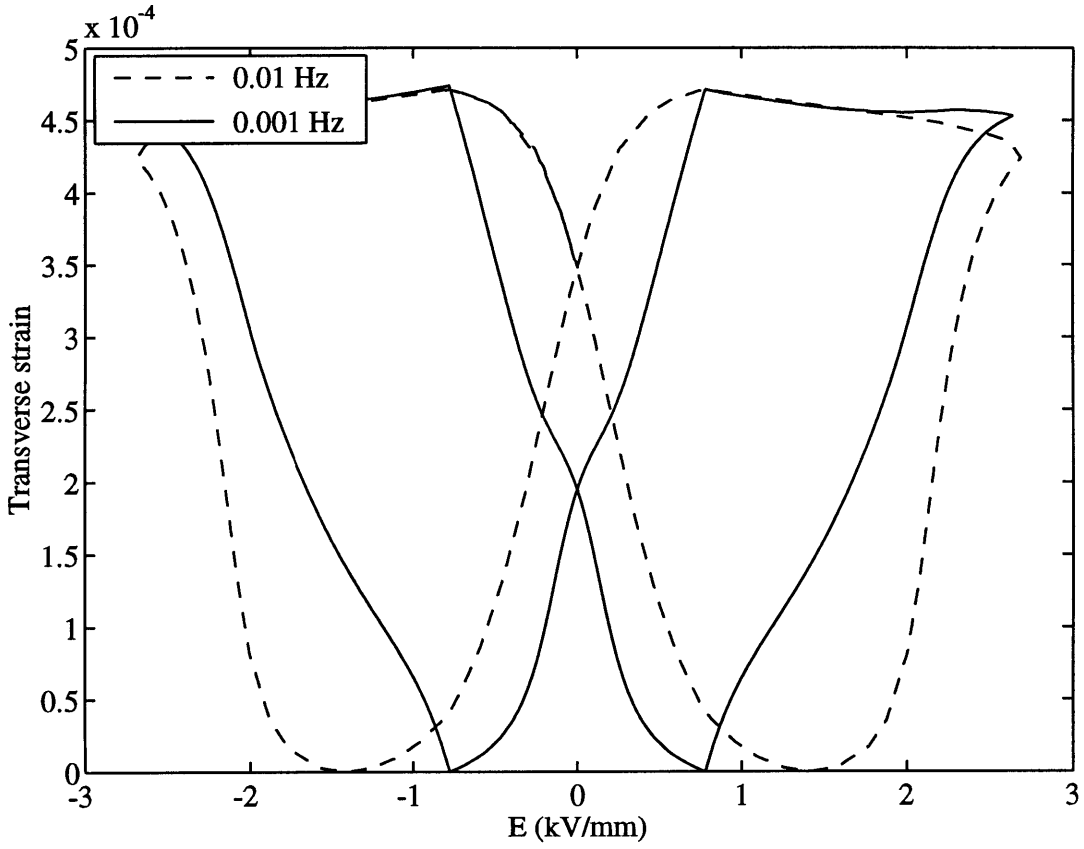

Figure 5.9 - Transverse strain generated by the Chen/Montgomery based model in response to an electric field with a frequency 1/10 of the design frequency (Using equations 5.10-5.16 and the parameters listed in Table 5.1).

5.2.4 Multiple Family Based Rate Law

The rate law presented in the previous section, aside from having difficulty at low frequency, also has difficulty with modeling partial transitions. The model performs fairly well if the applied electric field has a large enough amplitude to cause a transition in the entire material. However, if only partial transition is induced, problems similar to those shown in Figure 5.4a are encountered. Similar difficulties were encountered with all rate laws which attempted to model the material with only two internal variables. In order for the model to be capable of dealing with arbitrary waveforms, more information about the internal state of the material is required.

A possible solution can be seen by reconsidering the physical system. A sample of the ceramic contains numerous domains, which due to their orientation, state of surrounding material, and compositional variations, undergo transitions at slightly different field levels. It becomes clear that when using only a small number of internal variables, sufficient information about the internal state is not available.

While the physical system is much too complicated to model fully, the concept of multiple domains can be used. While this is inspired by the Chan model (§5.1.3), a much less rigorous approach is taken, with more emphasis on replicating experimental results than on modeling the crystal behavior in detail. An isolated domain could be described in terms of two parameters: E_f, the forward coercive field, and E_r, the reverse coercive field. The state of the domain at any given time depends on the value of the electric field relative to E_f and E_r, and the previous state of the domain:

$$\begin{array}{ccc} E_f < E & \Rightarrow & AFE \rightarrow FE+ \\ E < E_r \;\&\; E < E_f & \Rightarrow & FE+ \rightarrow AFE \\ E < -E_f & \Rightarrow & AFE \rightarrow FE- \\ -E_r < E \;\&\; -E_f < E & \Rightarrow & FE- \rightarrow AFE \\ otherwise & \Rightarrow & unchanged \end{array} \qquad (5.17)$$

It is assumed that E_f>0. Also, it can be seen that if E_r>0 the domain does not possess shape memory, and will return to the AFE state as soon as E becomes less than E_r. All domains having specific values of E_f and E_r will be referred to as a "family". At any given time, the domains in a family may be in the antiferroelectric state, positive ferroelectric state, or negative ferroelectric state. We can define n_1 as the fraction of the

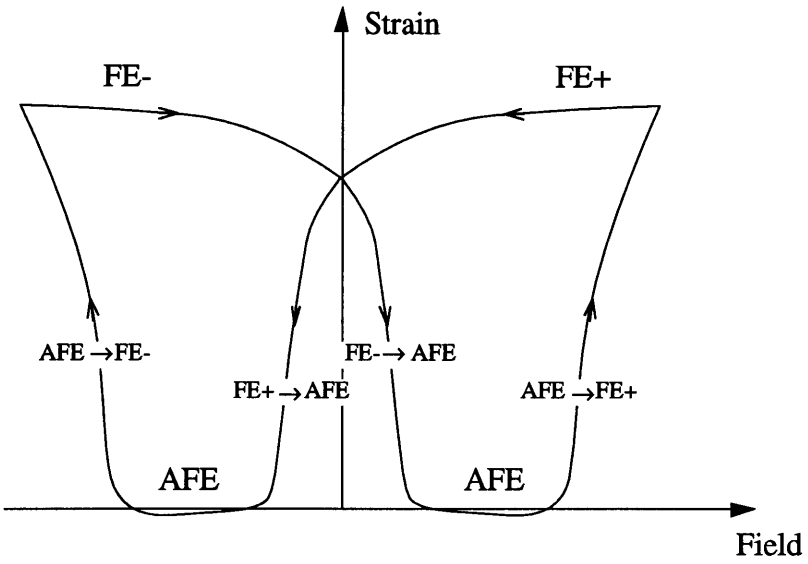

Figure 5.10 - The four possible transitions in a shape memory ceramic material.

family in the FE+ state, and n_2 as the fraction of the family in the FE- state. n_1 and n_2 can vary between 0 and 1.

A rate law is needed to describe each of the four possible transitions. It is assumed that the rate of a transition is proportional to the population of the initial state. Also different forward and reverse transition rates are permitted. The governing equations can thus be written as:

$$\begin{array}{ccc} E_f < E & \Rightarrow & \dot{n}_1 = \alpha_f(1-n_1-n_2) \\ E < E_r \;\&\; E < E_f & \Rightarrow & \dot{n}_1 = -\alpha_r n_1 \\ E < -E_f & \Rightarrow & \dot{n}_2 = \alpha_f(1-n_1-n_2) \\ -E_r < E \;\&\; -E_f < E & \Rightarrow & \dot{n}_2 = -\alpha_r n_2 \end{array} \tag{5.18}$$

Wherever not otherwise specified, the rates of change of n_1 and n_2 are assumed to be zero. α_f is the rate parameter for the forward transition and α_r is the rate parameter for the reverse transition. Note that with the above rate laws, we are ensured to satisfy the constraint on the sum of n_1 and n_2 being less than one, so long as the initial conditions also satisfy that constraint:

$$n_1 + n_2 \leq 1 \tag{5.19}$$

The exact values of E_f and E_r depend on several factors. Assuming constant temperature, one of the primary factors is the orientation of the lattice relative to the

direction of the applied field. If the forward coercive field for a domain whose polarization axis is aligned with the applied field is E_f^o, the coercive field for a domain rotated through angle θ would be:

$$E_f = E_f^o / \cos\theta \tag{5.20}$$

Since the domain is embedded in the ceramic, it is also affected by the surrounding material. Depending on the state the surrounding material is in, the domain of interest will be experiencing stresses which could inhibit or encourage the transition. Even more significant would be slight variations in the composition of the ceramic. In a PLZST sample, the cube center site may be occupied by either Pb^{2+} or La^{3+}, and the cube corner site may be occupied by Zr^{4+}, Sn^{4+}, or Ti^{4+}. Different domains will have slightly different distributions of cations, and will therefore undergo phase transitions at different field levels. These effects combine to produce a distribution of domains with different E_f and E_r. We shall define the population density function describing the distribution of these domains as:

$$\mathrm{f}(E_f, E_r) \qquad E_f > 0 \tag{5.21}$$

Thus $\mathrm{f}(E_f, E_r)dE_f dE_r$ is the fraction of the material which undergoes an AFE$\rightarrow$FE transition when $E_f < E < E_f + dE_f$ and which undergoes an AFE$\leftarrow$FE transition when $E_r < E < E_r + dE_r$, and so on. As with any population density function, $\mathrm{f}(\cdot)$ must satisfy a normalization condition:

$$\int_0^\infty dE_f \int_{-\infty}^\infty dE_r \; \mathrm{f}(E_f, E_r) = 1 \tag{5.22}$$

As already mentioned, the exact distribution of E_f and E_r, and thus the form of $\mathrm{f}(\cdot)$, depends on many factors which are difficult to model. Therefore, for lack of a better model, it is assumed that E_f and E_r have independent normal distributions with means and standard deviations of E_f^m, E_f^s, E_r^m, and E_r^s. Results using this assumption will be present in the following section. The cumulative probability density for a normal random variable with mean m, and standard deviation s is given by

$$\mathrm{Prob}_{norm}(X < x) = \mathrm{P}\left(\frac{x-m}{\sqrt{2}s}\right) = 1 + \tfrac{1}{2}\mathrm{erf}\left(\frac{x-m}{\sqrt{2}s}\right), \tag{5.23}$$

where the erf() function is the standard error function. The cumulative probability density for E_f and E_r was chosen to be:

$$\mathrm{F}(E_f, E_r) = \mathrm{P}\left(\frac{E_f - E_f^m}{\sqrt{2}E_f^s}\right)\mathrm{P}\left(\frac{E_r - E_r^m}{\sqrt{2}E_r^s}\right) \tag{5.24}$$

Different internal variables n_1 and n_2 exist for each family, parametrized by E_f and E_r. To obtain the total fraction of the material in a given state, we need to integrate over all families:

$$\begin{aligned} N_1 &= \int_0^\infty dE_f \int_{-\infty}^\infty dE_r \; \mathrm{f}(E_f, E_r) n_1(E_f, E_r) \\ N_2 &= \int_0^\infty dE_f \int_{-\infty}^\infty dE_r \; \mathrm{f}(E_f, E_r) n_2(E_f, E_r) \end{aligned} \tag{5.25}$$

Given an applied electric field, the evolution of the internal variables n_1 and n_2 can be computed according to (5.18). N_1 and N_2 are then obtained from (5.25) and used to calculated the strain in the material from (5.13). To implement the model, the continuous distribution of families is discretized. The listing of the MATLAB code for the model as well as some numerical implementation issues are presented in Appendix C.

5.3 Model Results

The model described in the previous section is governed by 9 parameters: E_f^m, E_f^s, E_r^m, E_r^s, α_f, α_r, e, a, and c. Under free strain conditions, it is only the ratios e/c and a/c which are of importance. Since it would be impossible to determine c using free strain data, the value of stiffness obtained in §4.4 was used. At low excitation frequencies the model response is independent of the value of the rate parameters (α_f and α_r). The values of all other parameters were obtained through an optimization process. A cost function was defined based on the pointwise error between the strain produced by the model and the strain observed experimentally:

$$J = \frac{1}{\#points}\sum (S_{expt} - S_{model})^2 \tag{5.26}$$

It should be noted that the dependence of strain on e and a is linear. Thus, once the rate equations are integrated for given values of E_f^m, E_f^s, E_r^m, E_r^s, α_f, and α_r, and N_1

and N_2 are obtained, the optimum e and a can be solved for explicitly. The other model parameters were adjusted using a standard gradient search algorithm in MATLAB, while at each step of the nonlinear optimization, e and a were calculated using the standard least squares minimization technique.

Figure 5.11 shows the experimental strain-field curve for the A3 sample at 0.01 Hz. This data was used in the optimization to produce the static response of the model. Arbitrarily large values were selected for the rate parameters (α_f and α_r) and were fixed during the optimization. The parameter values obtained with this optimization are listed in Table 5.2.

Table 5.2 - Parameters used in for the model with multiple family based rate law. Values are optimized for response at 0.01 Hz.

$E_f^m = 2.24\times10^6$ V / m,	$E_r^m = -1.64\times10^5$ V / m
$E_f^s = 2.53\times10^5$ V / m,	$E_r^s = 3.98\times10^5$ V / m
$\alpha_f = 100$ s^{-1},	$\alpha_r = 500$ s^{-1}
$e = -1.05$ Pa m / V,	$a = 53.9$ MPa
$c = 116$ GPa	

Figure 5.11 also shows the output of the model using the above parameters. It can be seen that the model is capable of reproducing the general shape of the field-strain curve fairly well. The slight remaining discrepancy can be attributed to the rather arbitrary choice of using normal distributions in modeling the population density of various families. Better fits may be obtained by using more general functions to describe the distribution. This however, would also entail fitting more parameters.

In order to optimize the response of the model over a range of frequencies, several experimental field-strain curves obtained at different frequencies were utilized in the optimization. For each set of data, the corresponding strains were calculated using the model. Also, a new cost function was defined:

$$J = \sum_{\text{diff freq}} \left\{ \frac{1}{\#points} \sum (S_{expt} - S_{model})^2 \right\} \tag{5.27}$$

The optimization was performed in two stages, in hopes of speeding up convergence. The goal of the first stage was to fit the static response of the model to experimental results while in the second stage frequency effects were included. Only one set of data was used during the first stage, simplifying the evaluation of the cost function. The rate parameters were fixed at fairly high values and only the parameters governing the distribution of the families were allowed to change. In the second stage, data at multiple frequencies were used, and the rate parameters (α_f and α_r) were also included in the optimization.

Figure 5.12 shows the experimental strain-field curves from §4.5. The data obtained at 0.02 Hz was used in the first stage of optimization, and all the data were used in the second stage. The parameter values obtained with this optimization are listed in Table 5.3.

Table 5.3 - Parameters used in for the model with multiple family based rate law. Values are optimized for response over the frequencies 0.02-20 Hz.

$E_f^m = 2.76\times10^6$ V / m,	$E_r^m = -9.97\times10^4$ V / m
$E_f^s = 6.11\times10^5$ V / m,	$E_r^s = 5.90\times10^5$ V / m
$\alpha_f = 333$ s^{-1},	$\alpha_r = 562$ s^{-1}
$e = -0.410$ Pa m / V,	$a = 44.4$ MPa
$c = 116$ GPa	

The model predictions are superimposed on corresponding experimental data in Figure 5.12. Reasonable qualitative agreement is observed between the experimental field-strain curves and the model predictions. As expected from experiments, the strains predicted by the model are smoother and have lower amplitude at higher frequencies. Figure 5.13 compares the peak-to-peak strains produced at each frequency. To improve the match between the frequency response of the model and experimental data, more complicated rate laws would be required.

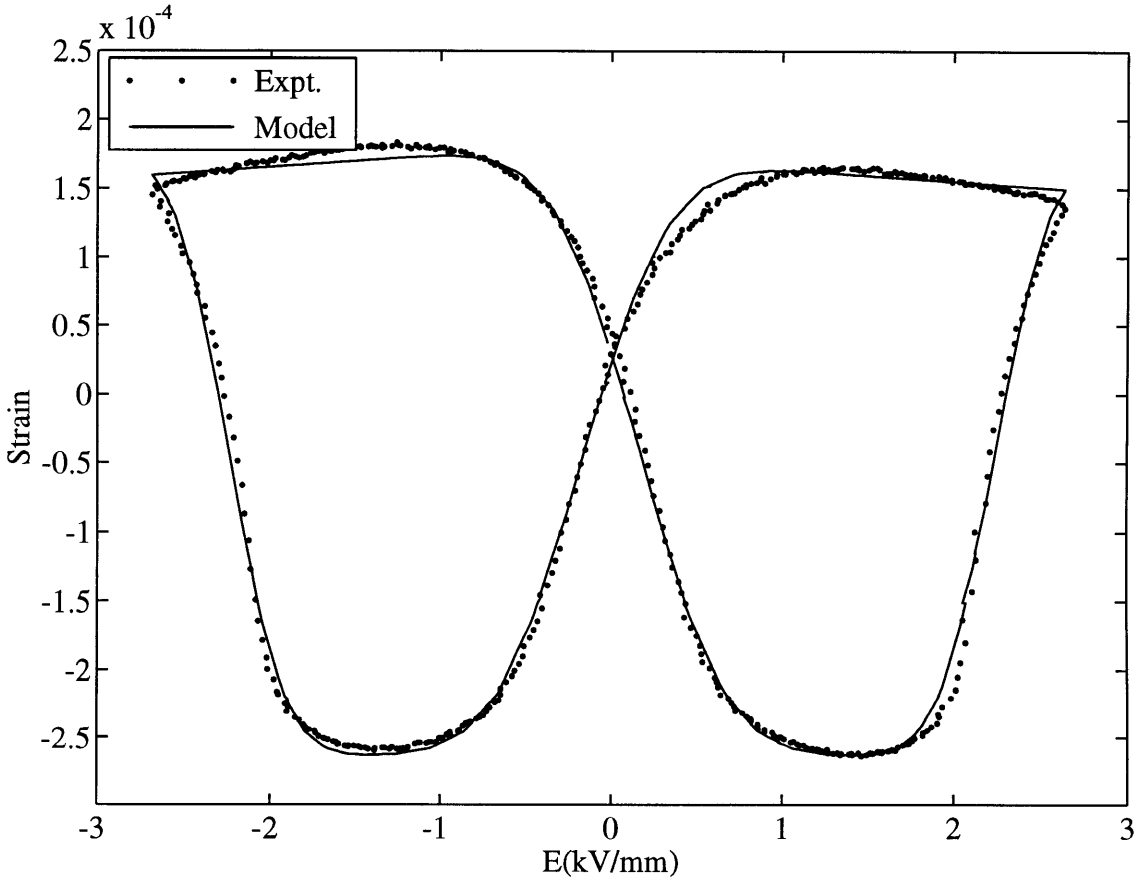

Figure 5.11 - Comparison of experimental field-strain curve with the multiple family model prediction. The parameter values in Table 5.2 were used for the model.

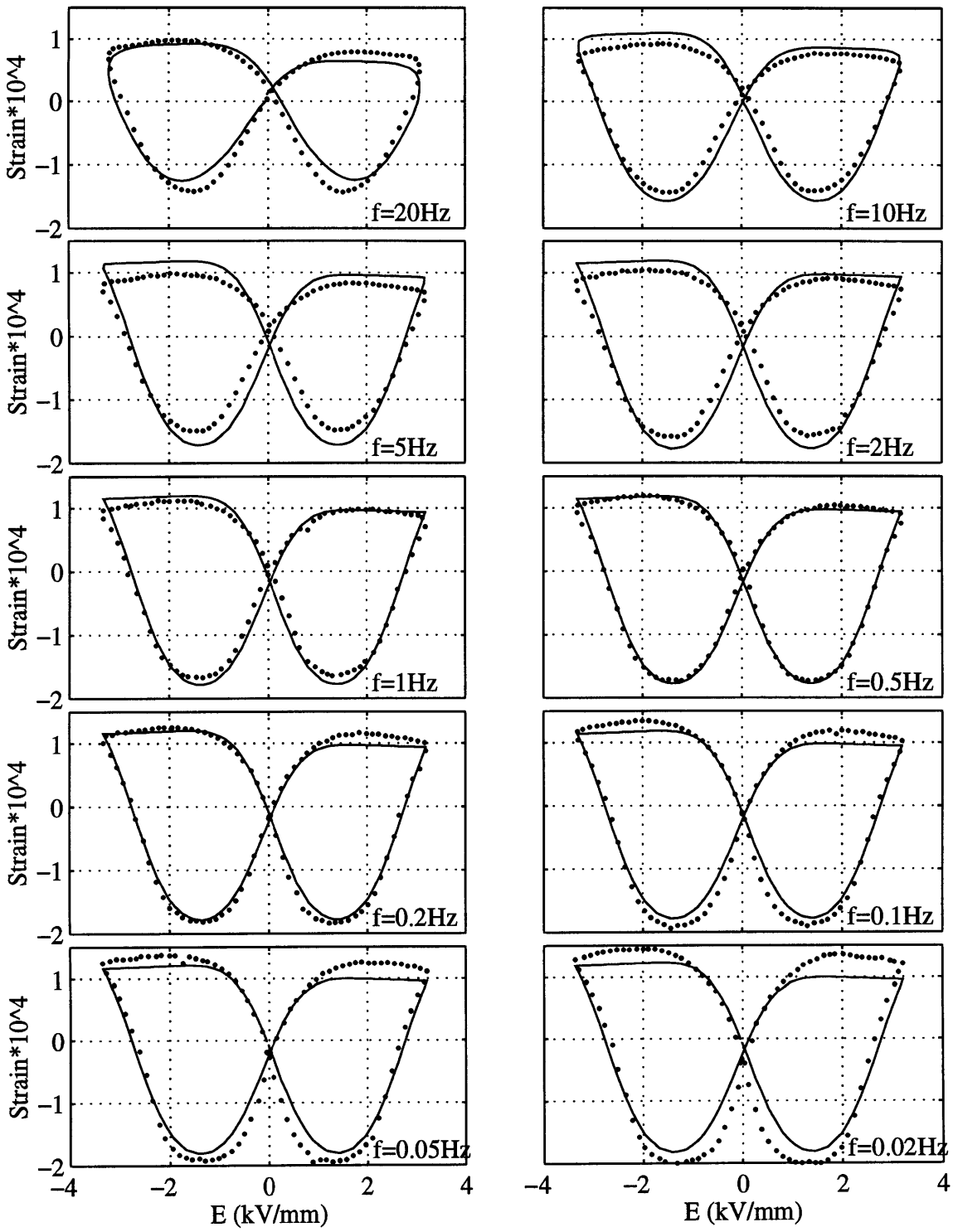

Figure 5.12 - Comparison of experimental field-strain curves (dots) obtained at different frequencies with the multiple family model predictions (solid). The parameter values in Table 5.3 were used for the model.

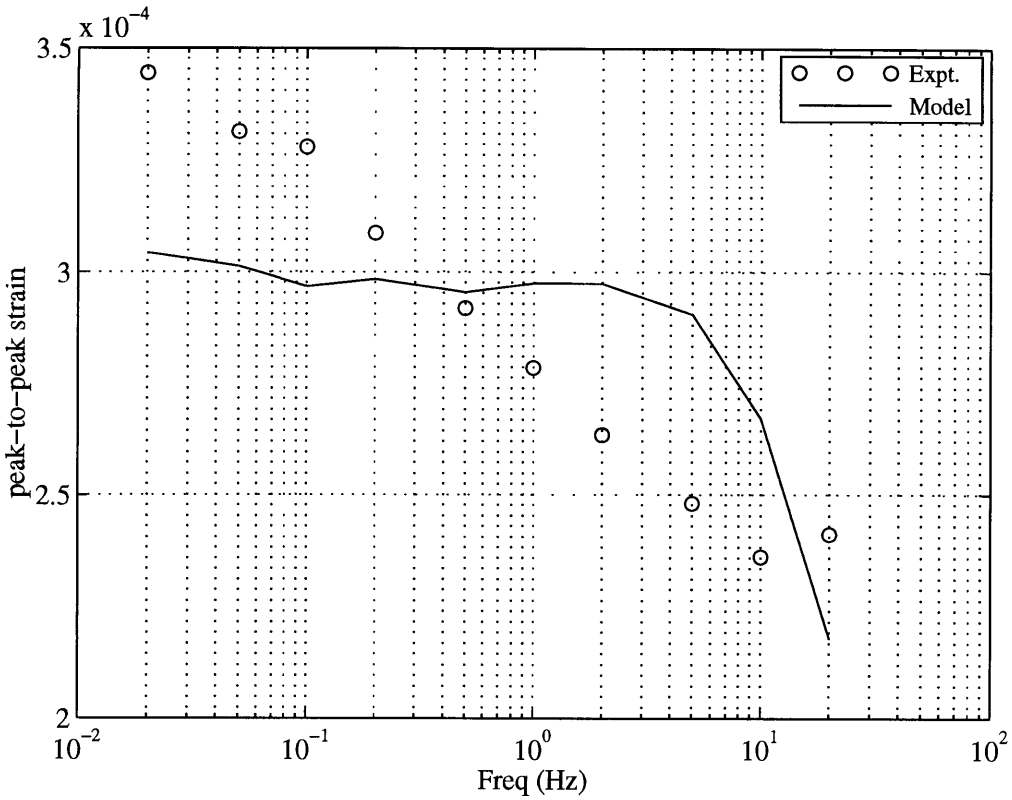

Figure 5.13 - Comparison of experimental and model peak-to-peak strain levels from Figure 5.12 as a function of frequency.

5.4 Summary

A phenomenological approach has been employed in modeling the behavior of shape memory ceramics. Three approaches from the literature for modeling phase transitions were summarized. Rogers utilizes a single internal variable representing the martensitic fraction to model the static response of shape memory alloys. A piecewise expression relating the martensitic fraction to temperature was used to predict the change of the internal variable. Similarly, Chen and Montgomery's model of polarization reversal in ferroelectrics utilizes an internal variable representing the net polarization of the material. The evolution of that internal variable is governed by a rate law. Chan argues that a single internal variable is not sufficient to predict the response of a ferroelectric to arbitrary electric fields. He has proposed a model utilizing multiple internal variables representing the state of different domains within the ceramic.

To model shape memory ceramics with AFE-FE phase transition, two basic internal variables are utilized representing the fraction of the material in each of the FE+ and FE-

states. A constitutive relation is proposed relating these internal variables to the applied electric field, external stress, and the strain of the material. Two approaches for modeling the evolution of the internal variable have been presented. In the first approach, each variable follows a set of rate laws similar to the Chen and Montgomery rate law. This approach was found to produce models with undesirable frequency characteristics. The model also could not represent partial transitions in a satisfactory manner. In the second approach, the ceramic is considered to consist of multiple families of domains with a distribution of properties. Two internal variables are used to represent the state of each family, and follow a set of proposed rate laws. These variables are summed over all the families to obtain the two internal variables for the entire material. This multiple family model is capable of producing correct response in the case of partial transitions. Also, it does not suffer from the low frequency problems associated with the former approach.

The proposed multiple family model is quite successful at duplicating experimental field strain curves at a specific frequency. While it is also capable of producing correct trends in the frequency response, there is room for improvement. Several approaches may be able to address this problem. It may be possible to improve the response by replacing the constant rate parameters α_f and α_r by functions of E_f and E_r. Or, one may need to replace the linear rate laws with other nonlinear rate laws. An even more ambitious approach may be needed.

Another aspect of the model which may be improved is the *ad hoc* approach taken in determining the distribution of the families with different values of E_f and E_r. Several attempts were made to model the distributions based on the polycrystalline structure of the ceramic, and the random distribution of the orientation of the different domains. However, due to the complexity of such a problem, only simple models could be constructed which were incapable of producing a viable distribution function.

6 ADAPTIVE MIRROR DEVELOPMENT

Design of an adapt as defined by sample application of shape memory ceramics. The following section will present the motivations for such an application. Two prototype mirrors were constructed and experimental results from them are discussed in the §6.2. In §6.3 finite element and Rayleigh-Ritz models are presented which were used to investigate some design considerations for full scale adaptive mirrors with large numbers of actuators.

6.1 Space Based Adaptive Optics

Space based telescopes have been increasing our understanding of the universe by providing astronomical images which are not distorted by the earth's atmosphere. The use of adaptive optics would be a great means of further increasing the capabilities of this technology. The main driving factor in the performance of such precise optical instruments is the presence of figure errors in the optics. In order to obtain diffraction limited images, the figure errors must be much smaller than the wavelength of interest. Grinding the optical components to such precision is difficult and expensive, especially for the primary mirror of a telescope which is the largest component of the system. For example, the Hubble Space Telescope (even without the spherical aberration in its primary mirror) would still not be able to obtain diffraction limited images in the far ultraviolet, because the figure errors present are of the same order as the wavelength for ultraviolet light [29]. Furthermore, to ensure the primary mirror will maintain the proper shape despite changes in the gravitational loading, it needs to be made quite stiff by increasing its thickness, and thus its weight. Using adaptive optics, one could compensate for figure errors, and thus obtain diffraction limited images at lower wavelengths. Also, if the secondary mirror of a telescope was capable of actively compensating for errors in the primary, the stiffness and

precision requirements on the primary could be relaxed, thus reducing its weight and the cost of future space observatories.

Another use of adaptive optics in space would be in the area of high bandwidth imaging. To obtain images of faint objects that are located close to a bright object, such as a planet orbiting a star. Such direct observation is not possible since the diffraction sidelobes from the star would swamp the image of the faint planet. It is possible to reduce the diffracted light using a cornograph or rotational shearing interferometer. The results would be limited by scattered light due to the figure errors. An adaptive secondary can compensate for those figure errors to reduce the scattered light and thus improve the results of cornographic imaging techniques. An even more sophisticated approach is the use of adaptive mirrors to implement 'dark hole' algorithms. Rather than attempting to reduce the scattered light uniformly over the field of view, such algorithms reduce the scattered light by an additional factor of ~100 to ~1000 only in the specific region near the center of the field of view. The mirror would actively redistribute the scattered light away from the area where the faint object is being observed [29].

It is necessary to point out the distinction between the above applications and the use of adaptive optics to correct for atmospheric disturbance. While the two are inherently similar, they are driven by different requirements. A ground based application is driven by the distortions of the wavefront caused by the atmosphere. Thus the system must have an update rate which can compensate for the bandwidth of the atmospheric (~100 Hz). On the other hand, a space based observatory is in a very stable environment, and the problem becomes one of shape control, with updates as infrequent as once every few minutes or hours. Furthermore, correcting for the wavefront error produced by the atmosphere requires actuators with fairly large stroke (10 μm). The space based application, however, would only require actuators with stroke levels which are a fraction of the wavelengths of interest. A stroke of 50 nm would be sufficient to meet such requirements. This makes it possible to use a monolithic actuator rather than electroceramic stacks to meet the stroke requirement [29].

The primary mirror, due to its large size, is the most difficult to manufacture, and will have the highest number of imperfections in the system. The number of actuators used in the adaptive mirror would determine the size of the figure errors in the primary which could be compensated for. If there are n actuators across the diameter of the secondary, and the primary has a one meter diameter, the smallest area over which figure errors could

be compensated for is 1/n meters. Thus by increasing the number of actuators figure errors with higher spatial frequency can be compensated for [29].

Using a large number of actuators in such an application is made much simpler by the shape memory and nonlinear material response of the PLZST ceramics. An array of electroceramics bonded to the rear surface of the mirror may be used to correct deformations in the mirror (Figure 6.1). While a great deal of work has been done in adaptive optics, our goal is to demonstrate the benefits of using shape memory ceramics in such applications. There are several advantages associated with utilizing the strain associated with phase transition. The first is the large actuation capability obtained from the high strain levels. The second is the residual strain at zero field. Rather than using a large array of amplifiers to power each actuator individually, a single amplifier can be used to program the actuators sequentially. This simplifies the requirements on the power supply and the driving circuitry. One may be concerned about the large temperature dependence of the material response. However, a scientific instrument such as a space telescope is generally equipped with a temperature control system to prevent thermal deformation of the optics. Hence the actuators can be tailored to have their peak performance at the operating temperature of the instrument.

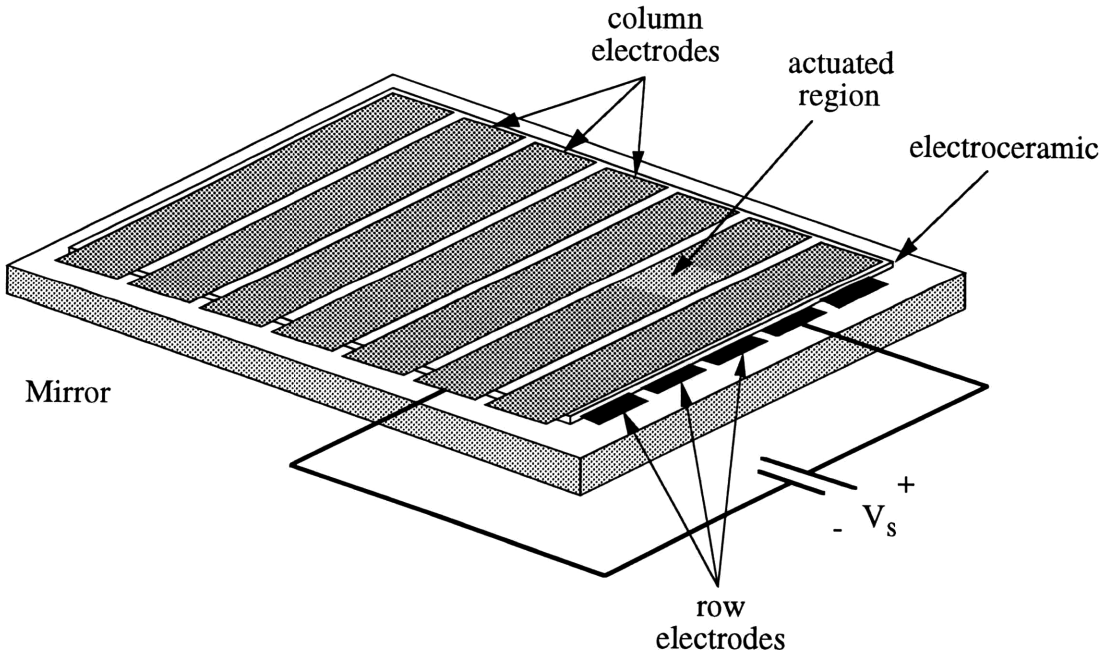

Figure 6.1 - Schematic of adaptive mirror with an array of actuators addressed by row/column electrodes.

An even greater advantage can be gained by utilizing the nonlinearity of the antiferroelectric actuators in future applications. Due to the nonlinearity, a deadband exists in the material response. With the material in its antiferroelectric phase, no response is observed until the electric field exceeds the minimum required for switching. This suggests the use of a row/column addressing technique for large arrays of actuators. Figure 6.2a shows a segment of an adaptive mirror with a large array of actuators. Columns of actuators share the top electrode, while rows of actuators share the bottom electrodes. To activate a specific actuator, the voltage on the corresponding row and column electrodes can be set to slightly larger than +V and -V volts respectively, while the remaining electrodes are grounded. The actuator at the intersection will experience a large enough field to undergo phase transition. Other actuators on the same row and column however, will only experience half of the required switching field, and will maintain their previous state. The shape memory feature makes it possible to scan through the actuators and set the desired strain state on each one, in a manner similar to that of raster displays. This type of row column addressing would be a major advantage when constructing adaptive systems with thousands of actuators, as required in adaptive telescope mirrors.

With the above addressing scheme, some actuators can experience as much as half of the field applied to the target region. This can be reduced at the expense of increasing the size of the affected region. This is accomplished by applying a mixture of +V, +V/3, -V/3 and -V volts to different electrodes, as shown in Figure 6.2b. The target region still experiences the full electric field, while the remainder of the ceramic experiences one third of that field. In either scheme, it is the presence of the deadband in the material response which makes row/column addressing possible.

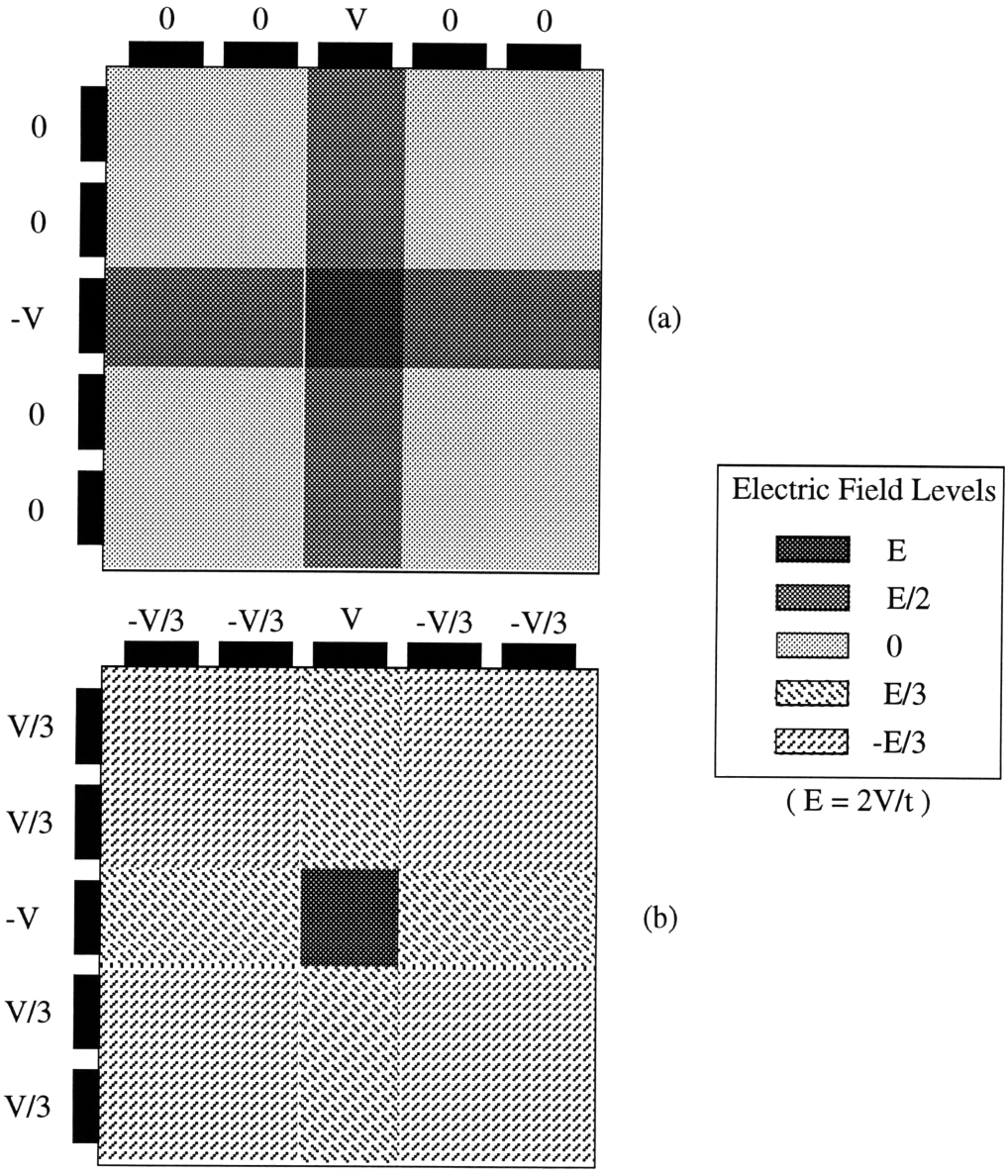

Figure 6.2 - Two different addressing schemes using row/column electrodes.

6.2 Development of a Prototype Adaptive Mirror

The knowledge gained from the material tests has been used to design of an adaptive optical mirror. Two prototype mirrors were constructed, each with four piezoceramic wafers mounted on the rear (Figure 6.3). The first mirror was actuated with PZT-5H (12.5 mil thick) piezoceramic wafers, and the second with A3 (15 mil thick) wafers. A 0.5 mil thick copper coated kapton sheet was bonded to the rear surface of a 7.5 cm long, 1.25 cm wide, and 0.1 cm thick plane glass mirror, to provide a ground terminal for the ceramic wafers which were bonded on top. The ceramic wafers were 1.5 cm by 1.25 cm in dimension and were separated by 1 mm.

The same analysis used to calculate the stiffness of the ceramic from partial clamping data, can be used to obtain a prediction of the mirror deflection. The strain and curvature for a bimorph (Figure 6.4) are calculated using Classical Laminated Plate Theory

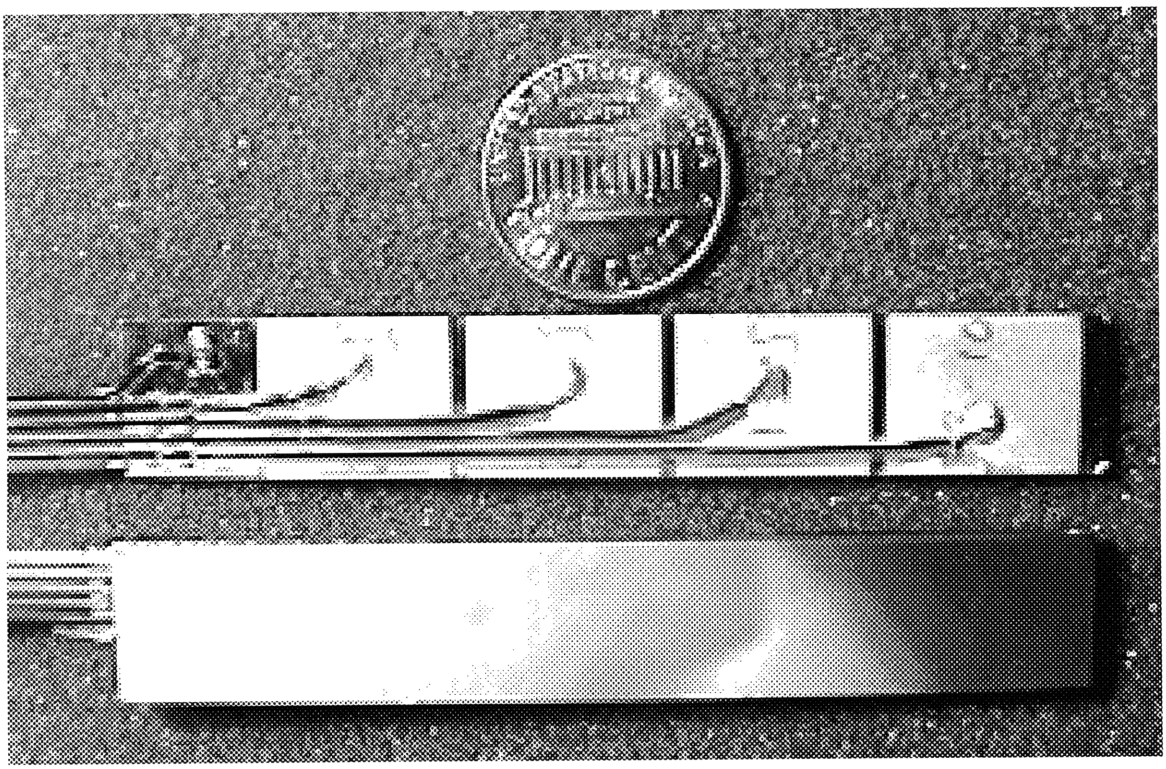

Figure 6.3 - The front and back views of the adaptive mirror.

with induced strain in Appendix A. The results of this analysis are summarized by (A.22):

$$\kappa = -6\frac{\psi(1+\tau)\Lambda}{t^a(1+4\psi+6\psi\tau+4\psi\tau^2+\psi^2\tau^2)}$$
$$S^o = \frac{(4\psi\tau^2+9\psi\tau+6\psi+1)\Lambda}{(1+4\psi+6\psi\tau+4\psi\tau^2+\psi^2\tau^2)} \qquad \text{(A.22)}$$

where S^o is the in-plane strain at z=0, and κ is the curvature. τ and ψ are the thickness and stiffness ratios of the mirror and the actuator as defined by (A.20). Λ is the in-plane strain the actuator would experience under free conditions. For any level of actuation specified by Λ, (A.22) can be used to calculate the curvature induced by the actuator. Making the simplifying assumption that the curvature of the mirror is κ directly above the actuators, and zero in between actuators, it can be integrated over the length of the mirror to obtain the profile of the mirror.

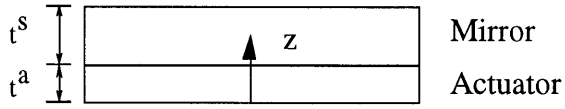

Figure 6.4 - The geometry of the mirror bimorph.

Published stiffness values were used to calculate plane stress c_{11}^* and c_{12}^* (and thus c^a) for the PZT-5H wafers as well as the c^s for the glass (Appendix B). The experimentally derived value from Chapter 4 was used for the A3 wafers. The relevant data for the model is listed in Table 6.1.

Table 6.1- Data used in mirror deflection predictions.

	PZT -5H	A3		Glass
t^a (mm)	0.317	0.381	t^s (mm)	1.0
c_{11}^* (GPa)	66.2	--	E (GPa)	65.0
c_{12}^* (GPa)	19.2	--	ν	0.16
c^a (GPa)	85.4	116	c^s (GPa)	77.4
Λ (με)	220†	430††		

† Corresponding to E=0.6 kV/mm (85% of coercive field).

†† Corresponding to E=1.0 kV/mm.

The deformations were measured by directing multiple laser beams to points on the surface of the adaptive mirror. The multiple beams were obtained by using a diffraction grating (Ronchi ruling) placed in the path of the laser. The reflected beams were observed on a screen placed 3 m from the mirror (Figure 6.5). Deformation of the mirror causes movement of the image points on the screen. The position of the image points were recorded and used to calculate the mirror deflection. Since the deflections of the mirror are quite small, only the slope of the mirror surface is responsible for the movement of the laser beams. Using a small angle approximation, it is a simple task to calculate the slope of the surface from the movement of the laser beams. The slope can then be integrated numerically to obtain the profile of the mirror.

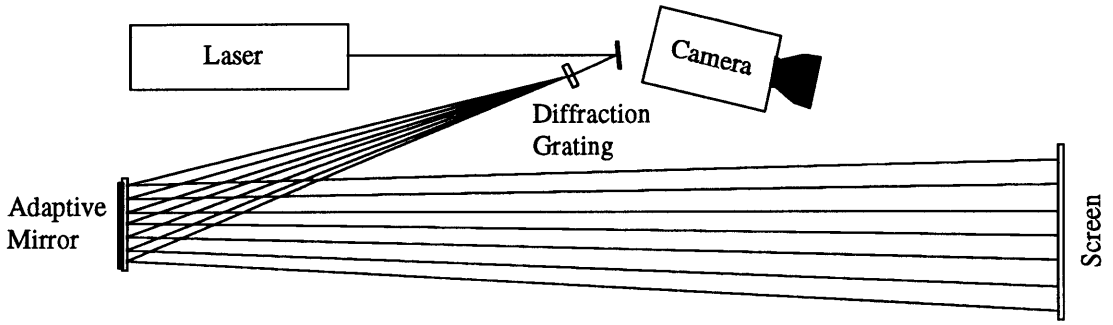

Figure 6.5 - Experimental Setup used to measure mirror deflection.

Figure 6.6 shows the tip deflection of the A3 mirror during the quasi static application of various field levels. All four wafers were actuated. The electric field was changed in 0.5 kV/mm steps at one minute intervals. At each new field level a 30 second settling time was allowed, and then deflections were measured. Also shown in the figure are the predicted tip deflections obtained by integrating the curvature from (A.22). The predictions were carried out using both the experimentally measured free strain (Λ) and the free strain from the material model (as in Figure 5.11). There is fairly good agreement between all three curves. There is a slight discrepancy in the location of the phase transition and the residual strain at zero field which can be attributed to frequency response of the material. This results from using free strain values obtained at 0.01 Hz in the model. The 30 second settling time, during which some decay in the strain takes place, is not accounted for in the model.

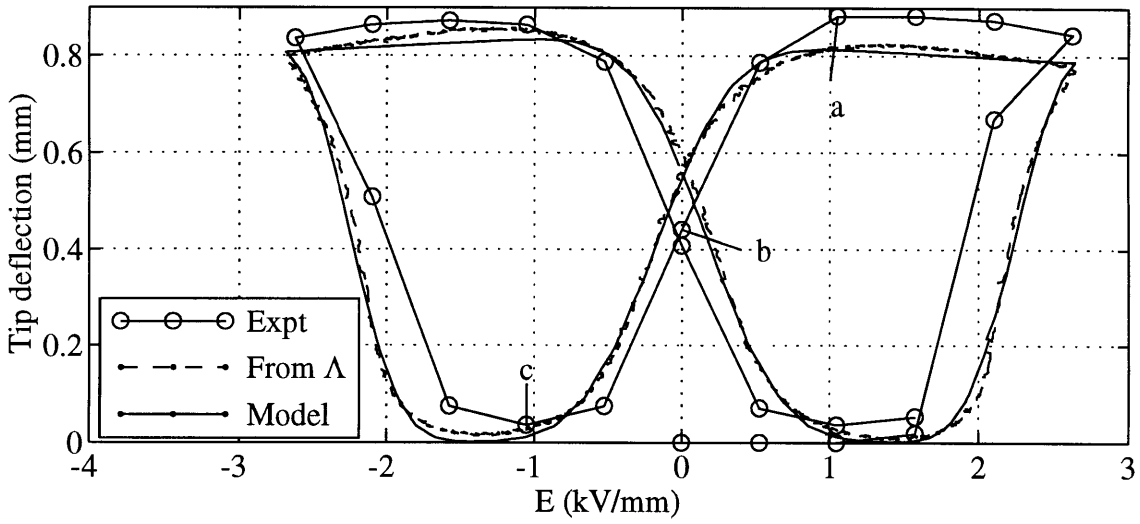

Figure 6.6 - Experimentally determined tip deflection of the shape memory ceramic actuated adaptive mirror at different applied field levels. The curve is compared to predicted tip deflections based on measured free strain, and free strain obtained from material model

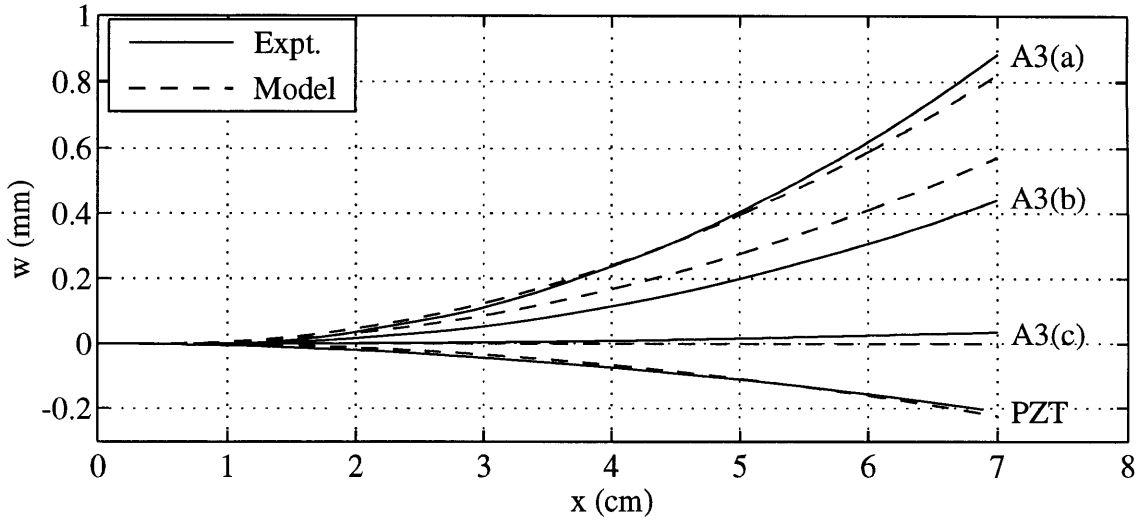

Figure 6.7 - Centerline deflection of the PZT-5H actuated mirror, and the shape memory ceramic (A3) actuated mirror. The PZT mirror deflection is shown for an applied field of 0.6 kV/mm. The A3 mirror defection is shown for a) 1 kV/mm, b) 0 kV/mm, and c) -1 kV/mm (corresponding to labels in Figure 6.6). For each case, the corresponding model predicted shapes on measured free strains are also shown.

Figure 6.7 shows the centerline profile of each mirror, as measured experimentally and as predicted based on (A.22). In each case, all four wafers were actuated. The PZT mirror deflection is shown for an applied electric field of 0.6 kV/mm, which is approximately 85% of the coercive field of the material. The mirror deflection was measured at several field levels. The centerline deflection is shown at three field values which correspond to points labeled in Figure 6.6. The good agreement of the experimentally measured deflection of the PZT mirror with the predictions serve to validate the calculations based on the experimental setup and the model. Good agreement is also seen for the A3 mirror in cases (a) and (c). In case (b) which corresponds to the electric field being zero, the model over predicts the deflection. Again, this is caused by not accounting for the decay in the strain which occurs during the 30 second settling time.

The presence of shape memory is clearly observed in this application. While the PZT mirror would require a sustained electric field to maintain its deflection, the A3 mirror remains deformed even after the field has been switched off (Figure 6.7b). The residual deflection in the mirror using PLZST is as high as the deflection of the PZT mirror, where the PZT material is driven to 85% of its coercive field.

6.3 Design of Full Scale Adaptive Mirror

The prototype adaptive mirror constructed during this study utilized the transverse strain produced by ceramic wafers to cause deformations in a bimorph fashion. The size of the features that can be induced is on the same order as the size of the actuators themselves. Thus, to correct small imperfections, small actuators would have to be used. For the type of adaptive optics described §6.1, which would improve the diffraction limit of a mirror by correcting surface imperfections, one requires the ability to induce deformations with higher spatial frequency (with as many as 300 actuators). As the area of each individual actuator is made smaller relative to its thickness, it becomes less effective in actuating in a bimorph fashion. An alternative method of actuation is to bond the rear surface of the electroceramic actuators to a stiff back structure (Figure 6.8), and thus cause deformations in the mirror surface through longitudinal strain.

Each method has advantages and disadvantages which make them suitable for different applications. With the bimorph type actuation the curvature of the mirror is affected, and since the mirror need only be pinned at a few points, fairly large deflections maybe obtained. This method is only capable of inducing deformations with low spatial

frequency. It is therefore best suited for applications such as controlling the focal length of a mirror. With the longitudinal mode of actuation, deformations with higher spatial frequency can be induced, and thus, very small surface features may be controlled. The amplitude of the deformation, however, is significantly smaller and is limited by the longitudinal stroke of the ceramic. This method of actuation is well suited for improving the diffraction limit of space based optics. As described earlier, such an application requires control over small features of the mirror, while the amount of stroke required is only a fraction of the wavelength of interest.

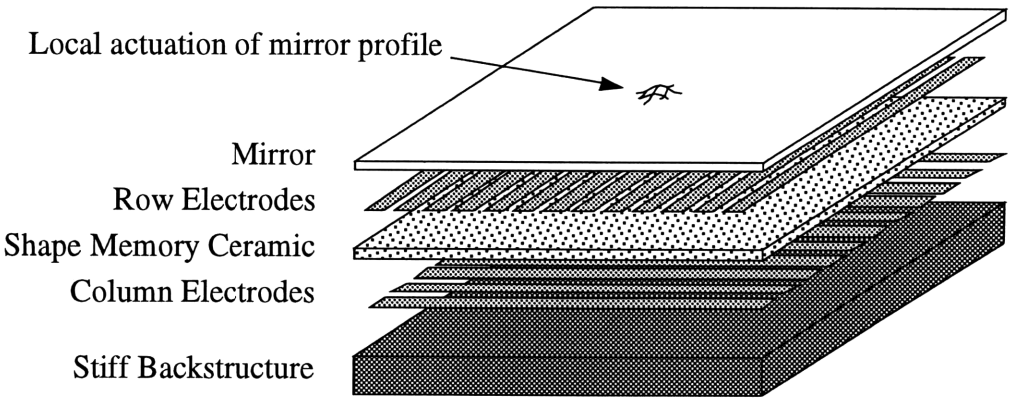

Figure 6.8 - Schematic of adaptive mirror with stiff back structure.

As the individual actuator area is reduced, the impact of neighboring actuators on one another becomes significant. Therefore, it becomes important to model the system as a full 3 dimensional structure in order to analyze the relative importance of such effects in actuation capability. The following sections will discuss a finite element model and a Rayleigh-Ritz model developed to study such effects.

6.3.1 Finite Element Mirror Model

To study the effects of small actuator size and the influence of neighboring actuators on the actuation capability, a solid three dimensional model was constructed. Various geometries were investigated using ANSYS, a finite element program capable of modeling piezoelectric material as Multifield Solid Elements [25]. The model code is listed in Appendix D. The objective of this model was to study the effects of neighboring actuators and tradeoffs between the actuator area, thickness, and spacing.

A representative volume element was selected for modeling. As seen in Figure 6.9, the representative volume element consists of a quadrant of an active actuator along with portions of the neighboring actuators. Two possible geometries were considered, shown in Figure 6.10. In case A, the actuators are physically segmented, while in case B a single ceramic is used and the actuators are only electrically isolated. The actuators were assumed to be squares with side p and separated by spacing s. The thickness of the actuator and the mirror were assumed to be h and t respectively. An electric field was then applied to the actuator at the origin, and the deformations of the mirror surface were computed. Symmetry conditions were assumed on the x=0 and y=0 faces of the representative volume. The z=0 face was clamped to model the stiff back structure. Free boundary conditions were assumed on the other three surfaces. While this neglects the rest of the structure, it is sufficient for a preliminary investigation since most of the deformation occurs near the actuated ceramic.

In an actual application, the maximum required deformation of the surface will dictate the actuator thickness. This could be computed in terms of the longitudinal strain achieved by the material. For the purposes of the model a thickness of 0.25 mm (~10 mil) was used for the ceramic, and a voltage of 100V was applied across the region being actuated. Other dimensions were varied for each run. Since the model is linear, all results can then be scaled for the actual actuator thickness. It is the effect of relative dimensions which is of interest in the present discussion, and not the absolute values themselves. Hence, all the comparisons made between the various FEM runs, as well as the Rayleigh-Ritz model, are performed in terms of relative dimensions. The actuator width (p), the gap size (s), and the mirror thickness (t) are each nondimensionalized relative to the ceramic thickness (h). Throughout the discussion, the actuator width to thickness ratio (p/h) is referred to as the aspect ratio of the actuator.

As indicated by the results from our prototype mirror, an adaptive structure utilizing shape memory actuators can be effectively modeled using an induced strain approach. Thus, one need not worry about the nonlinearity of the material behavior for the present computations. Deformations of the structure may be computed for an arbitrary electric field and then scaled according to the free strain of the material. With this point in mind, the FEM models were implemented using PZT-5H properties, since complete material stiffness and coupling matrices were not available for the shape memory ceramic.

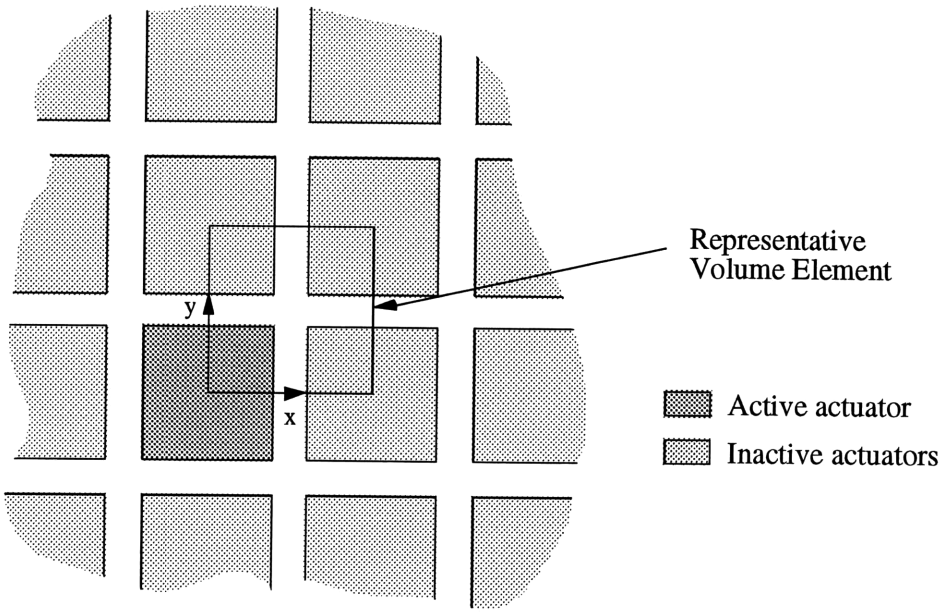

Figure 6.9 - Representative volume element for FEM studies.

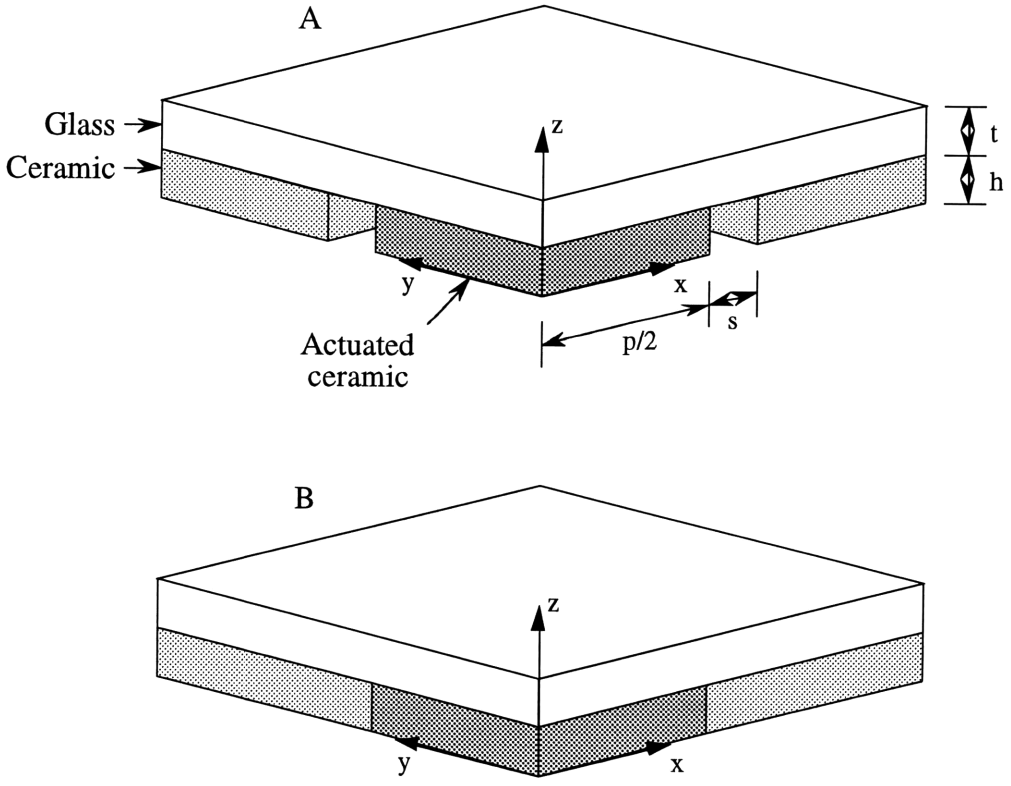

Figure 6.10 - Segmented vs. connected actuators.

The deformations in the mirror were calculated for different actuator widths as well as different gap sizes between the actuators. Figures 6.11-6.13 show contour maps of the deformation in the out of plane direction for some typical cases. As expected, the mirror surface is raised in the region above the actuator. It should be noted, however, that as the aspect ratio of the actuators is increased, the maximum deflection does not occur at the center of the actuator, but in a region close to the corner. This phenomenon is only observed for the cases with segmented actuators and is further discussed below.

Figure 6.14 shows the maximum out of plane surface deformation observed in the FEM model as a function of the actuator width to thickness ratio (p/h). Curves are shown for three different values of actuator gap size (s/h). Also shown are the out of plane surface deformation at the center of the actuator. For any given gap size, it can be seen that the maximum deflection and the center deflection are the same at low actuator aspect ratios. That is to say, the maximum deflection occurs at the center of the actuator. At higher aspect ratios, the mirror surface takes on a bowl shape, with the maximum deflection occurring near the corner of the actuator. This shows up in Figure 6.14 as a decrease in the center deflection curves relative to the maximum deflection curves. It should be noted that the observed deflections have a definite peak as a function of actuator aspect ratio (p/h).

The effect of increasing the actuator gaps can also be seen in Figure 6.14. The portion of the mirror between the actuator segments constrains the deformation caused by the actuator. Increasing the gap size softens this resistance, and thus increases the deflection of the mirror. Figure 6.15 presents similar results for the case of unsegmented actuators. In this case, the gap between active regions is filled with piezoceramic. Since the material in this region isn't being directly actuated, it effectively provides additional stiffness which the active region has to overcome. Thus much smaller deformations are observed. It was also found that unsegmented actuators, unlike the previous case, don't exhibit a sharp peak in the deflection as a function of aspect ratio. This will be explained with the help of the Rayleigh-Ritz model in the next section.

A series of runs were performed with different glass thicknesses. The Z deformation contour maps from these runs are shown in Figure 6.13. Figure 6.16 shows the center deflections and the maximum deflections obtained from these runs, at mirror thickness to ceramic thickness ratios of 0.5, 1, and 1.5. The reduction in mirror thickness softens the constraint on the ceramic and thus increases the observed deflection. The position of the peaks is also shifted in the process.

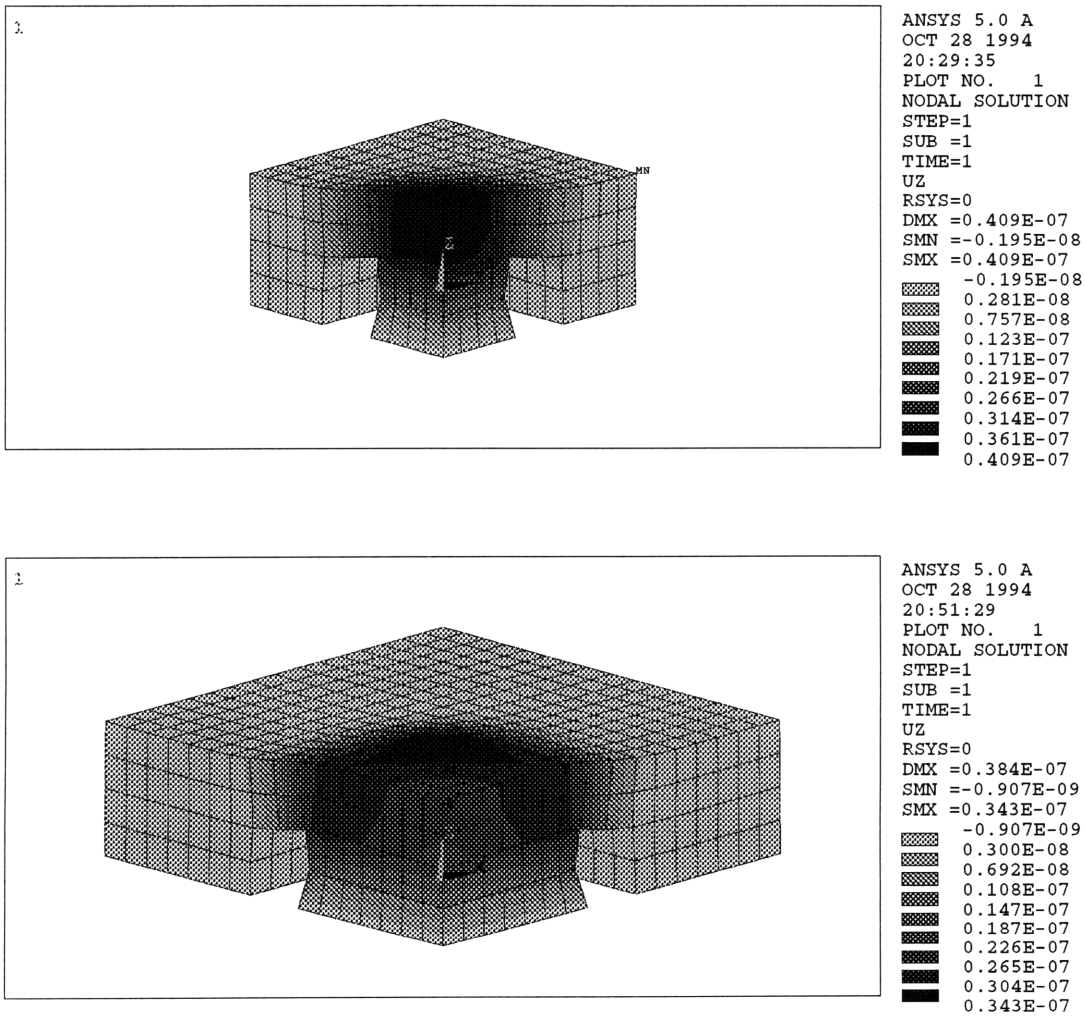

Figure 6.11 - Z direction displacement contours for a segmented adaptive mirror with p/h=3, and 6. In both cases s/h=t/h=1.

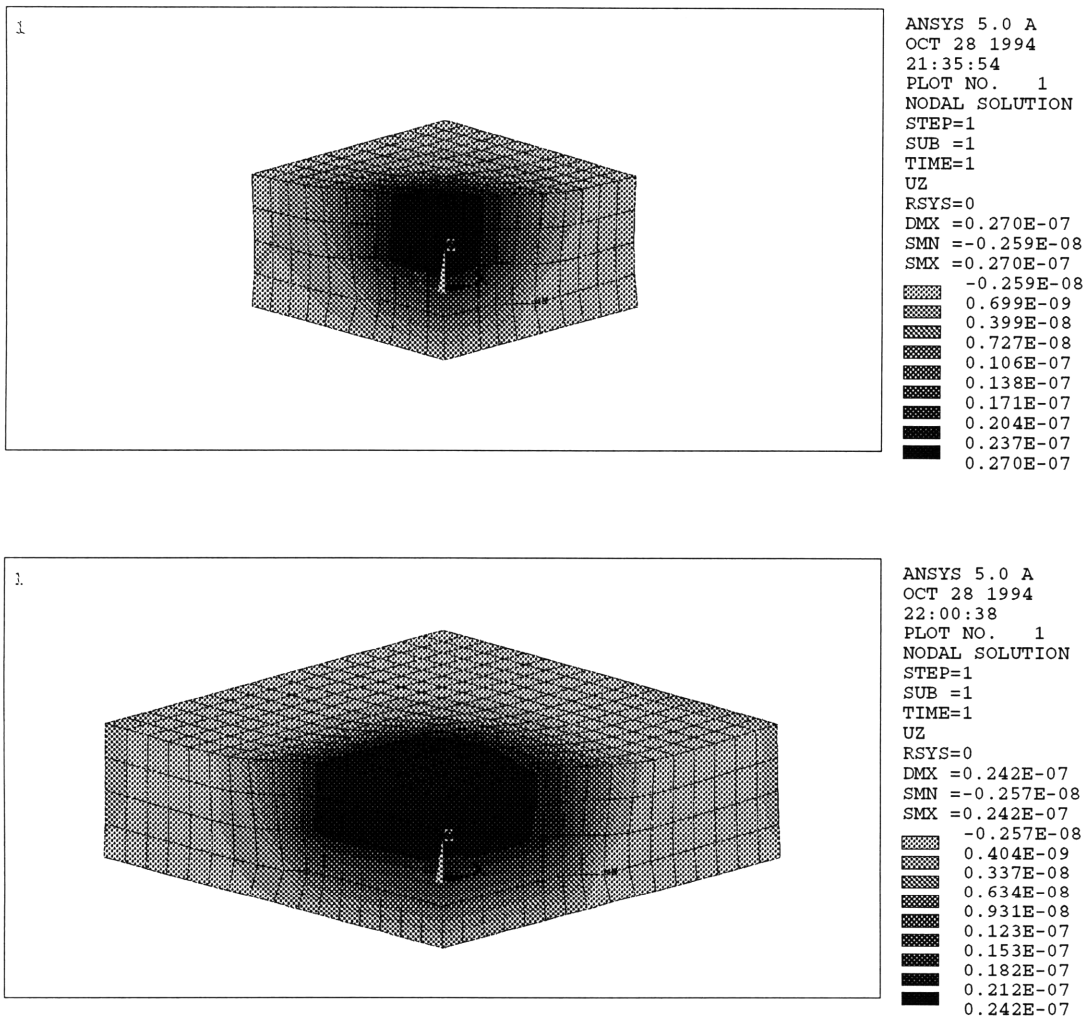

Figure 6.12 - Z direction displacement contours for a non-segmented adaptive mirror with p/h=3, and 6. In both cases s/h=t/h=1.

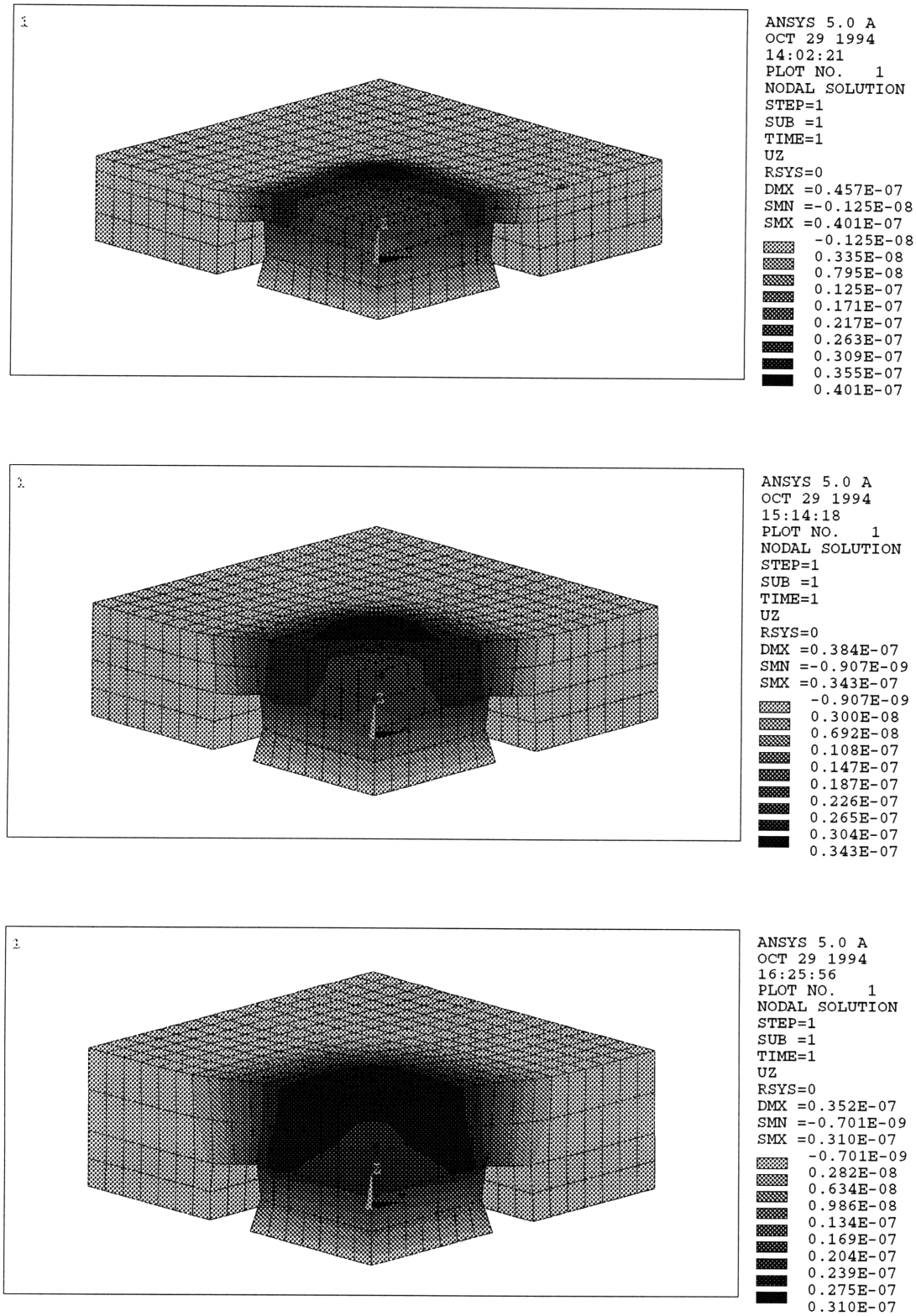

Figure 6.13 - Z direction displacement contours for a segmented adaptive mirror with t/h= 0.5, 1, 1.5. In all three cases s/h=1 and p/h=6.

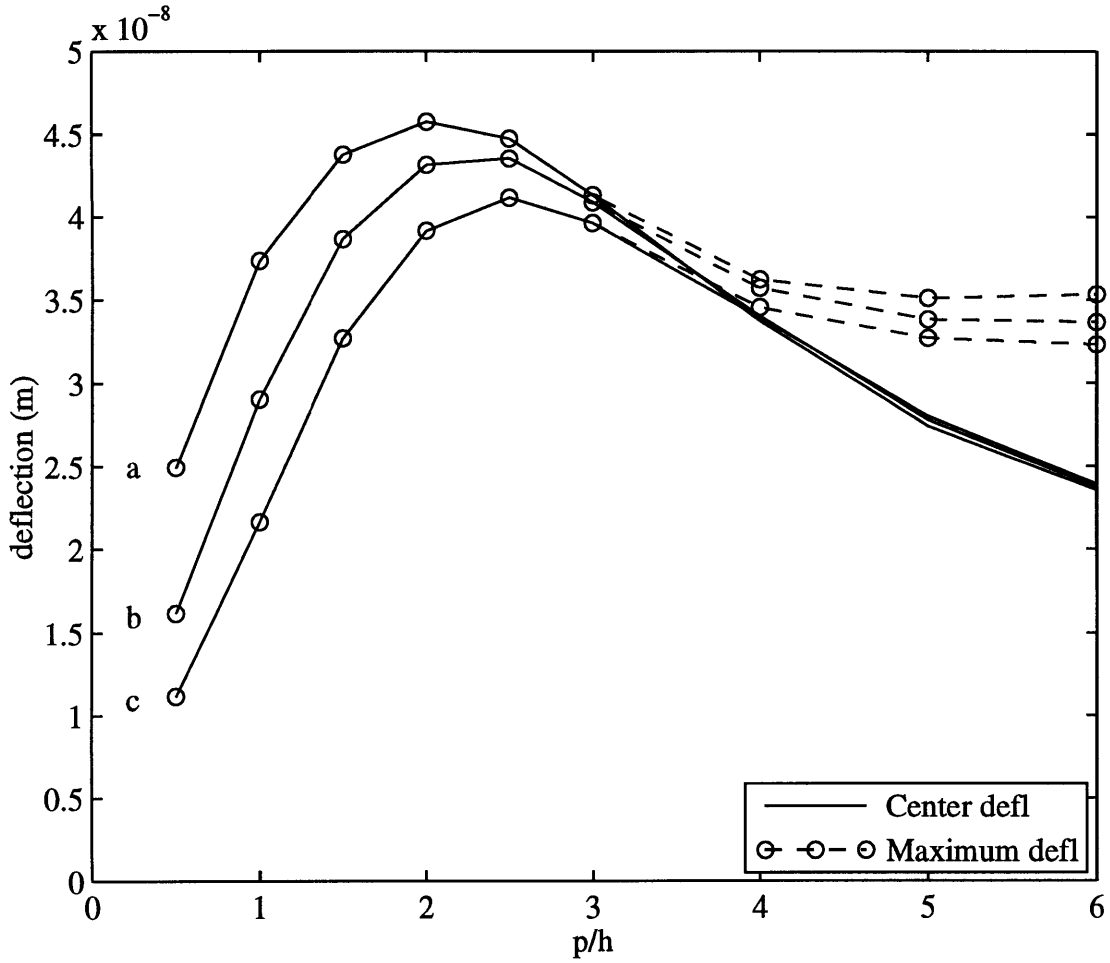

Figure 6.14 - Out of plane surface deflection of a segmented adaptive mirror for different gap sizes. Both the peak deflection and the deflection at the center of actuator are shown. The curves correspond to t/h=1, and three different gap size to ceramic thickness ratios: a) s/h=0.5 b) s/h=1.0 c) s/h=2 .

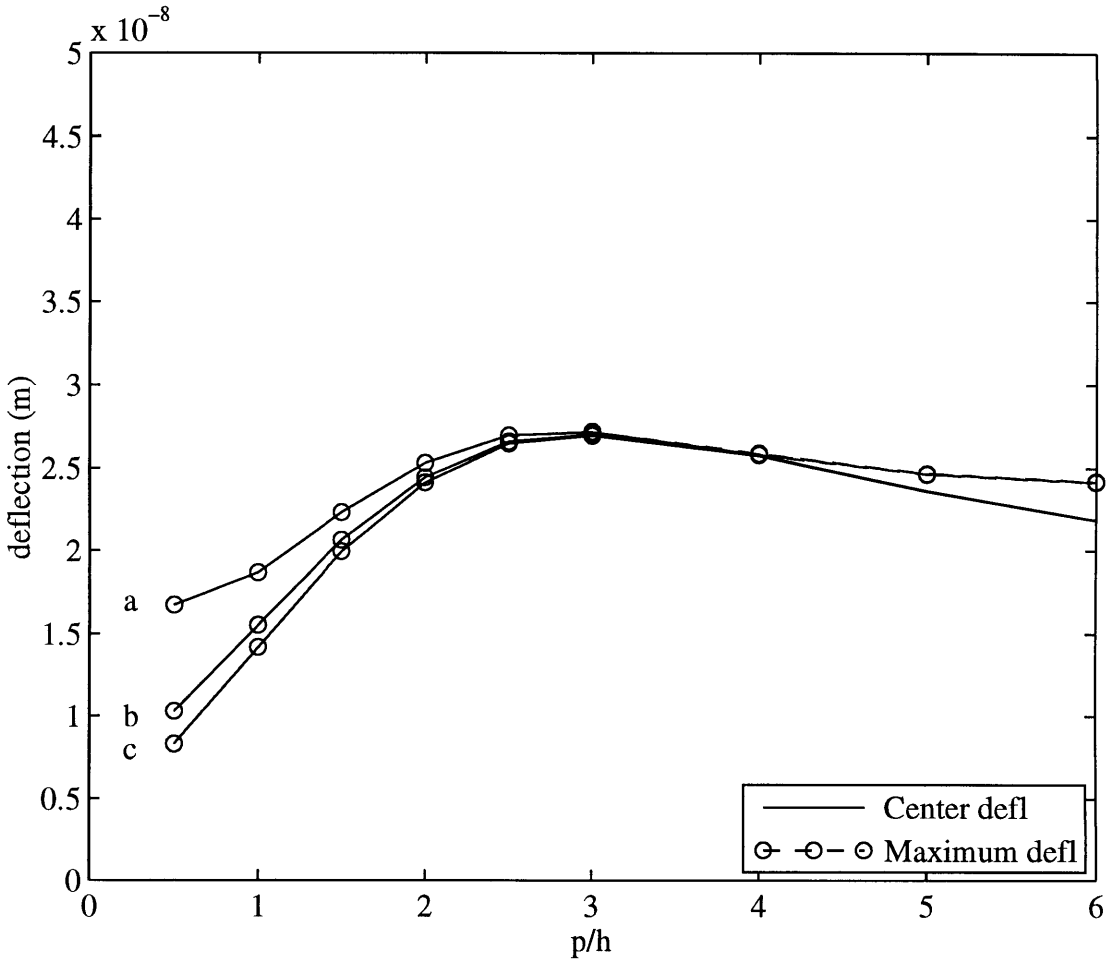

Figure 6.15 - Out of plane surface deflection of a non-segmented adaptive mirror for different gap sizes. Both the peak deflection and the deflection at the center of actuator are shown. The curves correspond to t/h=1, and three different gap size to ceramic thickness ratios: a) s/h=0.5 b) s/h=1.0 c) s/h=2 .

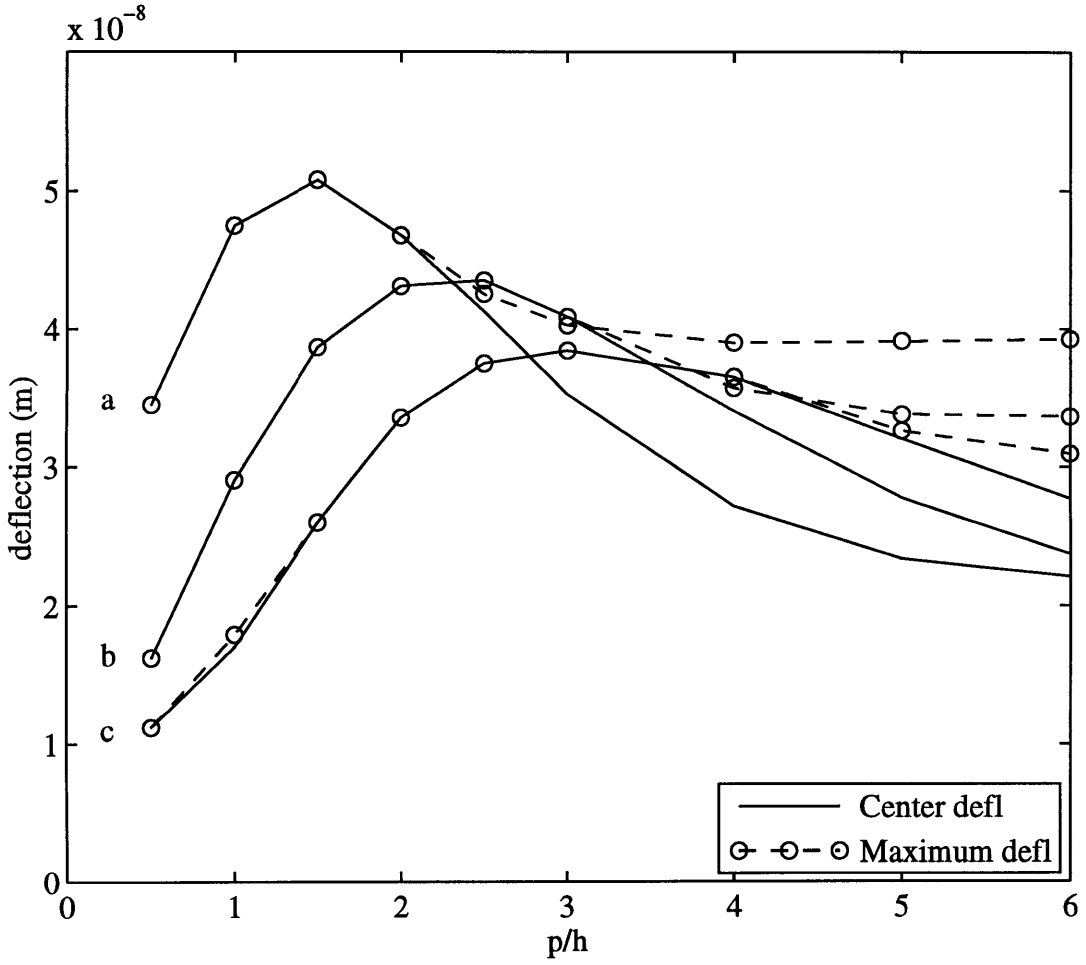

Figure 6.16 - Out of plane surface deflection of a segmented adaptive mirror for different glass thicknesses. Both the peak deflection and the deflection at the center of actuator are shown. The curves correspond *s/h*=1, and to three different glass/ceramic thickness ratios: a) *t/h*=0.5 b) *t/h*=1.0 c) *t/h*=1.5 .

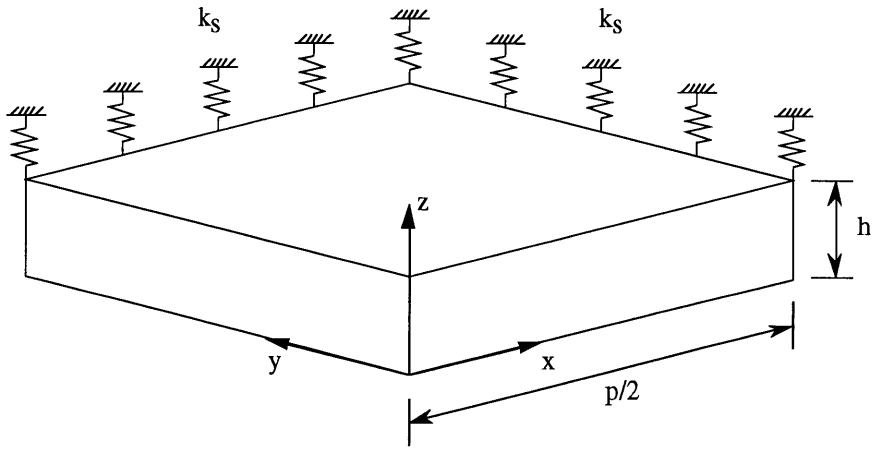

Figure 6.17 - Setup of the Rayleigh-Ritz model. The edges of the actuator are attached to distributed springs with stiffness per unit length of k_S.

6.3.2 Rayleigh-Ritz Mirror Model

To obtain an understanding of the FEM results, a simple model of the system based on variational principles is used as described by Hagood *et al.* [15]. The system being modeled simply consists of an electroceramic with distributed stiffness along the edge as in Figure 6.17. k_S is the stiffness per unit length along the edge of the actuator. It represents the glass connecting the neighboring actuators.

The constitutive relation for a piezoceramic, detailed in Appendix A, is given by:

$$\begin{bmatrix} \underline{\mathbf{T}} \\ \underline{\mathbf{D}} \end{bmatrix} = \left[\begin{array}{c|c} \underline{\underline{\mathbf{c}}}^E & -\underline{\underline{\mathbf{e}}}^T \\ \hline \underline{\underline{\mathbf{e}}} & \underline{\underline{\varepsilon}}^S \end{array}\right] \begin{bmatrix} \underline{\mathbf{S}} \\ \underline{\mathbf{E}} \end{bmatrix} \tag{6.2}$$

The Generalized Hamilton's Principle for a coupled electromechanical system is:

$$\int_{t_1}^{t_2} \left[\left(\partial T - \partial U + \partial W_e - \partial W_m \right) + \partial W \right] dt = 0 \tag{6.3}$$

where U is the mechanical energy, T is the kinetic energy, and W_e, W_m, and W are the electrical, magnetic, and mechanical work terms respectively. For the purposes of quasistatic analysis, the integral can be omitted. Also, ignoring the kinetic and magnetic energy terms, this can be written as:

$$-\partial U + \partial W_e + \partial W = 0 \tag{6.4}$$

The mechanical and electrical energy terms are:

$$\partial U = \iiint_V \partial \mathbf{S}^T \mathbf{T} dV \quad , \quad \partial W_e = \iiint_V \partial \mathbf{E}^T \mathbf{D} dV \tag{6.5}$$

The mechanical work term due to applied surface stresses and applied charges to the electrodes are:

$$\partial W = \iint_S \partial \mathbf{u} \cdot \mathbf{T}_S dA - \sum \partial \varphi_i \cdot q_i \tag{6.6}$$

Where, $\mathbf{T_S}$ is the vector of applied surface stresses to each surface, and φ_i and q_i are the voltage and total charge on each electrode.

To find a solution for the system, assumed shape functions for the displacement and the voltage potential are needed. Table 6.2 shows some of the shape functions used for displacement. The first three consist of displacements in the Z direction and are responsible for producing the deformations on the mirror surface. They are of the form:

$$\begin{aligned} u_x &= 0 \\ u_y &= 0 \qquad\qquad n = 0,2,4,... \\ u_z &= \tilde{z}\left(1-\tilde{y}^n\right)\left(1-\tilde{x}^n\right) \end{aligned} \tag{6.7}$$

The shape functions are written in terms of nondimensionalized coordinates $\tilde{x} = 2x/p$, $\tilde{y} = 2y/p, \tilde{z} = z/h$. It was desired to allow extra degrees of freedom in the X and Y directions, corresponding to possible deformations at the edges of the actuators. In the system of interest, the ceramic is clamped in the transverse direction by the rigid back structure. The mirror itself will also partially clamp the top surface of the ceramic. But the ceramic can undergo transverse strains away from the top and bottom surfaces. Thus, the shape functions were assumed to be zero along the z=0 and z=h surfaces. Shape functions satisfying these conditions were suggested by the results of the finite element model and are of the form:

$$\begin{aligned} u_x &= \tilde{x}\left((2\tilde{z}-1)^n - 1\right) \\ u_y &= \tilde{y}\left((2\tilde{z}-1)^n - 1\right) \qquad n = 2,4 \\ u_z &= 0 \end{aligned} \tag{6.8}$$

Table 6.2- Some possible shape functions for use in the Ritz model.

(1)	$u_x = 0$ $u_y = 0$ $u_z = \tilde{z}$	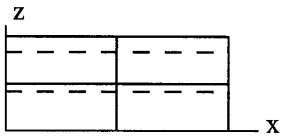
(2)	$u_x = 0$ $u_y = 0$ $u_z = \tilde{z}\left(1-\tilde{x}^2\right)\left(1-\tilde{y}^2\right)$	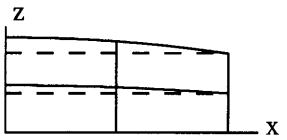
(3)	$u_x = 0$ $u_y = 0$ $u_z = \tilde{z}\left(1-\tilde{x}^4\right)\left(1-\tilde{y}^4\right)$	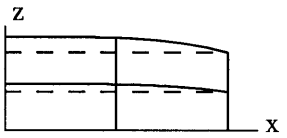
(4)	$u_x = \tilde{x}\left((2\tilde{z}-1)^2-1\right)$ $u_y = \tilde{y}\left((2\tilde{z}-1)^2-1\right)$ $u_z = 0$	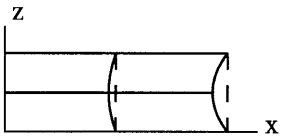
(5)	$u_x = \tilde{x}\left((2\tilde{z}-1)^4-1\right)$ $u_y = \tilde{y}\left((2\tilde{z}-1)^4-1\right)$ $u_z = 0$	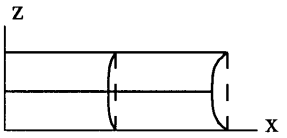
(6)	$u_x = \tilde{x}$ $u_y = \tilde{y}$ $u_z = 0$	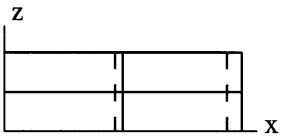
	Sample combination of shape functions.	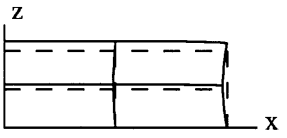

A shape function was also included with uniform strain in the X and Y direction. This shape function does not meet the boundary conditions at z=0 and z=h, and was only used in some of the calculations to gain some insight into the problem.

Having selected shape functions, the total deformation field can be written as a matrix product:

$$\mathbf{u} = \Psi_r \mathbf{r} \quad , \quad \Psi_r = \begin{bmatrix} u_x^{(1)} & u_x^{(2)} & \cdots \\ u_y^{(1)} & u_y^{(2)} & \cdots \\ u_z^{(1)} & u_z^{(2)} & \cdots \end{bmatrix} \quad , \quad \mathbf{r} = \begin{Bmatrix} r_1 \\ r_2 \\ \vdots \end{Bmatrix} \tag{6.9}$$

where Ψ_r is the matrix containing the shape functions and **r** is the column vector containing the coefficients. Based on the deformation fields, one can then calculate the strains by applying the operator:

$$\mathbf{L}_r = \begin{bmatrix} \frac{\partial}{\partial x} & 0 & 0 \\ 0 & \frac{\partial}{\partial y} & 0 \\ 0 & 0 & \frac{\partial}{\partial z} \\ 0 & \frac{1}{2}\frac{\partial}{\partial z} & \frac{1}{2}\frac{\partial}{\partial y} \\ \frac{1}{2}\frac{\partial}{\partial z} & 0 & \frac{1}{2}\frac{\partial}{\partial x} \\ \frac{1}{2}\frac{\partial}{\partial y} & \frac{1}{2}\frac{\partial}{\partial x} & 0 \end{bmatrix} \tag{6.10}$$

The vector of strains (**S**) can then be expressed as:

$$\mathbf{S} = \mathbf{N}_r\mathbf{r} \quad , \quad \mathbf{N}_r = \mathbf{L}_r \Psi_r \tag{6.11}$$

where N_r contains the strain shape functions. Shape functions for the electric potential are also required. The potential can be expressed as:

$$\varphi = \Psi_v \mathbf{v} \tag{6.12}$$

where Ψ_v is the matrix containing the shape functions and **v** is the column vector containing the coefficients. Voltage shape functions must be constant along the electrodes. Only one voltage shape function was used, assuming the whole actuator experiences a uniform field in the Z direction. This assumption is satisfied by the choice:

$$\varphi = -z / h \tag{6.13}$$

So the electric field can be obtained by taking the gradient of the potential:

$$\mathbf{E} = \mathbf{N}_v\mathbf{v} \qquad \mathbf{N}_v = -\mathbf{L}_v \Psi_v \tag{6.14}$$

where L_v is the gradient operator. The constitutive relation for the piezoceramic (6.2) and the assumed shape functions (6.11,6.14) are substituted into the work and energy terms (6.5,6.6). The resulting integrals can be written as:

$$\begin{aligned} \partial W &= \partial\mathbf{r}^T\mathbf{F}_r - \partial\mathbf{v}^T\mathbf{F}_v \\ \partial U &= \partial\mathbf{r}^T\mathbf{K}\mathbf{r} - \partial\mathbf{r}^T\Theta^T\mathbf{v} \\ \partial W_e &= \partial\mathbf{v}^T\Theta\mathbf{r} + \partial\mathbf{v}^T\mathbf{C}\mathbf{v} \end{aligned} \tag{6.15}$$

where the following definitions were made in the above calculations:

$$\begin{aligned}
\mathbf{K} &= \iiint_V \mathbf{N}_r^{\mathsf{T}} \mathbf{c}^E \mathbf{N}_r dV \\
&\quad + \int_0^{p/2} k_s \mathbf{N}_r^{\mathsf{T}} \mathbf{N}_r \Big|_{\substack{z=h \\ y=p/2}} dx + \int_0^{p/2} k_s \mathbf{N}_r^{\mathsf{T}} \mathbf{N}_r \Big|_{\substack{z=h \\ x=p/2}} dy \\
\Theta &= \iiint_V \mathbf{N}_v^{\mathsf{T}} \mathbf{e} \mathbf{N}_r dV \\
\mathbf{C} &= \iiint_V \mathbf{N}_v^{\mathsf{T}} \varepsilon^S \mathbf{N}_v dV \\
\mathbf{F}_r &= \iint_A \Psi_r^{\mathsf{T}} \mathbf{T}_s dA \\
\mathbf{F}_v &= \sum_i \Psi_v^{\mathsf{T}} q_i
\end{aligned} \tag{6.16}$$

Substituting back into Hamilton's equation (6.4):

$$\begin{aligned}
0 &= -\partial \mathbf{r}^{\mathsf{T}} \mathbf{K} \mathbf{r} + \partial \mathbf{r}^{\mathsf{T}} \Theta^{\mathsf{T}} \mathbf{v} + \partial \mathbf{v}^{\mathsf{T}} \Theta \mathbf{r} + \partial \mathbf{v}^{\mathsf{T}} \mathbf{C} \mathbf{v} + \partial \mathbf{r}^{\mathsf{T}} \mathbf{F}_r + \partial \mathbf{v}^{\mathsf{T}} \mathbf{F}_v \\
&= \partial \mathbf{r}^{\mathsf{T}} (-\mathbf{K} \mathbf{r} + \Theta^{\mathsf{T}} \mathbf{v} + \mathbf{F}_r) + \partial \mathbf{v}^{\mathsf{T}} (\Theta \mathbf{r} + \mathbf{C} \mathbf{v} - \mathbf{F}_v)
\end{aligned} \tag{6.17}$$

Which gives the system of equations:

$$\begin{bmatrix} \mathbf{F}_r \\ \hline \mathbf{F}_v \end{bmatrix} = \left[\begin{array}{c|c} \mathbf{K} & -\Theta^{\mathsf{T}} \\ \hline \Theta & \mathbf{C} \end{array}\right] \begin{bmatrix} \mathbf{r} \\ \hline \mathbf{v} \end{bmatrix} \tag{6.18}$$

The top relation in (6.18) is referred to as the actuator equation, while the bottom one is the sensor equation. Assuming no external forces ($\mathbf{F}_r$=**0**), all that remains is to carry out the integrations for **K**, Θ, and **C**. This operation was performed using Maple, a symbolic mathematics software. The actuation relation can then be inverted to obtain the shape function coefficients under an applied field:

$$\mathbf{r} = \mathbf{K}^{-1} \Theta^{\mathsf{T}} \mathbf{v} \tag{6.19}$$

The surface deflection of the mirror can then be obtained from

$$\mathbf{u} = \Psi_r \mathbf{r}\big|_{z=h} \tag{6.20}$$

Table 6.3-Shape functions used in each model.

	(1)	(2)	(3)	(4)	(5)	(6)
A	√					
B	√					√
C	√			√	√	
D	√	√	√			
E	√	√	√			√
F	√	√	√	√	√	

By evaluating (6.20), the surface deformation at the point (x=y=0, z=h) can be expressed in terms of the actuator width to height aspect ratio p/h, and k_s (the spring stiffness / unit length). To simplify the expressions, α is defined to equal p/h. Figure 6.18 shows the results of this model. Each subplot in the figure shows the deflection obtained by including a different set of shape functions in the model (Table 6.3). The different curves in each subplot correspond to different values of k_s. Increasing k_s would correspond to increasing the mirror thickness, or lowering the gap size between actuators. If only uniform longitudinal strain is allowed (shape function 1) this analysis yields

$$u_z = \frac{1.979\times10^{-8}\alpha}{3.406\times10^{-11}k_s + \alpha} \tag{6.21}$$

This result could have been obtained by simply using the constitutive relation for the material, and balancing the force generated by the piezoceramic with the load in the springs. The use of the Rayleigh-Ritz approach is only required to allow the addition of more complex shape functions. As seen from (6.21), as the aspect ratio increases, the deformation approaches an asymptote. As the aspect ratio is decreased, the deformation goes to zero. Ignoring the edge effects, the stress produced by the actuator is independent of its area. Thus the actuation force on the mirror is proportional to the actuator area. The mirror is however restrained by the neighboring regions, with a force which is proportional to the length of the actuator circumference. The balance between these two effects is responsible for the shape of the curves in subplot A.

If the piezoceramic is also allowed to strain in the transverse direction (i.e. using shape functions 1 & 6) the result is

$$u_z = \frac{5.930\times10^{-8}\alpha}{8.280\times10^{-11}k_s + \alpha} \tag{6.22}$$

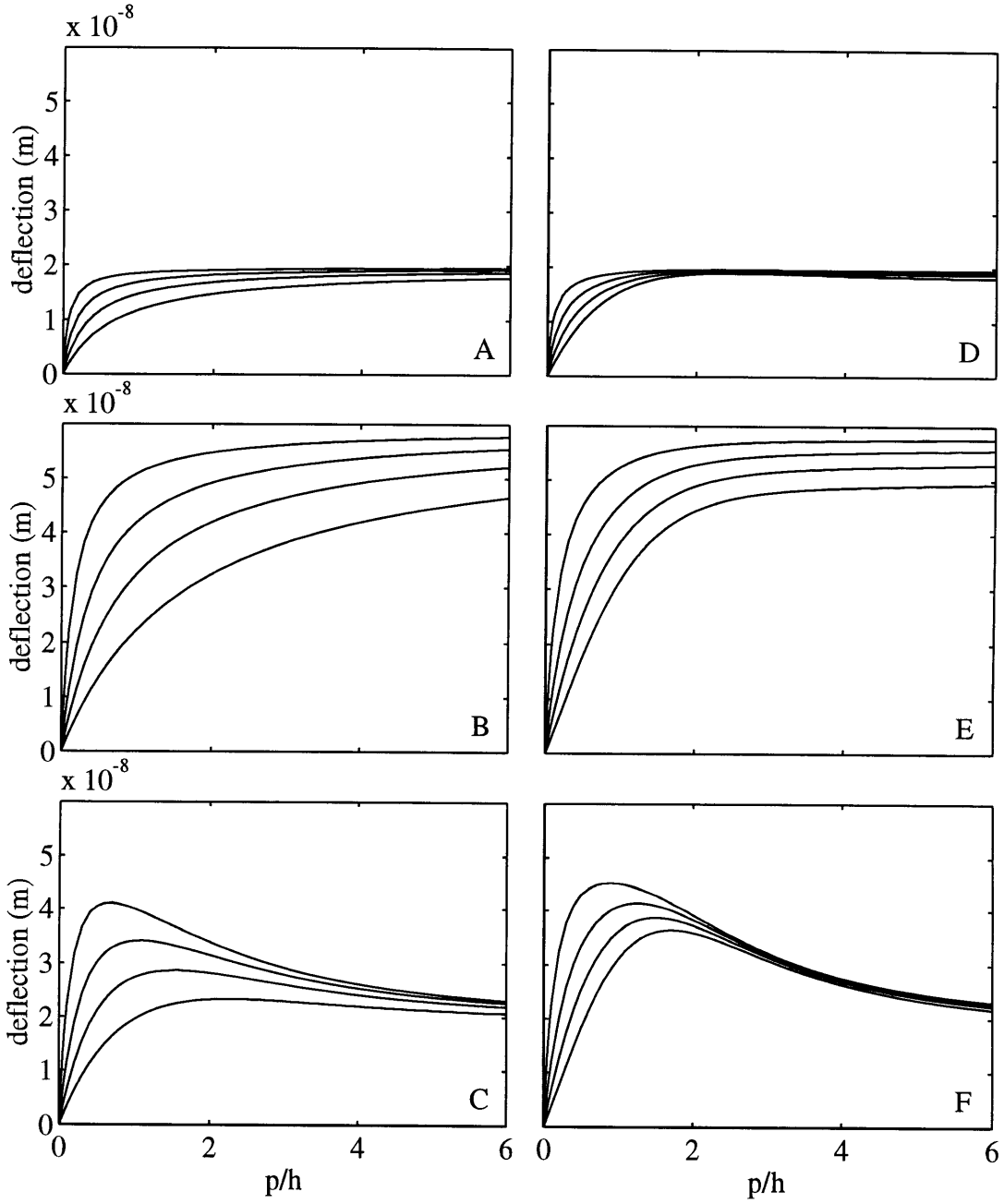

Figure 6.18 - Center deflection of the mirror from the Ritz model using different sets of shape functions. The curves in each plot correspond to k_S values of 2, 5, 10, and 20 GPa in order of decreasing deflection. See Table 6.3 for list of shape functions.

The shape of the curves in subplot B, as well as the physical reason for them is the same as those of subplot A. But, since the material is no longer being constrained due to Poisson effects, the magnitude of the strain is increased. However, shape function 6 does not meet the boundary conditions of the problem. If instead shape functions 1, 4, and 5 are used, we obtain

$$u_z = \frac{(2.801+2.796\alpha^2+0.198\alpha^4)\times 10^{-7}\alpha}{(3.961+4.098\alpha^2+0.341\alpha^4)\times 10^{-10}k_s+(5.240+6.719\alpha^2+\alpha^4)\alpha} \quad (6.23)$$

As seen from subplot C, the deflection curves approximate the results in subplot B at low actuator aspect ratios, while they approach the values in subplot A at high aspect ratios. Thus it can be concluded that at low aspect ratios the ceramic is in effect free in the transverse direction, and not constrained by the Poisson effect. This results in the peak observed in the deflection at some optimum aspect ratio. This conclusion applies to adaptive mirrors with segmented actuators (i.e. case A). For non-segmented actuators however, the material between the actuated regions, constrains the transverse deformations at the actuator edge. This diminishes the peak and reduces the overall deformation in the mirror. Thus it can be seen that it is beneficial to segment the actuators.

Subplots D, E, and F show similar results, while also including two more longitudinal shape functions. The addition of these shape functions causes a slight shift in the location of the peaks, resulting in slightly better agreement with the FEM model. Of course, the Rayleigh-Ritz model does not represent the mirror stiffness accurately, and has significantly lower degrees of freedom than the finite element model. But, while its results do not match the FEM results exactly, it helps in the understanding of those results.,

6.4 Summary

The development of an adaptive mirror was pursued as one of the possible applications of shape memory ceramics. Diffraction is the limiting factor in the performance of space telescopes at low wavelengths. Active compensation can be used to reduce figure errors in optical mirrors, and thus reduce scattered light at lower wavelengths. Furthermore, adaptive optics can be utilized to increase the dynamic range of space telescopes permitting the imaging of faint and bright objects which are in close proximity.

A prototype mirror was manufactured utilizing four PLZST wafers as bimorph actuators, and compared to a similar mirror using PZT wafers. Tests on the mirror verified

an induced strain actuation model used to predict mirror deflections. They also demonstrate the feasibility of constructing structures which are capable of maintaining a residual deflection, by using the shape memory of the ceramic material. That is, for sufficiently flexible structures, the material continues to exhibits a remnant strain despite structural stress.

A full adaptive mirror designed to reduce figure errors would have to utilize smaller actuators in a longitudinal actuation mode. A 3 dimensional finite element model was generated and used to study the edge effects as actuator size is reduced. A Rayleigh-Ritz model was also formulated to obtain closed form expressions in terms of the actuator width to thickness ratio for a simplified geometry. The Rayleigh-Ritz results were used to verify and provide an understanding of the finite element results. It was found that as actuator area is reduced the structural stiffness of the mirror becomes dominant, reducing the observed deformations. Also, larger deformations would be induced if the ceramic were not constrained in the transverse direction due to Poisson's effect. The transverse clamping is imposed by the bond between the ceramic and the stiff backstructure. By segmenting the actuators and reducing the actuator area to thickness ratio the material is allowed to strain in the transverse direction despite the clamping due to the backstructure. This increases the observed deflection.

7 Summary & Conclusions

A great deal of work has been performed in recent years on smart structures utilizing control systems to satisfy ever more demanding requirements. Integrated actuators have been used to reduce vibrations, compensate for thermal strains, and perform aeroelastic control. The increasing use of distributed actuators is accompanied by a demand for improved actuation authority and a need for developing new materials capable of producing higher strain levels. Large strains are associated with the lattice distortions which occur during the antiferroelectric to ferroelectric phase transition in certain types of ceramics. For certain compositions, the phase transition may be induced by the application of electric field, making it possible to use such material as actuators.

Several compositions in the lead lanthanum zirconate stannate titanate (PLZST) and lead niobium zirconate stannate titanate (PNZST) families of piezoceramics, exhibiting AFE-FE phase transition, were investigated for the purpose of utilizing their large strain and shape memory in structural actuation. Of the lanthanum doped compositions which were manufactured and tested, the composition labeled A3 exhibited AFE-FE transition. Longitudinal strains of approximately 2200 $\mu\varepsilon$ and transverse strains of approximately 400 $\mu\varepsilon$ were observed in these samples. Niobium doped compositions also provide shape memory and slightly higher strains. The PNZST composition labeled B1 produced strains of 2700 $\mu\varepsilon$ in the longitudinal direction and 650 $\mu\varepsilon$ in the transverse direction. Higher longitudinal strains could be attained by increasing the field level. However, this also increases the possibility of arcing across the sample electrodes.

The residual strain was found to be a higher fraction of the peak strain in the transverse direction than in the longitudinal direction. This is attributed to the superposition

of an anisotropic field strain relation, during the FE state, on the strain due to AFE-FE phase transition. This may be important in a shape memory based application of the material. In such an application the applied electric field will be primarily zero, with non-zero fields only applied to induce a transition. Two possible strain levels at zero field are desired. The excess strain observed during the application of the electric field would produce an overshoot in the deformation of the structure. Since less excess strain is observed in the transverse direction, transverse actuation is more suitable for shape memory based switching applications.

Numerous issues important in the use of such a material in applications have been examined. Both the transition field levels and strain magnitudes of the samples were found to be temperature dependent. At zero field the material appears to be metastable in both the ferroelectric and antiferroelectric phases over a limited range of temperatures. In this region, field induced phase transitions provide a mechanism for actuation. Energetically, both the FE and AFE phases correspond to local minima, thus shape memory is observed. Increasing the temperature produces more rapid decay of the residual strain. This is likely caused by the increased thermal energy which would lower the effective energy barrier for the FE to AFE phase transition. At high enough temperatures no shape memory will be present. If only the ferroelectric phase is stable, the material behaves like a conventional piezoelectric. This was the case with B1 material at temperatures slightly below room temperature. Using some of the strain-temperature curves obtained from experiments, it is possible to determine the optimal operating temperature for each composition, to either maximize peak strain or residual strain. The B1 samples appeared to be much more sensitive to changes in temperature.

The importance of investigating strain under partially clamped conditions was also presented. It is necessary to ensure that structural backstress will not inhibit phase transition in the material. In addition, partially clamped tests provide a means of calculating the stiffness of the ceramic. The brittle nature of ceramic wafers makes it difficult to use conventional tensile testing machines for this purpose. Using the data obtained from partially clamped samples the effective in-plane extensional stiffness* for the A3 material was found to be 116 GPa.

Material response was also examined as a function of frequency. It was found that due to the hysteresis in the actuator, significant heating of the sample is observed at high

---

* See effective stiffness defined in §A.2.

Table 7.1 - Summary of A3 material properties.

Maximum longitudinal strain† at 20°C	2200 με
Maximum transverse strain† at 20°C	400 με
AFE→FE transition field at 20°C	2.5 kV/mm
Effective in-plane extensional stiffness††	116 GPa
Optimum temperature for maximum transverse strain	34°C
Optimum temperature for remnant transverse strain	20°C

frequencies. This should be an important consideration in any application design. Some of the properties of the A3 material are summarized in Table 7.1. More details can be found in §4.

A one dimensional model intended to capture the antiferroelectric to ferroelectric phase transition has been presented. Two internal variables are used to represent the fraction of the material in the FE+ and FE- states. These are related to the applied field, the external stress, and the strain of the material through a proposed constitutive relation. The evolution of the two internal variables is calculated by considering multiple families of crystalline domains with a distribution of properties such as transition field levels. By optimizing model parameters using experimental strain data, the model can reproduce the overall shape of the field-strain curves. Unlike other phenomenological transition models found in the literature, the multiple family model is capable of producing correct response for arbitrary field amplitudes. The frequency response of the model can be adjusted to match the trends observed in the material. While the frequency dependence of the strain amplitude could not be exactly reproduced, there is good qualitative agreement in the field-strain curves.

More comprehensive characterization of the material is required to determine some of the material properties which could not be obtained during this study. The full 6×6 stiffness matrix for the material was not determined. Furthermore, it is necessary to ascertain if the stiffness varies as a function of the phase. Once the stiffness has been fully characterized, it will be possible to construct a full 3-dimensional model of the material, using the transverse and longitudinal strain measurements available from the experiments.

---

† Electric field was limited to 3.2 kV/mm.

†† See effective stiffness defined in §A.2.

A prototype adaptive structure consisting of a four ceramic actuators bonded to a mirror was constructed and used to demonstrate the application of the material. The material model, along with a simple structural model based on Classical laminate Plate Theory, were used to successfully predict the behavior of the adaptive mirror. The experiments specially verified the presence of shape memory despite the structural stress on the ceramic.

Finite element models and Rayleigh-Ritz models were used to design a full-scale adaptive mirror consisting of an array of ceramic actuators mounted between a membrane mirror and a rigid support structure. The models were used to study the effect of actuator dimensions on performance in view of the geometric constraints created by the neighboring actuators. Two factors were found to be of importance. First, due to the stiffness of the mirror, the surface displacement produced by the actuator decreases as the actuator area is reduced, putting a practical limit on the minimum size of surface irregularities which could be corrected. Second, due to coupling of transverse and longitudinal strains through the Poisson effect, increased longitudinal strain is observed as the transverse clamping of the actuator is reduced. The transverse constraints can be reduced by segmenting the actuators, so that they do no constrain one another, and by reducing the area of each actuator.

The present study has characterized the behavior of PLZST and PNZST families of piezoceramics over a range of conditions. The results have demonstrated the feasibility of structural actuation using shape memory ceramics. The large strains associated with phase transition provide a great deal of actuation authority. Furthermore, the shape memory associated with the transition may be used to simplify construction of adaptive structures with large numbers of actuators. A successful application depends on a thorough understanding of the material behavior. The material response was found to be temperature dependent, which needs to be considered when selecting the optimum material composition for a given application. Also, stiffness of the controlled structure has a significant effect on the phase transition. The prototype structure built and tested during this study verified that use of the shape memory effect is possible even under structural loads. By considering the effect of each of these factors, it is possible to successfully design adaptive structures making full use of the properties of shape memory ceramics.

References

[1]. D. Berlincourt, H. H. A. Krueger, and B. Jaffe, "Stability of Phases in Modified Lead Zirconate with Variation in Pressure, Electric Field, Temperature and Composition", *J. Phys. Chem. Solids*, **25**, 1964, pp.659-674.

[2]. D. Berlincourt, H. Jaffe, and H. H. A. Krueger, "Release of Electric Energy in $PbNb(Zr,Ti,Sn)O_3$ by Temperature- and by Pressure-Enforced Phase Transitions", *Applied Physics Letters*, **3** (5), Sept 1 1963, pp 90-92.

[3]. D. Berlincourt, "Transducers Using Forced Transitions Between Ferroelectric and Antiferroelectric States", *IEEE Trans. Sonics Ultrason.* **SU-13**, 116 (1966).

[4]. D. Berlincourt, H. Krueger, C. Near, "Important properties of Morgan Matroc Piezoelectric Ceramics", TP-226, Electroceramics Division, Morgan Matroc, Inc.

[5]. N. Braithwaite and G. Weaver, Electronic Materials (Materials in action series), Alden Press, London, England, 1990.

[6]. W. G. Cady, Piezoelectricity, New York, McGraw-Hill Book Co. Inc., 1946, pp. 17.

[7]. K. H. Chan, N. W. Hagood, "Nonlinear Modeling of High Field Ferroelectric Ceramics for Structural Actuation", S.M. Thesis, Massachusetts Institute of Technology. Dept. of Aeronautics and Astronautics, Cambridge, MA, 1994

[8]. P. J. Chen, S. T. Montgomery, "A Macroscopic Theory for the existence of the Hysteresis and Butterfly Loops In Ferroelectricity", *Ferroelectrics*, **23** (1980), pp. 199-208.

[9]. J. S. Cory, J. L. McNichols, Jr., "Nonequilibrium Thermostatics", *J. Appl. Phys.*, **58** (9), Nov 1 1985, pp. 3282-3294.

[10]. E. F. Crawley, J. DeLuis, "Use of Piezoelectric Actuators as Elements of Intelligent Structures", *AIAA Journal* , **25** (10), 1987, pp. 1373-1385.

[11]. E. F. Crawley, K. B. Lazarus, "Induced Strain Actuation of Isotropic and Anisotropic Plates", *AIAA Journal*, **23** (6), June 1991, pp. 944-951.

[12]. L.E. Cross, "Antiferroelectric-Ferroelectric Switching in a Simple "Kittel" Antiferroelectric", *J. of the Physical Soc. of Japan*, **23** (1), Jul 1967, pp. 77-82.

[13]. L. E. Cross, "Polarization Controlled Ferroelectric High Strain Actuators", *J. of Intell. Mater. Syst. and Struct.*, **2** (Jul 1991), pp. 241-260.

[14]. K. Ghandi, and N. W. Hagood, "Shape Memory Ceramic Actuation of Adaptive Structures", *Proc. 35th AIAA/ASME/ASCE/AHS Structures, Structural Dynamics, and Material Conference*, Hilton Head, NC, 1994.

[15]. N. W. Hagood, W. H. Chung, and A. H. von Flotow, "Modeling of Piezoelectric Actuator Dynamics for Active Structural Control", *J. of Intell. Mater. Syst. and Struct.*, **1** (3), July 1990, pp. 327-354.

[16]. K. H. Hoffmann, "Mathematical Models of Dynamical Martensitic Transformations in Shape Memory Alloys", *J. of Intell. Mater. Syst. and Struct.*, **1**, Jul 1990, pp. 355-374.

[17]. IEEE Std 176-1978, IEEE Standard on Piezoelectricity, The Institute of Electrical and Electronics Engineers, 1978.

[18]. B. Jaffe, "Antiferroelectric ceramics with field-enforced transitions: a new nonlinear circuit element", *Proceedings of the IRE*, **49**, 1961, pp. 1261-1267.

[19]. R. M. Jones Mechanics of Composite Materials, Hemisphere Publishing Corp., New York, 1975, pp. 147-175

[20]. C. Kittel, "Theory of Antiferroelectric Crystals" *Physical Review*, **82** (5), June 1 1951, pp 729-732.

[21]. C. Liang, C. A. Rogers, "One-Dimensional Thermomechanical Constitutive Relations for Shape Memory Materials", *J. of Intell. Mater. Syst. and Struct.*, **1** (Apr 1990) pp. 207-234.

[22]. J. L. McNichols, Jr., J. S. Cory, "Thermodynamics of Nitinol", *J. Appl. Phys.*, **61** (3), Feb 1 1987, pp. 972-984.

[23]. K. Oh, A. Furuta, K. Uchino, "Field Induced Strains In Antiferroelectrics", *IEEE Ultrasonics Symposium* (1990), pp. 743-746.

[24]. K. Okada, "Phenomenological Theory of Antiferroelectric Transition. III. Phase Diagram and Bias Effects of First-Order Transition", *J. of the Physical Soc. of Japan*, **37** (5), Nov 1974, pp. 1226-1232.

[25]. D. F. Ostergaard, Coupled Field Analysis, Houston, PA: Swanson Analysis Systems, Inc., 1989.

[26]. W. Y. Pan, Q. M. Zhang, Q. Y. Jaiang, and L. E. Cross, "Electric Field Induced Strain in (Pb,La)(Ti,Zr)O_3 Ferroelectric Ceramics Near The Tetragonal-Rhombohedral Morphotropic Phase Boundary", *Ferroelectrics*, **88**, 1988, pp. 1-15.

[27]. W. Y. Pan, C. Q. Dam, Q. M. Zhang, and L. E. Cross, "Large displacement transducers based on electric field forced phase transitions in the tetragonal $(Pb_{0.97}La_{0.02})$(Ti,Zr,Sn)O_3 family of ceramics", *J. Appl. Phys.*, **66** (12), Dec 15 1988, pp. 6014-23.

[28]. C. B. Sawyer, C. H. and Tower, "Rochelle Salt as a Dielectric", *Physical Review*, **35** (Feb 1 1930), pp. 269-273.

[29]. M. Shao, "Active Optics for Space VIS/UV Imaging", Proposal to the JPL director's discretionary fund, Jet Propulsion Lab., Pasadena, California, Aug 20 1993.

[30]. G. Shirane, E. Sawaguchi, and Y. Takagi, "Dielectric Properties of Lead Zirconate", *Physical Review*, **8** (3), Nov 1 1951, pp. 476-481.

[31]. G. Shirane, F. Jona, R. Pepinsky, "Some Aspects of Ferroelectricity", *Proceedings of the IRE*, Dec 1955, pp. 1738-1793.

[32]. K. Uchino, "Digital Displacement Transducer Using Antiferroelectrics", *Proc. of 6th int. Meeting on Ferroelectricity. Jap. J. of Appl. Physics,* **24** (1985) Suppl 24-2 pp. 460-462.

Appendix A - Classical Laminated Plate Theory

A.1 Constitutive Relations

This section provides an overview of the standard constitutive relations used to describe 3 dimensional elastic bodies, and piezoceramics. In a general 3 dimensional elastic body, the relation between stress and strain can be written as:

$$\begin{aligned} \mathbf{S} &= \mathbf{sT} \quad \text{or} \quad \mathbf{T} = \mathbf{cS} \\ \mathbf{s} &= \mathbf{c}^{-1} \end{aligned} \tag{A.1}$$

where $\mathbf{S}$ is the 6×1 engineering strain vector, and $\mathbf{T}$ is the 6×1 stress vector:

$$\mathbf{S} = \begin{bmatrix} S_x \\ S_y \\ S_z \\ S_{yz} \\ S_{xz} \\ S_{xy} \end{bmatrix}, \quad \mathbf{T} = \begin{bmatrix} T_x \\ T_y \\ T_z \\ T_{yz} \\ T_{xz} \\ T_{xy} \end{bmatrix} \tag{A.2}$$

s is the 6x6 compliance matrix for the material, and **c** is the 6x6 stiffness matrix for the material. For an isotropic body, the compliance matrix has the form:

$$\mathbf{s} = \begin{bmatrix} s_{11} & s_{12} & s_{12} & 0 & 0 & 0 \\ s_{12} & s_{11} & s_{12} & 0 & 0 & 0 \\ s_{12} & s_{12} & s_{11} & 0 & 0 & 0 \\ 0 & 0 & 0 & s_{66} & 0 & 0 \\ 0 & 0 & 0 & 0 & s_{66} & 0 \\ 0 & 0 & 0 & 0 & 0 & s_{66} \end{bmatrix} \qquad (A.3)$$

$$s_{11} = \frac{1}{E}, \quad s_{12} = \frac{-\nu}{E}, \quad s_{66} = \frac{2(1+\nu)}{E}$$

where E is the Young's modulus for the material, and ν is the Poisson's ratio. The stiffness matrix has a similar structure. If the body is transversely isotropic, as is the case for a poled piezoceramic, the compliance matrix has the form

$$\mathbf{s} = \begin{bmatrix} s_{11} & s_{12} & s_{13} & 0 & 0 & 0 \\ s_{12} & s_{11} & s_{13} & 0 & 0 & 0 \\ s_{13} & s_{13} & s_{33} & 0 & 0 & 0 \\ 0 & 0 & 0 & s_{44} & 0 & 0 \\ 0 & 0 & 0 & 0 & s_{44} & 0 \\ 0 & 0 & 0 & 0 & 0 & s_{66} \end{bmatrix} \qquad (A.4)$$

When considering plate problems, only in-plane stresses and strains are of interest:

$$\mathbf{S} = \begin{bmatrix} S_x \\ S_y \\ S_{xy} \end{bmatrix}, \quad \mathbf{T} = \begin{bmatrix} T_x \\ T_y \\ T_{xy} \end{bmatrix} \qquad (A.5)$$

Using the plane stress assumption (T_z=T_{yz}=T_{xz}=0) the compliance matrix can be reduced by eliminating appropriate rows and columns. The reduced stiffness matrix is then calculated by inverting the reduced compliance matrix:

$$\mathbf{s}^* = \begin{bmatrix} s_{11} & s_{12} & 0 \\ s_{12} & s_{11} & 0 \\ 0 & 0 & s_{66} \end{bmatrix}, \quad \mathbf{c}^* = \begin{bmatrix} c_{11}^* & c_{12}^* & 0 \\ c_{12}^* & c_{11}^* & 0 \\ 0 & 0 & c_{66}^* \end{bmatrix} = \left(\mathbf{s}^*\right)^{-1} \qquad (A.6)$$

Note that while the elements of the $\mathbf{s}^*$ matrix have the same values as the standard values in the full 6x6 matrix, the elements of the $\mathbf{c}^*$ matrix have been modified. $(\cdot)^*$ is used to distinguish the reduced plane stress stiffness constants from their standard values. relation (A.1) can then be reduced to:

$$\mathbf{T} = \mathbf{c}^*\mathbf{S} \quad \text{or} \quad \mathbf{S} = \mathbf{s}^*\mathbf{T} \tag{A.7}$$

The distinction between the full 3 dimensional stress and strain vectors and the in plane stress and strain vectors will be obvious from context.

Like all elastic bodies, a piezoceramic material obeys relation (A.1). Due to the piezoelectric effect the stress (**T**) and strain (**S**) are also coupled to the electric field (**E**) and electric displacement (**D**) experienced by the material. The constitutive relation for a material with electromechanical coupling can be stated using the standard convention [17]:

$$\begin{bmatrix} \mathbf{T} \\ \mathbf{D} \end{bmatrix} = \left[\begin{array}{c|c} \mathbf{c}^E & -\mathbf{e}^{\mathsf{T}} \\ \hline \mathbf{e} & \varepsilon^S \end{array}\right] \begin{bmatrix} \mathbf{S} \\ \mathbf{E} \end{bmatrix} \tag{A.8a}$$

or

$$\begin{bmatrix} \mathbf{S} \\ \mathbf{D} \end{bmatrix} = \left[\begin{array}{c|c} \mathbf{s}^E & \mathbf{d}^{\mathsf{T}} \\ \hline \mathbf{d} & \varepsilon^T \end{array}\right] \begin{bmatrix} \mathbf{T} \\ \mathbf{E} \end{bmatrix} \tag{A.8b}$$

where $(\cdot)^{\mathsf{T}}$ denotes transpose. The superscript $(\cdot)^S$ signifies that the values are measured at constant strain (e.g. clamped), the superscript $(\cdot)^T$ signifies that the values are measured at constant stress (e.g. free strain), and the superscript $(\cdot)^E$ signifies that the values are measured at constant electrical field (e.g. short circuit). The piezoceramics couple the mechanical and electrical equations. In the form of the equations given in (A.8) the coupling terms are the piezoelectric constants which relate stress to applied field (the **e** constants), or the constants which relate strain to applied field (the **d** constants). These constants are related through the expression:

$$\mathbf{e} = \mathbf{d}\mathbf{c}^E \tag{A.9}$$

By convention, the z axis, is aligned with the direction of polarization of the piezoelectric material. In such a coordinate system, the matrix constitutive relations of the form of Equation (A.8a) can be expressed as:

$$\begin{bmatrix} T_x \\ T_y \\ T_z \\ T_{yz} \\ T_{xz} \\ T_{xy} \\ \hline D_x \\ D_y \\ D_z \end{bmatrix} = \left[\begin{array}{cccccc:ccc} c_{11}^E & c_{12}^E & c_{13}^E & 0 & 0 & 0 & 0 & 0 & -e_{31} \\ c_{12}^E & c_{11}^E & c_{13}^E & 0 & 0 & 0 & 0 & 0 & -e_{31} \\ c_{13}^E & c_{13}^E & c_{33}^E & 0 & 0 & 0 & 0 & 0 & -e_{33} \\ 0 & 0 & 0 & c_{55}^E & 0 & 0 & 0 & -e_{15} & 0 \\ 0 & 0 & 0 & 0 & c_{55}^E & 0 & -e_{15} & 0 & 0 \\ 0 & 0 & 0 & 0 & 0 & c_{66}^E & 0 & 0 & 0 \\ \hdashline 0 & 0 & 0 & 0 & e_{15} & 0 & \varepsilon_1^S & 0 & 0 \\ 0 & 0 & 0 & e_{15} & 0 & 0 & 0 & \varepsilon_1^S & 0 \\ e_{31} & e_{31} & e_{33} & 0 & 0 & 0 & 0 & 0 & \varepsilon_3^S \end{array}\right] \begin{bmatrix} S_x \\ S_y \\ S_z \\ S_{yz} \\ S_{xz} \\ S_{xy} \\ \hline E_x \\ E_y \\ E_z \end{bmatrix} \tag{A.10}$$

Note that due to symmetry the material properties are identical in the 1 and 2 directions. The first term in the subscript of the coupling coefficients refers to the electrical axis while the second refers to the mechanical. Thus e_{31} refers to the stress developed in the 1 direction in response to a field in the 3 direction (parallel to the material poling). Appendix B contains a listing of the material properties which have been used in various computations throughout this report.

A.2 Classical Laminated Plate Theory

Classical Laminated Plate Theory is used to model multiple layer structures such composite materials [19]. Structures such as the ones in Figure A.1 can also be modeled using CLPT by using the concept of induced stress.

The structure is assumed to undergo Bernoulli-Euler bending. That is to say, a plane through the thickness of the structure will remain planar, such that the strain at any point can be written as

$$\mathbf{S} = \mathbf{S}^o + \kappa z \tag{A.11}$$

where $\mathbf{S}^o$ is the in-plane strain vector at z=0, and κ is the curvature vector. Placing relation (A.11) into the stress-strain relation (A.7), the stress (**T**) can be written as:

$$\mathbf{T} = \mathbf{c}^*\mathbf{S} = \mathbf{c}^*(\mathbf{S}^o + \kappa z) \tag{A.12}$$

A plane stress assumption is used. Thus, $\mathbf{c}^*$ corresponds to the 3x3 stiffness matrix appropriate for plane stress. Proceeding with standard plate theory, the resultant loads (**N**) and moments (**M**) in the plate are calculated by integrating the stress through the thickness of the test article,

$$\begin{aligned} \mathbf{N} &= \int \mathbf{S}dz = \left(\int \mathbf{c}^* dz\right)\mathbf{S}^o + \left(\int \mathbf{c}^* z dz\right)\kappa \\ \mathbf{M} &= \int \mathbf{S}z dz = \left(\int \mathbf{c}^* z dz\right)\mathbf{S}^o + \left(\int \mathbf{c}^* z^2 dz\right)\kappa \end{aligned} \tag{A.12}$$

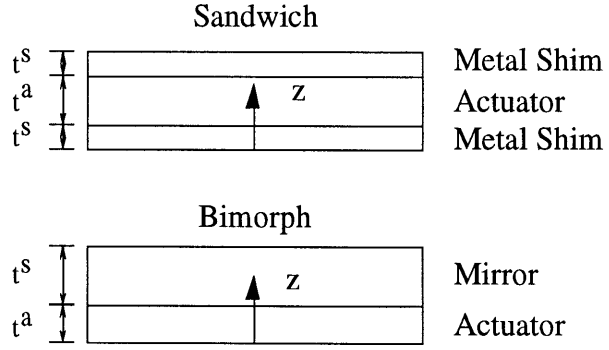

Figure A.1 - Cross section of sandwich and bimorph structures.

The quantities in parenthesis are functions only of the geometry and the material properties, and can be easily evaluated. Thus, matrices **A**, **B**, and **D** are defined to be:

$$\mathbf{A} = \int \mathbf{c}^* dz\,, \quad \mathbf{B} = \int \mathbf{c}^* z dz\,, \quad \mathbf{D} = \int \mathbf{c}^* z^2 dz \tag{A.13}$$

A is the extensional stiffness, **B** is the coupling stiffness, and **D** is the bending stiffness of the structure. To satisfy equilibrium conditions, the structural loads and moments must balance the induced loads and moments caused by the actuator. The induced loads and moments are given by

$$\mathbf{N}_e = \int_a \mathbf{c}^* dz \Lambda \qquad \mathbf{M}_e = \int_a \mathbf{c}^* z dz \Lambda \tag{A.14}$$

where $(\cdot)_e$ denotes electrically induced loads, and Λ is the vector of the ceramic free strains. The integrals in (A.14) are evaluated over the thickness of the active layers only. Equating the structural and induced loads and moments from (A.12) and (A.14), the following relation is obtained:

$$\begin{bmatrix} \mathbf{A} & \mathbf{B} \\ \mathbf{B} & \mathbf{D} \end{bmatrix} \begin{bmatrix} \mathbf{S}^o \\ \boldsymbol{\kappa} \end{bmatrix} = \begin{bmatrix} \mathbf{N}_e \\ \mathbf{M}_e \end{bmatrix} \tag{A.15}$$

Given the induced loads on the structure, Equation (A.15) can be solved for the strains and curvatures in system. If the structure and the loads in the problem under consideration are symmetric in the x and y directions, the resulting strains will also be symmetric. Hence,

$$\boldsymbol{\kappa} = \begin{bmatrix} \kappa_x \\ \kappa_y \\ \kappa_{xy} \end{bmatrix} = \begin{bmatrix} \kappa \\ \kappa \\ 0 \end{bmatrix} \quad \mathbf{S}^o = \begin{bmatrix} S_x^o \\ S_y^o \\ S_{xy}^o \end{bmatrix} = \begin{bmatrix} S^o \\ S^o \\ 0 \end{bmatrix} \quad \Lambda = \begin{bmatrix} \Lambda_x \\ \Lambda_y \\ \Lambda_{xy} \end{bmatrix} = \begin{bmatrix} \Lambda \\ \Lambda \\ 0 \end{bmatrix} \tag{A.16}$$

By substituting (A.16) into equation (A.15) and collecting terms the system can be simplified to:

$$\begin{bmatrix} A & B \\ B & D \end{bmatrix} \begin{bmatrix} S^o \\ \kappa \end{bmatrix} = \begin{bmatrix} N_e \\ M_e \end{bmatrix} \tag{A.17}$$

The problem has been reduced to a one dimensional system. The quantities A, B, D, N_e, and M_e are the effective values for the new system. They can be computed using

definitions similar to (A.13) and (A.14) by replacing the stiffness matrix $\mathbf{c}^*$ by the effective stiffness given by

$$c = c_{11}^* + c_{12}^* \tag{A.18}$$

The integrals in equations (A.13) and (A.14) can be evaluated in a piecewise manner over different layers. Superscript $(\cdot)^s$ and $(\cdot)^a$ will be used to distinguish the properties of the structural layers and the active layers. Note that for the structural layers, which are isotropic, the effective stiffness (A.18) can also be written in the form:

$$c^s = E/(1-\nu) \tag{A.19}$$

The final expressions will be simplified by defining the non-dimensional stiffness and thickness ratios as

$$\psi = t^s c^s / t^a c^a \qquad \tau = t^s / t^a \tag{A.20}$$

Evaluating A, B, D, N_e, and M_e for the sandwich problem, and solving (A.17) for the strain and curvature, one obtains

$$\kappa = 0 \qquad S^o = \frac{\Lambda}{1+2\psi} \tag{A.21}$$

Similarly, for the bimorph problem the equations yield

$$\begin{aligned} \kappa &= -6\frac{\psi(1+\tau)\Lambda}{t^a(1+4\psi+6\psi\tau+4\psi\tau^2+\psi^2\tau^2)} \\ S^o &= \frac{(4\psi\tau^2+9\psi\tau+6\psi+1)\Lambda}{(1+4\psi+6\psi\tau+4\psi\tau^2+\psi^2\tau^2)} \end{aligned} \tag{A.22}$$

The free strain of the ceramic due to the applied electric field (Λ) determines the level of actuation. Its value may be predicted using the material characterization data. Depending on the geometry of interest, expression (A.21) or (A.22) can be used to compute the deformation of the structure. This approach may also be used to model laminates with a more complicated arrangement of layers. This can be accomplished by computing the extensional, coupling, and bending stiffnesses for the structure and using appropriate expressions for the induced loads and moments.

Appendix B - Material Properties

The following tables contain values of the material properties for PZT-5H, used in various models in this report. These values are based on or derived from [4]. They represent low signal values at 25°C.

Table B.1 - Dielectric properties of PZT-5H at 1 kHz.

$\varepsilon_1^S/\varepsilon_o$	$\varepsilon_3^S/\varepsilon_o$
1700	1470
$\varepsilon_1^T/\varepsilon_o$	$\varepsilon_3^T/\varepsilon_o$
3130	3400

Table B.2 - Compliance properties of PZT-5H. units are (10^{-12} m^2/N).

s_{11}^E	s_{12}^E	s_{13}^E	s_{33}^E	s_{44}^E	s_{66}^E
16.5	-4.78	-8.45	20.7	43.5	42.6
s_{11}^D	s_{12}^D	s_{13}^D	s_{33}^D	s_{44}^D	s_{66}^D
14.05	-7.27	-3.05	8.99	23.7	42.6

Table B.3 - Stiffness properties of PZT-5H. units are (10^{10} $N/m^{2)}$.

c_{11}^E	c_{12}^E	c_{13}^E	c_{33}^E	c_{44}^E	c_{66}^E
12.72	8.02	8.47	11.74	2.30	2.35
c_{11}^D	c_{12}^D	c_{13}^D	c_{33}^D	c_{44}^D	c_{66}^D
12.96	8.27	7.20	16.01	4.22	2.35

Table B.4 - Piezoelectric properties of PZT-5H.
units are e (Coul/m^2), d (10^{-12} m/V)

e_{15}	e_{31}	e_{33}
17.0	-9.11	23.3
d_{15}	d_{31}	d_{33}
741	-274	593

The following Table contains plane stress stiffness constants for PZT-5H obtained by using Equation (A.6).

Table B.5 - Plane stress stiffness properties of PZT-5H.
units are (10^{10} N/m^2).

c_{11}^E	c_{12}^E	c_{66}^E
6.62	1.92	2.35
c_{11}^D	c_{12}^D	c_{66}^D
9.72	5.03	2.35

The following table contains values of the stiffness properties for selected isotropic material which are used in various models in this report.

Table B.6 - Stiffness properties of selected material.

Material	E (GPa)	ν
Brass	105	0.35
Steel	190	0.30
Aluminum	70	0.35
Glass	65	0.16

Appendix C - Material Model Code (MATLAB)

This Appendix contains a listing of the Matlab code used to implement the material model, which was presented in §5.2. First however, a few notes about the implementation are in order.

As described in §5.2.4, the model utilizes a distribution of families. The families are parametrized by two continuous parameters: E_f and E_r. The state of each family is described by two internal variables which are a function of these parameters: $n_1(E_f, E_r)$ and $n_2(E_f, E_r)$. For the purposes of numerical simulation it is necessary to replace these continuous functions with a discrete number of variables, n_1^{ij} and n_2^{ij}. Each of these variables corresponds to a range of E_f and E_r as shown in Figure C.1. The integral over the different families (5.25) can now be approximated by a summation over i and j:

$$\begin{aligned} N_1 &= \sum_i \sum_j f^{ij} n_1^{ij} \\ N_2 &= \sum_i \sum_j f^{ij} n_2^{ij} \end{aligned} \tag{C.1}$$

where f^{ij} is the population weighting for each family. It can be calculated in terms of the population density function $\mathrm{f}(\cdot)$ for the family distributions:

$$f^{ij} = \int_{-\Delta E_f/2}^{\Delta E_f/2} dE_f \int_{-\Delta E_r/2}^{\Delta E_r/2} dE_r \; \mathrm{f}(E_f^i + E_f, E_r^j + E_r) \tag{C.2}$$

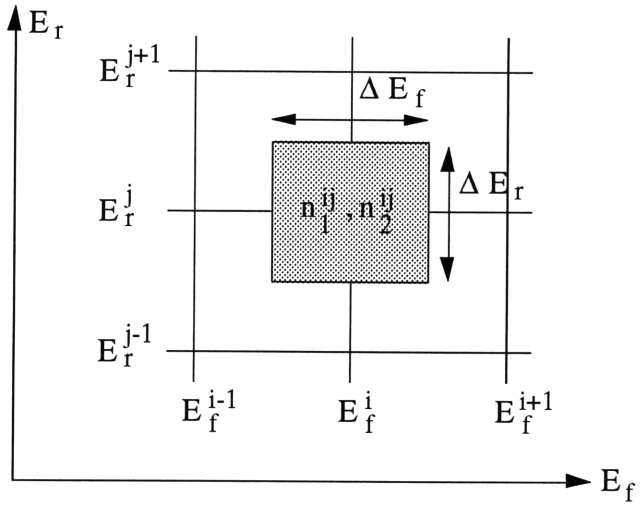

Figure C.1 - Discretization of the internal variables.

Since each variable corresponds to a range of E_f and E_r, the rate laws of §5.2.4 must be slightly modified. For example, during the AFE→FE+ transition, the following rate law applies to n_1:

$$E_f < E \qquad \Rightarrow \qquad \dot{n}_1 = \alpha_f(1 - n_1 - n_2) \qquad \text{(C.3)}$$

It is unclear what value for E_f should be used in the above condition. One may decide to use the mean of E_f for each family. With such a choice, N_1 calculated using (C.1) will appear quantized. Increasing the number of internal variables will reduce this problem at the cost of increased computational intensity. Alternatively, the transition can be smoothed over the range of E_f by replacing (C.3) with:

$$n_1 < n_1^o \qquad \Rightarrow \qquad \dot{n}_1 = \alpha_f(n_1^o - n_1 - n_2) \qquad \text{(C.4)}$$

where the form of n_1^o is shown in Figure C.2. Note that as the number of internal variables are increased and ΔE_f is reduced to zero, (C.4) is reduced to (C.3). Similar modifications are made to the other equations in (5.18). This allows numeric implementation of the model.

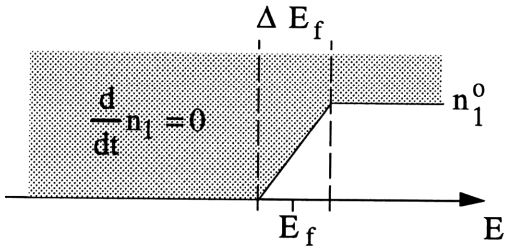

Figure C.2 - Smoothing of the transition for discretized internal variable during the AFE→FE+ transition.

The following is the listing of the Matlab script file '**model.m**'. Given a set of model parameters, and a vector containing the applied electric field, it calculates the time history of the internal variables for each family, and then outputs N_1, N_2.

```
function [N1,N2]=model(EE,dt,Parm)
% Multiple family model of material with Antiferroelectric to
% Ferroelectric switching.  This version is used in the
% parameter optimization process.
% The inputs to the model are:
%
% EE:       A vector containing the value of electric field at each
%              timestep.
% dt:       The size of each timestep.
% Parm:     Model Parameters.

% Model Parameters, to be extracted from Parm vector are
% Parm=[ Efm Efs Erm Ers Af Ar C e a];

save 'parm' Parm

Efm= Parm(1);      % The mean of the Ef pop. density
Efs= Parm(2);      % The Std. deviation of the Ef pop. density
Erm= Parm(3);      % The mean of the Er pop. density
Ers= Parm(4);      % The Std. deviation of the Er pop. density
Af = Parm(5);      % Rate parameter for forward transitions
Ar = Parm(6);      % Rate parameter for reverse transitions
C  = Parm(7);      % Stiffness parameter
e  = Parm(8);      % Ferroelectric strain coefficient
a  = Parm(9);      % Phase transition strain coefficient


% Define the coerceive field values for different families.
% Use the standard deviation of the population density to select the
% spacing of the Ef,Er for different families.
dEf=Efs/2;   dEr=Ers/2;
[Ef,Er]=meshdom([Efm-4*Efs:dEf:Efm+4*Efs],[Erm-4*Ers:dEr:Erm+4*Ers]);

% Calculate the population density for each family.

x=Ef+dEf/2; b=Efs*sqrt(2);
A=0.5+0.5*erf((x-Efm)./b);
x=Ef-dEf/2; b=Efs*sqrt(2);
```

```
B=0.5+0.5*erf((x-Efm)./b);
Nfpdf=(A-B)/dEf;


x=Er+dEr/2; b=Ers*sqrt(2);
A=0.5+0.5*erf((x-Erm)./b);
x=Er-dEr/2; b=Ers*sqrt(2);
B=0.5+0.5*erf((x-Erm)./b);
Nrpdf=(A-B)/dEr;

% Having assumed Ef and Er distributions are independent, the
% combined population density is:
Npdf=Nfpdf.*Nrpdf;

% Rearrange the families into column vectors, eliminating those
% with very small population densities (to speed up calculations).
n=(Npdf>0.002) & (Ef>=0);
Npdf=Npdf(n);
Ef  =Ef(n);
Er  =Er(n);

% Initialize internal variables for each family.
n1=zeros(size(Ef));   n2=zeros(size(Ef));

% Initialize the cumulative internal variables (summed over families)
N1=zeros(size(EE)); N2=zeros(size(EE));

% For each time step, calculate the new internal variables.
for timestep=1:length(EE)
  E=EE(timestep);

  n1old=n1;
  n2old=n2;

  idx=find(Ef-dEf/2<=E);
  n10=min(1,(E-(Ef(idx)-dEf/2))/dEf);
  n1(idx)=n1(idx)+(max(0,n10-n1old(idx)-n2old(idx))).*min(1,Af*dt);

  idx=find(E<=-Ef+dEf/2);
  n20=min(1,((-Ef(idx)+dEf/2)-E)/dEf);
  n2(idx)=n2(idx)+(max(0,n20-n1old(idx)-n2old(idx))).*min(1,Af*dt);

  idx=find((E<Er+dEr/2) & (E<Ef+dEf/2));
  n10=1-min(1,((Ef(idx)+dEf/2)-E)/dEf).*min(1,((Er(idx)+dEr/2)-E)/dEr);
  n1(idx)=n1(idx)-max(0,n1old(idx)-n10)*min(1,Ar*dt);

  idx=find((-Er-dEr/2<E) & (-Ef-dEf/2<E));
  n20=1-min(1,(E-(-Ef(idx)-dEf/2))/dEf).*...
        min(1,(E-(-Er(idx)-dEr/2))/dEr);
  n2(idx)=n2(idx)-max(0,n2old(idx)-n20)*min(1,Ar*dt);

  % Integrate the internal variables over the different families.
  N1(timestep)=sum(n1.*Npdf)*dEf*dEr;
  N2(timestep)=sum(n2.*Npdf)*dEf*dEr;
end
```

The following is the listing of the Matlab script file '**costfun.m**' which calculates the optimization cost function. Given a set of model parameters, the strain predicted by the model is calculated and compared with the experimental strain.

```
function [cost,constr]=costfun(Parm0)

% Declare some global variables
% The following contain the experimental data that we are fitting
global exptT exptdT exptE exptS Label
global GParm FitNdx ParmScl
global ParmHistory CostHistory TimeHistory
global DoPlot

% Parm  =[ Efm Efs Erm Ers Af Ar C e a];

Parm=GParm; Parm(FitNdx)=Parm0;

constr=-Parm([1 2 4 5 6]);
if max(constr)>0
  cost=1e3;
  return
end

C=Parm(7)*ParmScl(7);

for k=1:length(Label)
  dset=Label(k);

  % Expt(:,2) contains one period of the applied electric field.
  % Repeat the cycle, to account for initial transients.
  E=[exptE(:,dset);exptE(:,dset)];

  [N1t,N2t]=model(E,exptdT(dset),Parm.*ParmScl);

  % Cut out the first cycle, to get rid of initial transients.
  ndx=[length(E)/2+1:length(E)];
  N1(:,k)=N1t(ndx);
  N2(:,k)=N2t(ndx);
  EE(:,k)=E(ndx);
  Se(:,k)=exptS(:,dset);
end

Pol=N1-N2;
Nfe=N1+N2;

XX=Pol.*EE*1e6/C;
YY=Nfe/C;

for k=1:length(Label)
  XX(:,k)=XX(:,k)-mean(XX(:,k));
  YY(:,k)=YY(:,k)-mean(YY(:,k));
  Se(:,k)=Se(:,k)-mean(Se(:,k));
end
```

```
% rearrange the data from the different experiments into a single column
[m,n]=size(XX);
X=reshape(XX,m*n,1);
Y=reshape(YY,m*n,1);
S=reshape(Se,m*n,1);

% calculate scaling factors to avoid matrix ill-conditioning problem.
sX=norm(X); sY=norm(Y);

A=[X/sX Y/sY];

% Solve the problem defined by Sexpt=A*eab, using a least-square's
% approach.
eab=(A'*A)\(A'*S);
e=eab(1)/sX; a=eab(2)/sY;

Parm(8:9) =[e a]./ParmScl(8:9);
GParm(8:9)=[e a]./ParmScl(8:9);

Sm=(e*XX+a*YY);

[n,m]=size(Se);

dS=1e5*(Sm-Se)/(n*m);
cost=sum(sum(dS.^2));


if DoPlot
  clg
  plot(EE,Se,'g--'); hold on
  plot(EE,Sm);
  drawnow
end


ParmHistory=[ParmHistory; Parm];
CostHistory=[CostHistory; cost];
TimeHistory=[TimeHistory; toc ];
save 'optim.mat' ParmHistory CostHistory TimeHistory GParm ParmScl

end
```

The following is the listing of the Matlab script file '**optimize.m**'. It is used to calculate the model parameters such that the difference between the experimental strains and the model predictions are minimized.

```
% Declare some global variables
% The following contain the experimental data that we are fitting
global exptT exptdT exptE exptS Label
global GParm FitNdx ParmScl
global ParmHistory CostHistory TimeHistory
global DoPlot

format long e


% Load the experimental data which we would like to fit the model to.
% The file contains several matrices.  Each matrix contains several
% columns of data each corresponding to a run at a different
% frequency. The different matrices are:
%       exptT:              time
%       exptE:              electric field
%       exptS:              transverse strain
%       exptdT              the size of timesteps in the data
load dat3

tic        % Start the clock (To keep track of the computation time)

DoPlot=0;
diary on

disp('Start fitting Efm Efs Erm Ers.');
ParmHistory=[];  CostHistory=[];  TimeHistory=[];
GParm  =[2.6 0.4  0 0.5  1  5 1.16 0 0];
ParmScl=[1.0 1.0 1.0 1.0 1e2 1e2 1e11 1.0 1e7];
FitNdx =[ 1 2 3 4], Label=10
GParm(FitNdx)=constr('costfun',GParm(FitNdx),1)

save 'optim.mat' ParmHistory CostHistory TimeHistory GParm ParmScl

disp('Start fitting Efm Efs Erm Ers Af Ar.');
FitNdx=[1 2 3 4 5 6], Label=[1 2 3 4 5 6 7 8 9 10]
GParm(FitNdx)=constr('costfun',GParm(FitNdx),1)

%Call costfun one last time, to make sure e, a are set correctly:
costfun(GParm(FitNdx));

save 'optim.mat' ParmHistory CostHistory TimeHistory GParm ParmScl

diary off
exit
```

Appendix D - Finite Element Code (ANSYS)

The following is the listing of the ANSYS script file '**miraspct.mod**', which was used to model a segment of an adaptive mirror, and study the effect of various geometries and configurations.

```
/com, ANSYS REVISION  5.0
/com
/com, FINITE ELEMENT MIRROR MODEL
/com,
/com, This file contains a solid block model of a small mirror with
/com, an array of piezos on the back surface.  Objective is to study
/com, the tradeoffs in changing the aspect ratio of the pzts.
/com,

/com, The following parameters must be set before the execution
/com, of this file:
/com,   gt    = glass thickness / piezo thickness ratio
/com,   wt    = piezo width / piezo thickness ratio
/com,   st    = spacing / piezo thickness ratio
/com,
/com,   case  = condition along backsurface:
/com,           1: bimorph actuation model (backsurface is free)
/com,           2: hybrid model (backsurface is clamped in z dir)
/com,           3: longitudinal actuation model (backsurface is clamped)
/com,
/com,   gap   = type of separation between actuators:
/com,           1: actuators separated by space (segmented)
/com,           2: actuators separated by inactive ceramic (unsegmented)

/show,plots,plt,1
```

```
/com, Start up the preprocessor and set up the model.
/prep7
antype,static              ! Analysis type static
et,1,5,0                   ! Piezoelectric element type
et,2,5,0                   ! Glass element type

/com,
/com, Load Material Properties
/com,
*ufile,matv5,mod,/home2/kghandi/ansys/
*use,PZT-5H,1
*use,GLASS,2

/com,
/com, Begin Geometry definition
/com,

pztt=-0.25e-3              ! Piezo thickness
glst=-pztt*gt              ! Glass thickness
pthx=-pztt*wt              ! Piezo width
spcx=-pztt*st              ! Piezo spacing
ngap=nint(2*st)            ! Number of elements along each gap
npzt=nint(wt+0.5)          ! Number of elements along piezo width

del =1e-5

/com,
/com, Define Keypoints for creating a solid model.
/com

k,1,0,0,0
k,2,pthx/2,0,0
k,3,pthx/2+spcx,0,0
k,4,pthx+spcx,0,0

k,5,0,pthx/2,0
k,6,0,pthx/2+spcx,0
k,7,0,pthx+spcx,0

k,8,0,0,glst
k,9,0,0,pztt

/com, Define lines between keypoints and set number of elements to
/com, be created along each line.

l,1,2,npzt
l,2,3,ngap
l,3,4,npzt

l,1,5,npzt
l,5,6,ngap
l,6,7,npzt

l,1,8,2
l,1,9,2
```

```
/com, Drag lines into areas
adrag,1,2,3,,,,4,5,6

/com, Drag areas along z direction to form the solid glass volume
vdrag,1,2,3,4,5,6,7
vdrag,7,8,9, , , ,7
vatt,2,2,2                ! Material type 2 (Glass)

/com, Define piezos with/without gaps depending on "gap" parameter
/com, by draging appropriate areas along the thickness direction.
*if,gap,eq,2,then         ! Define unsegmented piezos
   vdrag,1,2,3,4,5,6,8
   vdrag,7,8,9, , , ,8
*else                     ! Define segmented piezos
   vdrag,1,3,7,9,,,8
*endif

vsel,all
vsel,u,volu,,1,9
vatt,1,1,1                ! Material type 1 (Piezos)

vsel,all

/com,
/com, To model a larger representative volume element, uncomment the
/com, next two commands.  This will copy the generated volumes so that
/com, the model encompasses more of the adaptive mirror.
/com,
/com, vgen,2,all,,,spcx+pthx
/com, vgen,2,all,,,0,spcx+pthx

nummrg,all,1e-7           ! Merge coincident nodes/keypoints/etc.

/com,
/com, Mesh volumes to form elements.
/com,

vmesh,all
nummrg,all,1e-7
wsort                     ! Sort node numbering for best wavefront

nsel,all
finish

/com,
/com,   MODEL COMPLETE
/com,

/com, ------------------------------------------------------------
```

```
/com,
/com,    SOLUTION PHASE
/com,

/solu
cnvtol,f,,,,1e-3          ! Force convergance tolerance
cnvtol,amps               ! Current convergance tolerance


/com,
/com,    GEOMETRIC BOUNDARY CONDITIONS
/com,
nsel,s,loc,x,-del,del
dsym,symm,1               ! Symmetry condition on x=0 surface
nsel,s,loc,y,-del,del
dsym,symm,2               ! Symmetry condition on y=0 surface

nsel,all
nsel,s,loc,z,pztt-del,pztt+del
nsel,r,loc,x,-del,del
nsel,r,loc,y,-del,del
d,all,uz                  ! Clamp (0,0,pztt) to remove rigid body mode

nsel,s,loc,z,pztt-del,pztt+del


/com, Depending on case parameter set condition along back surface

*if,case,EQ,1,then        ! case=1: bimorph actuation model
   /title, PIEZOELECTRICS ON A FLAT MIRROR, Free PZTs
*elseif,case,EQ,2,then    ! case=2: hybrid model
   d,all,uz               ! clamp backsurface in z direction only
   /title, PIEZOELECTRICS ON A FLAT MIRROR, Sliding PZTs
*else                     ! case=3: longitudinal actuation model
   d,all,uz,,,,,ux,uy     ! clamp backsurface
   /title, PIEZOELECTRICS ON A FLAT MIRROR, Clamped PZTs
*endif


/com,
/com,  VOLTAGE BOUNDARY CONDITIONS
/com,

nsel,s,loc,z,-del,del
nsel,r,loc,x,-del,pthx/2+del
nsel,r,loc,y,-del,pthx/2+del
d,all,volt,0              ! ground the glass side electrode

nsel,s,loc,z,pztt-del,pztt+del
nsel,r,loc,x,-del,pthx/2+del
nsel,r,loc,y,-del,pthx/2+del
d,all,volt,100            ! other electrode at specified voltage
nsel,all
```

```
/com, CONSTRAIN UNUSED DOFs
/com, Multifield solid elements also have magnetic and thermal
/com, degrees of freedom which aren't being used.

nsel,all
d,all,mag
d,all,temp

/com,
/com,         SOLVE THE FEM
/com,

solve
save
finish

/com, ------------------------------------------------------------------
/com,
/com,      OUTPUT RESULTS
/com,


/post1
set                          ! Load solution results

/com, Set various viewing parameters
/plopt,leg2,0
/plopt,title,0
/user
/focus,,auto
/dist,,0.0008
/win,,-1,1,0,1
/view,,-1,-1,0.4
/vup,,z
/page,,,999
/show,,,0
/type,,3

plnstr,uz                    ! Plot contour map of z displacement


/com, Find maximum surface deformation in z direction

nsel,s,loc,x,-del,pthx/2+spcx+del
nsel,r,loc,y,-del,pthx/2+spcx+del
nsel,r,loc,z,glst-del,glst+del

nsort,u,z,0,0,1
*get,zmax,sort,0,max
nusort

/com, Find surface deformation at center of piezo

nsel,r,loc,x,-del,del
nsel,r,loc,y,-del,del
*get,n,node,,num,max
*get,zcnt,node,n,u,z
nall
```

```
/com, Select nodes along the top surface for output to data file
nsel,s,loc,x,-del,pthx/2+spcx+del
nsel,r,loc,y,-del,pthx/2+spcx+del
nsel,r,loc,z,glst-del,glst+del

/com, Output current parameter settings and surface nodes to a data file

/output,data,dat
case=case
gap=gap
pztt=pztt
glst=glst
pthx=pthx
spcx=spcx
zmax=zmax
zcnt=zcnt

nlist
prnsol,u
/output

finish
/eof

/com, DISPLAY CMDS:
/show,pscr
pscr,color,0
pscr,tranx,10
pscr,trany,-150
pscr,scale,0.137
pscr,rotate,0
file,allplots,plt
plot,all

/com,change BB to 0 0 432 192
```

The following is the listing of the data file '**material.mod**', which contains the material properties used in the model.

```
PZT-5H

/com,
/com,  PIEZO PZT-5H
/com,

ep1 = 15.045e-9
ep3 = 13.009e-9

e31 = -6.62281
e33 = 23.24
e15 = 17.0345

d31 =-274e-12
d33 = 593e-12
d15 = 741e-12

c11 = 12.72e10
c12 = 8.02e10
c13 = 8.467e10
c33 = 11.74e10
c66 = 2.3e10
c55 = 2.3e10

/com, dielectric
mp,perx,ARG1,ep1
mp,pery,ARG1,ep1
mp,perz,ARG1,ep3

/com, piezoelectric
tb,piez,ARG1
tbdata,3,e31
tbdata,6,e31
tbdata,9,e33
tbdata,11,e15
tbdata,13,e15

/com, stiffness
tb,anel,ARG1
tbdata,1,c11,c12,c13
tbdata,7,c11,c13
tbdata,12,c33
tbdata,16,c55
tbdata,19,c55
tbdata,21,c66

/com, density
mp,dens,ARG1,7500


/com, The following parameters are.  not used,
```

```
/com,  but ANSYS complains if they aren't supplied:

mp,murx,ARG1,1
mp,kxx,ARG1,1

/EOF
GLASS

mp,EX,ARG1,65e9
mp,GXY,ARG1,28e9                * using G=E/(2(1+v))
mp,NUXY,ARG1,0.161
mp,dens,ARG1,2203

/com, The following parameters are.  not used,
/com,  but ANSYS complains if they aren't supplied:

mp,murx,ARG1,1
mp,kxx,ARG1,1
mp,perx,ARG1,1

/EOF
```

The following is the listing of a UNIX shell script which was used to execute the ANSYS model with various parameters, and collect the output from the various runs. Note that the first line is not a comment, and in fact specifies the type of script.

```
#!/bin/csh

# This is a shell script which starts up ANSYS, and runs the ansys
# script miraspct.mod with various parameter settings.  It also
# collects the output from the various runs for later examination.

# Clear the contents of the different output files:
echo "" >! output
echo "" >! alldata.dat
echo "" >! allplots.plt

# Delete all the temporary files created by ANSYS.
"rm" file.*

echo "TIME: SCRIPT START" >>& output
date >>& output

foreach case ( 3)                              # 1 2 3
 foreach gap ( 1 2 )                           # 1 2
  foreach gt ( 1 )                             # 0.5 1 1.5
   foreach st ( 0.5 1 2 )                      # 0.5 1 2
    foreach wt ( 0.5 1 1.5 2 2.5 3 4 5 6  ) # 0.5 1 1.5 2 2.5 3 4 5 6

     # Output some parameters to the screen.
     echo "Starting run $case $gap $gt $st $wt"

     # Create an ANSYS script containing the values of the
     # parameters and append the rest of the script to it.
     echo "case = $case" >! run.mod
     echo "gap  = $gap " >> run.mod
     echo "gt   = $gt  " >> run.mod
     echo "wt   = $wt  " >> run.mod
     echo "st   = $st  " >> run.mod
     cat miraspct.mod  >> run.mod

     # Run ANSYS with the new script file, while keeping a
     # record of the time.
     echo "" >>& output
     echo "Starting run $case $gap $gt $st $wt" >>& output
     echo "TIME: ANSYS START " >>& output
     date >>& output

     ansys < run.mod

     echo "TIME: ANSYS END " >>& output
     date >>& output

     # Append the ANSYS output to output from previous runs.
     cat plots.plt >> allplots.plt
     cat data.dat  >> alldata.dat
```

```
      cat file.err  >> output

      # Delete all the temporary files created by ANSYS.
      "rm" file.* plots.plt data.dat
     end
    end
   end
  end
end

echo "TIME: SCRIPT END " >>& output
date >>& output
```